UCLA
UCLA Electronic Theses and Dissertations

Title
Sparse Image Reconstruction and Artifact Correction of Multi-Dimensional Spectroscopic Imaging Data

Permalink
https://escholarship.org/uc/item/5ch5c8rp

Author
Burns, Brian Loren

Publication Date
2014

Peer reviewed|Thesis/dissertation

eScholarship.org Powered by the California Digital Library
University of California

University of California
Los Angeles

Sparse Image Reconstruction and Artifact Correction of Multi-Dimensional Spectroscopic Imaging Data

A dissertation submitted in partial satisfaction
of the requirements for the degree
Doctor of Philosophy in Biomedical Engineering

by

Brian Loren Burns

2014

© Copyright by
Brian Loren Burns
2014

Abstract of the Dissertation

Sparse Image Reconstruction and Artifact Correction of Multi-Dimensional Spectroscopic Imaging Data

by

Brian Loren Burns

Doctor of Philosophy in Biomedical Engineering

University of California, Los Angeles, 2014

Professor Dr. Albert Thomas, Chair

This dissertation is concerned with solving two problems in multi-dimensional magnetic resonance spectroscopic imaging (MRSI): the use of non-uniform, undersampling (NUS) together with non-linear, iterative reconstruction to accelerate the acquisition of 4D (2 spatial+2 spectral) MRSI scans *in vivo* to clinically acceptable times, and the characterization of spatio-temporal phase errors during 4D MRSI acquisition so they can be decoupled and removed from the appropriate domain in post-processing. In support of these goals, the Cambridge reconstruction algorithm was implemented from partially documented sources in order to solve the Maximum Entropy (MaxEnt) reconstruction problem for 4D MRSI. It was compared to Compressed Sensing (CS) reconstruction down to NUS rates as low as 4X *in vivo* in the human breast and was found to produce superior results. Additionally, the Group Sparse (GS) iterative reconstruction problem of 4D MRSI was defined and the solution within the Split-Bregman iterative framework was derived. It was compared to MaxEnt, CS, and Total Variation (TV) reconstructions and demonstrated the best metabolite peak reproduction, lowest mean metabolite peak RMSEs, and best denoising characteristics down to NUS rates as low as 10X in the human brain *in vivo*. Lastly, the Interleaved Navigator Scan

corrected J Resolved Echo Planar Spectroscopic Imaging (INSEP-JRESI) pulse sequence was implemented for this dissertation, which acquires a reference navigator scan at each TR in order to remove phase errors caused by B_0 field drift in 4D EP-JRESI data. A spatio-temporal framework of 4D MRSI acquisition phase errors was derived using the INSEP-JRESI sequence. With this framework in place, the various sources of phase errors that are coupled in space and time could be decoupled and removed from the data in post-processing. Gray matter phantom results using the new post-processing technique were compared to Klose's method-based post-processing and resulted in higher metabolite peak amplitudes, improved spectral line-shapes, and a more even distribution of metabolite peak energy throughout the homogeneous phantom. These projects are all original work completed in support of this dissertation by Brian Burns working under Dr Albert Thomas.

The dissertation of Brian Loren Burns is approved.

Dr. Luminita Vese

Dr. Daniel Ennis

Dr. Alex Bui

Dr. Albert Thomas, Committee Chair

University of California, Los Angeles

2014

For Lee Anna

Table of Contents

List of Figures

List of Tables

Acknowledgments

To my advisor, Dr Albert Thomas, I want to thank you for all of your encouragement and support throughout my time at UCLA. I appreciate your patience and willingness to let me try new ideas when there were no guarantees they would work. I am fortunate to have been given the opportunity to work with you as my mentor for all these years.

To my committee, thank you for taking the time to review my work and provide valuable feedback on my dissertation.

To Dr Jon Furuyama and Neil Wilson, our discussions on sparsity, spectroscopy, and the implications of under-sampling were immensely helpful to me. The feedback you gave me on my ideas pushed me to dig deeper into the literature and to develop new theory when I couldn't find the answers I needed there.

To Dr Alex Bui, thank you for accepting me into the MII lab at UCLA and providing me with four years of funding through the NLM training grant. The flexibility it provided allowed me to explore my interests in spectroscopy and sparse image reconstruction without the constant worry around funding that plagues so many graduate students.

To my parents, thank you for instilling in me the work ethic and intellectual curiosity required to pursue and finish a PhD. You have been a constant source of support and encouragement throughout my life.

To my wife, thank you for all of the sacrifices you have made over the years that allowed me to finish this dissertation. Throughout the many periods of late nights and early mornings when I was working in the lab, you never complained or tried to compete for my time, and for that I am eternally grateful. You're positive attitude and willingness to help manage other aspects of our lives while I concentrated on my dissertation allowed me to keep going when I didn't think I could.

Vita

2013	Master of Science in Biomedical Engineering, University of California, Los Angeles.
2004	Master of Philosophy in Electrical Engineering, Cambridge University.
2001	Bachelor of Science in Electrical Engineering, University of Washington.

Publications

Burns B., Wilson N.E., Thomas M.A. Split-Bregman-Based Group-Sparse Reconstruction of Multidimensional Spectroscopic Imaging Data. IEEE ISBI, 2014; Beijing, China.

Burns B., Wilson N.E., Furuyama J.K., Thomas M.A. Non-Uniformly Under-Sampled Multidimensional Spectroscopic Imaging in vivo: Maximum Entropy versus Compressed Sensing Reconstruction. NMR in Biomedicine. In Press

Furuyama J.K., Wilson N.E., Burns B., Thomas M.A. Application of compressed sensing to multidimensional spectroscopic imaging in human prostate. Magnetic Resonance in Medicine. 2012;67(6):1499-1505

Furuyama J.K., Burns B., Wilson N.E., Thomas M.A. Multi-Echo-Based Echo-Planar Spectroscopic Imaging Using a 3T MRI Scanner. Materials. 2011; 4(10):1818-1834.

Poster presentation at the International Society of Magnetic Resonance in Medicine (ISMRM) Conference 2013, Salt Lake City, UT. Maximum Entropy Reconstruc-

tion of Non-Uniformly Under-Sampled Multidimensional Spectroscopic Imaging. April 2013

Poster presentation at the Experimental NMR Conference (ENC), Asilomar, CA. Accelerated Four-Dimensional Echo-Planar J-Resolved Spectroscopic Imaging of Human Prostate: Prospective Non-Uniform Undersampling and Maximum Entropy Reconstruction. April 2013

Poster presentation at the International Society of Magnetic Resonance in Medicine (ISMRM) Conference 2012, Melbourne, Australia. Maximum Entropy Reconstruction of Correlated Spectroscopy of Human Breast in vivo. May 2012

Poster presentation at the International Society of Magnetic Resonance in Medicine (ISMRM) Conference 2012, Melbourne, Australia. Maximum Entropy Based Reconstruction of Echo-Planar Correlated Spectroscopic Imaging of Human Breast in vivo. May 2012

Poster presentation at the International Society of Biomedical Engineering (ISBI) Conference 2012, Barcelona, Spain. Maximum Entropy Reconstruction of Echo-Planar Correlated Spectroscopic Imaging of Human Breast in vivo. May 2012

Poster presentation at the National Institutes of Health (NIH). Improved Post-Processing Strategies for Multi-Dimensional Magnetic Resonance Spectroscopic Imaging. June, 2011

CHAPTER 1

Introduction

Over the past 30 years, magnetic resonance imaging (MRI) has quickly grown into one of the most valuable tools used by physicians to non-invasively diagnose disease in the human body. It is capable of imaging up to three spatial dimensions and a temporal dimension during a single scan with sub-millimeter spatial resolutions and high contrast between anatomical tissue types. By leveraging the resonant frequency of ^{1}H protons in water to produce the image, MRI is able to create static images of anatomy with and without contrast amplifying agents between tissues [25, 117], create cine images of a beating heart [53, 76, 93], measure the diffusion of water across a voxel to produce a map of the central nervous system [5, 6, 13], measure arterial blood flow velocities and pressures [44, 127], and measure activation regions in the brain based on the differences between oxygenated and deoxygenated blood [90].

While MRI is an extremely powerful tool in medicine, it is limited to imaging anatomical properties of tissue based on ^{1}H protons in water and cannot elicit their biochemical composition. ^{1}H protons exist in a variety of molecules within the human body, so physicians need not be restricted to using water-based MR images to diagnose disease. Single voxel magnetic resonance spectroscopy (MRS) and multi-voxel magnetic resonance spectroscopic imaging (MRSI) are similar to MRI, but instead of producing images from water, MRS/MRSI produce a complete resonance spectrum using the ^{1}H protons of the various metabolites and macromolecules within the human body [2, 104]. The human body contains numerous

metabolites in concentrations high enough to be seen in the spectra produced by an MRS/MRSI scan, including but not limited to: creatine (Cr), choline (Cho), glutamate (Glu), glutamine (Gln), lactate (Lac), aspartate (Asp), myo-Inositol (mI), and N-acetyl-aspartate (NAA) [56, 120]. Each of these metabolites has a distinct resonance spectrum that is produced by the ^{1}H protons within the molecule in the presence of an external magnetic field. Therefore, MRS/MRSI are able to show the biochemical composition of tissues over a region of interest (ROI) and can potentially help physicians non-invasively detect the differences between diseased and healthy tissue without the need for biopsy [7, 54, 89]. Because MRS/MRSI scans have a lower spatial resolution than anatomical MRI, they are viewed as complimentary techniques rather than a replacement.

1.1 Accelerating MRS/MRSI Acquisition

While the additional biochemical information that can be determined using MRS/MRSI is potentially very useful, there is an acquisition penalty imposed on these scans when compared to traditional MRI. Because they must repeatedly sample the MR signal from the same spatial region in order to acquire the time domain signal necessary to produce a localized spectrum, their scan times are much longer than most MRI sequences and too long to be used in a routine clinical protocol. As an example, the 2D single voxel Localized-Correlated Spectroscopy (L-COSY) MRS and 4D multi-voxel Echo Planar based Correlated Spectroscopic Imaging (EP-COSI) MRSI sequences, which both produce 2D spectra, require 20 and 40 minutes, respectively, using standard sequence parameters [78, 120]. When incorporated into a long imaging study that contains numerous MRI acquisitions, an additional 20 to 40 minutes of scan time may not be possible for some of the sickest or most uncooperative patients.

Reducing the scan times of the MRS/MRSI sequences is critical to their suc-

cess in being accepted into standard clinical protocols. Because all MRS/MRSI sequences are acquired as rasterized scans, their scan times are directly proportional to their spatial-spectral resolutions and bandwidths. If sampling patterns along the rasterized dimensions are uniform, the scan time can be reduced by truncating the number of rasterized lines, which would reduce the spatial-spectral resolutions. Additionally, the spacing between rasterized lines can be increased, which would decrease the bandwidth and increase the possibility of aliasing. Therefore, these methods may not be able to sufficiently reduce the scan times to clinically acceptable levels while maintaining sufficient spatial-spectral resolutions and bandwidths.

The acquisition of both 2D MRS and 4D MRSI data *in vivo* can be accelerated by non-uniformly under-sampling (NUS) the rasterized dimensions, so the scans require as little as $1/8^{th}$ of the time of a fully sampled scan while maintaining the spatial-spectral resolutions and bandwidths. The sampling pattern is no longer uniform, but a random distribution of samples that ensures no coherent aliasing is present [65]. However, the NUS pattern produces incoherent artifacts in the data that must be removed by non-linear reconstruction. These techniques reconstruct the points that were not sampled during acquisition and recreate the fully sampled data set from the under-sampled data, which was acquired in much less time. However, if these artifacts are not removed by the reconstruction without negatively affecting the under-lying biochemical information in the MRS/MRSI scan, its value may be decreased. Therefore, the ability to decrease MRS/MRSI scan times to clinically acceptable levels using NUS hinges on the success of non-linear reconstruction techniques to adequately reconstruct the missing data without adding or removing spatial-spectral features of the scan.

1.2 Iterative Non-Linear Reconstruction in MRS/MRSI

The Cambridge algorithm was one of the first general purpose non-linear reconstruction techniques developed for NUS imaging data and has been adapted for NMR and MRS/MRSI data sets [19, 59]. It reconstructs the missing MRS/MRSI sample points by solving for them as the solution to the Maximum Entropy (MaxEnt) reconstruction problem, which is formulated as a constrained convex optimization problem and solved by a variant of the conjugate gradient method [114]:

$$\begin{aligned} &\max_m && S(m)_{1/2} \\ &\text{such that} && \|K\mathcal{F}m - d\|_2 \leq \sigma \end{aligned} \tag{1.1}$$

where m is the estimated fully-sampled spectrum, $\mathcal{F}$ is the Fourier transform, K is the NUS matrix that describes which samples were acquired, d is the time-domain measured data, σ is the noise standard deviation, and $S(m)_{1/2}$ is the entropy of the estimated spectrum. The spectrum with the highest entropy is that which conforms to the uniform distribution and has a flat baseline. Therefore, by iteratively maximizing the entropy of the spectrum constrained by the sampled data, MaxEnt smooths out the spectrum and removes artifacts caused by NUS [61, 114].

Compressed Sensing (CS) reconstruction is a non-linear reconstruction method that was developed after MaxEnt and solves a similar constrained convex optimization problem, but maximizes the sparsity of the data instead of maximizing the entropy [36]:

$$\begin{aligned} &\min_m && \|\psi m\|_1 \\ &\text{such that} && \|K\mathcal{F}m - d\|_2 \leq \sigma \end{aligned} \tag{1.2}$$

where $\|\psi m\|_1$ is the ℓ_1-norm of the spectrum in some known transform domain, ψ, and the remaining terms are identical to the MaxEnt problem. Sparsity in ψ implies the spectrum is compressible in that domain and can therefore be repre-

sented by fewer samples than what is required by the Nyquist limit. Sparsity is a measure of how few transform domain coefficients are needed to fully represent the data; the sparsest solution to the problem is that which has the smallest ℓ_1-norm of those coefficients. NUS artifacts resemble broadband noise, so they decrease sparsity by not being compressible in the transform domain. By constraining the problem with the sampled data and iteratively reducing the ℓ_1-norm, NUS artifacts can be removed and the missing samples reconstructed [20, 21, 23, 36].

In addition to MaxEnt and CS reconstruction, the Group Sparse (GS) reconstruction method is one of the more recently developed techniques that can be used to restore the missing samples from under-sampled MRS/MRSI data [129]. It maximizes the structural sparsity of the data, which is the tendency of transform coefficients to form clumps as opposed to being spread across the domain, by formulating the problem as a constrained convex optimization problem [42, 64]:

$$\begin{aligned} \min_{m,z} \quad & \|z\|_{1,2} \\ \text{such that} \quad & \|K\mathcal{F}m - d\|_2 \leq \sigma \\ & z = Gm \end{aligned} \tag{1.3}$$

where $\|z\|_{1,2}$ is the mixed-$\ell_{1,2}$-norm that calculates the ℓ_1-norm over a set of ℓ_2-norms of groups of spectral points, and G maps the reconstructed spectrum in m to the groups in z [125]. The ℓ_2-norm is calculated over groups of spectral points that are spatially or spectrally correlated. This differs from MaxEnt and CS that calculate the entropy and ℓ_1-norm over individual points and do not exploit the correlations between adjacent samples. Because of the nature of spectral peaks, MRS/MRSI data sets are highly correlated across the spectral domain and exhibit a high of degree of structural sparsity. By grouping spectral points together, group sparsity increases the structural sparsity of groups of spectral points so that each sample in the group is reconstructed with its adjacent neighbors.

1.3 Phase Errors in MRS and MRSI Acquisition

Whether MRS/MRSI scan times are long or short, the acquisitions still occur in the presence of numerous sources of phase error that can shift the spatial-spectral domain, broaden peaks, and blur the true locations of metabolite peaks if not properly removed. Line-widths must be narrowed so metabolite peaks can be resolved from each other in the spectrum and metabolite peak energy should be localized to the voxel from which it originated, and not shifted into neighboring voxels. If the spatio-temporal Point Spread Function (PSF) of the acquired data is not narrowed in post-processing by characterizing and removing these phase errors in the appropriate domain, the utility of MRS/MRSI is lessened because of the increased uncertainty of the source of metabolite resonances.

MRS/MRSI acquisition phase errors may depend on time, on space, or on both space and time, and can occur in k-space, the spatial domain, the temporal domain, the spectral domain, or a combination thereof [70,73,118]. Because of the interdependence of the various domains as a result of their Fourier relationships, these phase errors are coupled to each other even though they originate from different sources. This makes it difficult to characterize each phase error and remove it in the appropriate domain without the influence of the others. Previous work in MRS/MRSI has typically addressed a single source of error without addressing the others, so their coupled nature has not been addressed and they have not been adequately characterized [39,73,118]. As multi-voxel MRSI has become more popular over the past 20 years, the phase error correction techniques being used are from single-voxel MRS, which only characterizes the temporal phase evolution.

Luckily, there is a substantial body of work from MRI that characterizes the spatial domain phase evolution during an acquisition, and shows how it can be decoupled from the spatio-temporal phase errors in scans with a temporal dimension [38, 45, 70, 71, 94, 96]. Many of these techniques can be modified and applied

to MRSI in order to decouple, characterize, and remove phase errors from an acquisition, such as: the Dynamic Off-Resonance in k-space (DORK) technique from fMRI can be used to estimate time dependent phase shifts using a reference TR that removes any other sources of phase error from the estimate [94], the Interleaved Dual-Echo Acceleration Echo Planar Imaging (IDEA-EPI) readout can be used to remove spatio-temporal phase errors in k-space where they occur rather than in the spatial domain, where they are currently addressed in MRSI [96], and extensive phase error modeling that has been done within MRI can be used in MRSI to support any assumptions that need to be made regarding the phase evolution [70, 71]. By adjusting each of these techniques to the acquisition trajectory of an MRSI pulse sequence through the spatial-spectral domains, the interdependence of phase errors in MRSI can be reduced and they can be successfully removed from the acquisition in post-processing.

1.4 Dissertation Goals and Organization

The two main goals of this dissertation are to accelerate the acquisition of multi-dimensional spectroscopy and spectroscopic imaging through NUS and iterative reconstruction, and to characterize the phase errors of an MRS/MRSI acquisition so they can be removed in the appropriate domain.

The first goal is composed of three parts:

1. Design and implement the 2D Poisson-gap sampling mask creation process to stochastically under-sample MRS/MRSI data.

2. Implement the Cambridge algorithm and compare MaxEnt iterative reconstruction results of MRSI data to those from CS.

3. Derive a solution to the GS reconstruction problem within the Split-Bregman iterative framework and compare the MRSI reconstruction results to Max-

Ent and ℓ_1-norm-based reconstruction results.

The second goal is composed of two parts:

1. Design and implement the Interleaved Navigator Scan corrected J Resolved Echo Planar Spectroscopic Imaging (INSEP-JRESI) pulse sequence that acquires an interleaved water navigator scan within each TR.

2. Design and implement a post-processing pipeline that decouples the acquisition phase errors from each other and corrects them in the appropriate domain using the INSEP-JRESI sequence.

This dissertation is separated into eight chapters, including the introduction. It is composed of three research manuscripts and supporting materials for those manuscripts that provide background and more detail. Chapter 2 covers relevant MRS physics and describes pulse sequences referred to in later chapters. Chapter 3 covers uniform and non-uniform sampling theory, the nature of under-sampling artifacts in MRSI, and the 2D Poisson-gap sample mask creation algorithm in detail. Chapter 4 discusses sparsity and its relationship to CS reconstruction, the nature of entropy and the MaxEnt problem, and a detailed description of the Cambridge algorithm with pseudo-code. GS reconstruction is not covered in chapter 4 because it is discussed in detail in chapter 6. The first manuscript is in chapter 5 and discusses MaxEnt reconstruction of 4D MRSI data compared CS in the human breast *in vivo*. Results are provided for prospective and retrospective *in vivo* data as well as quantitative metrics between the two reconstruction methods over a simulated data set. The second manuscript is in chapter 6 and derives a solution to the GS reconstruction problem within the Split-Bregman iterative framework. Results form gray matter phantom and *in vivo* brain data are provided with comparisons between GS using two different grouping patterns and multiple iterative reconstruction methods. The third and final manuscript is presented in

chapter 7. It provides descriptions of the INSEP-JRESI pulse sequence, detailed discussions on the nature of phase errors in MRSI, a post-processing pipeline to correctly remove the phase errors, and results of gray matter brain phantom scans processed using the new method compared to the current state of the art. The conclusions are in the final chapter.

CHAPTER 2

2D MRS and 4D MRSI Basics

2.1 NMR Theory Overview

The behavior of ^{1}H protons interacting with an external magnetic field is the basis for MRI and MRS. Other species of nuclei with odd mass numbers can also be used, such as ^{13}C, ^{31}P, and ^{19}F, but the vast majority of MRS applications *in vivo* use ^{1}H because of its vast abundance in the human body and its compatibility with existing MRI hardware.

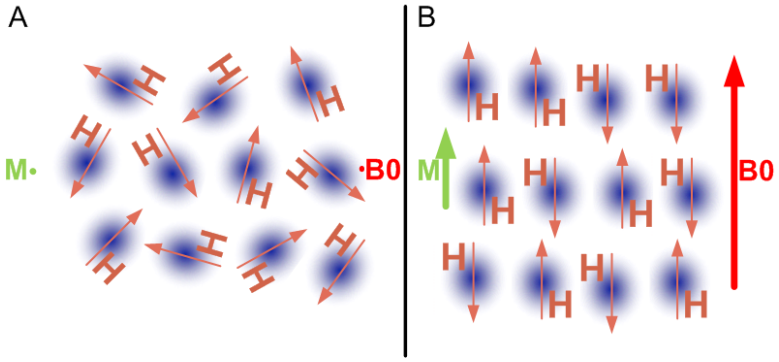

Figure 2.1: Illustration of ^{1}H protons interacting with a magnetic field, B_0. (A) Isotropic proton polarization when B_0=0 (B) Protons align parallel and anti-parallel to B_0 when B_0!=0

As shown in figure 2.1A, when an ensemble of ^{1}H protons are not in the presence of an external magnetic field (B_0), their individual magnetic moments are randomly oriented in space and the net magnetization (M) of the ensemble is zero. However, when placed in a magnetic field, as shown in figure 2.1B, ^{1}H protons settle into a state of thermal equilibrium and align themselves parallel and

anti-parallel with the direction of the magnetic field according to the Boltzmann distribution. There is now a net magnetization in the ensemble from their individual magnetic moments because slightly more ^{1}H protons align themselves parallel to the field than anti-parallel. Because ^{1}H is a spin-$\frac{1}{2}$ nucleus, it has two spin quantum states that make it align parallel (spin-up) or anti-parallel (spin-down) when in B_0. These quantum states are separated by an energy difference, ΔE, proportional to B_0 such that spin-down protons are in a higher energy state than spin-up protons. Spin-up protons can be excited to the higher energy state by a radio frequency (RF) pulse of energy equal to ΔE so that many of the spin-up protons are now spin-down and the system is no longer at thermal equilibrium [1,32].

When in the presence of a magnetic field B_0, protons will not only align their magnetic moments parallel and anti-parallel with the field, but they will begin to precess at a frequency proportional to B_0. This precessional frequency is:

$$\nu_0 = \frac{\gamma}{2\pi} B_0 \tag{2.1}$$

where γ is the gyromagnetic ratio of ^{1}H and equals $26.752 \times 10^7\ rad\, T^{-1} s^{-1}$. This frequency is called the Larmor frequency and is equal to $63.87 Mhz$ and $127.73 Mhz$ when $B_0 = 1.5T$ and $3T$, respectively. When spin-up protons are excited to the higher spin-down energy state by an RF pulse, the frequency of the RF pulse is the Larmor frequency, such that $\Delta E = h\nu_0$, where h is Planck's constant [32].

Figure 2.2A shows a molecule with numerous ^{1}H protons bonded to carbon, oxygen, and other ^{1}H protons surrounded by their electron shields in blue. Because electrons are a moving charged particle with mass, they have a magnetic moment associated with them that acts on the ^{1}H nucleus. The proximity of the ^{1}H protons to the electron clouds of the other nuclei shield them from B_0 so their Larmor frequency is shifted away from that of free ^{1}H protons. Therefore, a more

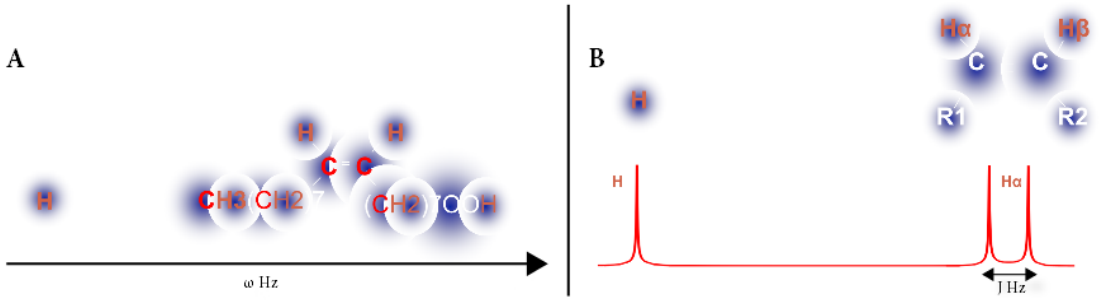

Figure 2.2: Illustration of chemical shift and J-coupling effects on ^{1}H protons. (A) Electron cloud shielding of ^{1}H protons by neighboring nuclei. (B) Nuclei-nuclei interactions of neighboring ^{1}H protons through chemical bonds adjacent nuclei.

accurate representation of the Larmor frequency should be:

$$\nu_0 = \frac{\gamma}{2\pi} B_0(1 - \sigma) \tag{2.2}$$

where σ is a dimensionless shielding constant that depends on the chemical environment of the nucleus and is measured in units of parts-per-million (ppm). This bonding-structure dependent frequency shift is known as chemical shift and is one of the processes that gives metabolites their unique spectral signatures measured by MRS [32].

Another feature of the proton resonance spectrum is the splitting of a single ^{1}H resonance into several smaller peaks as shown by figure 2.2B. This splitting is caused by the interaction of ^{1}H nuclei with the magnetic moments of other nuclei through chemical bonds and is referred to as J-coupling [32]. As the chemical shift is caused by the electron cloud of nearby nuclei and shifts the resonance frequency of ^{1}H protons away from the Larmor frequency, J-coupling is a nuclei-nuclei interaction that splits the energy levels of a proton so there are more than two per spin system (spin-up and spin-down) [1]. This splitting of the energy levels manifests itself as separate resonances in the spectrum because J-coupling is a frequency modulated process known as J-modulation and is measured in the 10s of Hz. The split resonance peaks are centered at the chemically shifted

resonance frequency of each ^{1}H proton, but are separated by the J-coupling value between each ^{1}H proton and its adjacent, bonded nuclei. Some ^{1}H protons are J-coupled to many other nuclei through numerous bonds, so the splitting patterns can be extremely complex given that splitting occurs for each bond.

J-coupling between nuclei affects the splitting of protons in a 1D spectrum, but also governs the frequency modulation of the coherence transfer between nuclei in an excited energy state [32]. Coherence transfer is beyond the scope of this dissertation, but it is important to know the process exists because it is what is used to form the second dimension of some types of 2D MRS spectra with chemical shift forming the first [2].

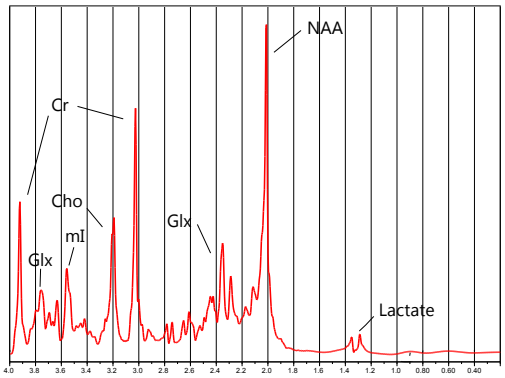

Figure 2.3: A 1D MRS spectrum showing numerous metabolites

When an ensemble of protons is disturbed from thermal equilibrium by an RF pulse centered at the Larmor frequency, but having a bandwidth sufficient to excite chemically shielded ^{1}H protons, the excited protons immediately begin to release the ΔE energy and return to their spin-up state at equilibrium. This release of energy from the chemically shifted protons is the Nuclear Magnetic Resonance (NMR) signal picked up by the scanner and used to form a 1D spectrum as shown in figure 2.3. The resonance peaks of various *in vivo* metabolites are shown in the figure, including Choline (Cho), Creatine (Cr), Glutamate and Glutamine (Glx), Lactate (Lac), Myo-Inositol (mI), and N-acetylaspartate (NAA). Water (Wat) is not shown but it resonates at 4.7ppm just off the left edge of the spectrum.

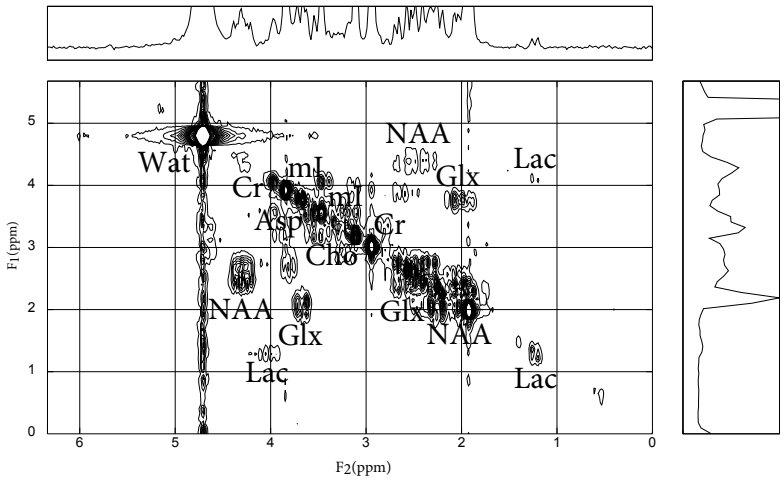

Figure 2.4: A 2D L-COSY spectrum showing numerous metabolites and the effects of chemical shift, J-coupling, and coherence transfer.

Figure 2.4 shows a 2D MRS spectrum with many of the same metabolites shown in figure 2.3. The horizontal dimension, F_2, shows the chemical shift effect on ^{1}H protons and the vertical dimension, F_1, represents the indirectly sampled coherence transfer between nuclei. As can be seen in the 1D projection of the 2D spectrum at the top of figure 2.4, the information represented by the diagonal peaks is roughly equivalent to the information present in the 1D spectrum from figure 2.3. However, the off-diagonal peaks, known as cross-peaks, are a result of sampling the coherence transfer between J-coupled nuclei and are not present in the 1D spectrum. The main benefit of producing a spectrum in this manner is that metabolite resonances that overlap because of similar chemical shifts or complex J-coupled splitting, have distinct cross-peaks that can be used to disambiguate them [120].

2.2 2D MRS and 4D MRSI Pulse Sequences

Figure 2.5 shows the 2D Localized Correlation Spectroscopy (L-COSY) pulse sequence that is used to acquire single-voxel 2D spectra with the J-modulated coherence transfer among nuclei being sampled as an increasing phase delay between

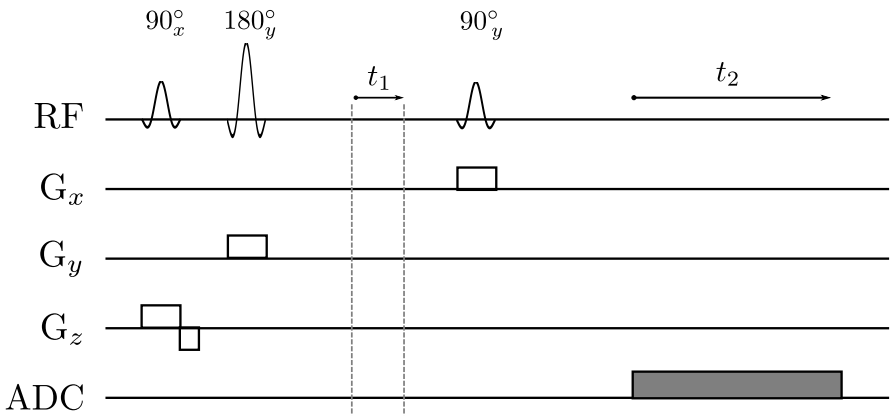

Figure 2.5: Illustration of the L-COSY pulse sequence used to acquire single-voxel 2D MRS spectra *in vivo*.

TRs [120]. It consists of three slice selective RF pulses (90°_x-180°_y-90°_y) that are used to localize and excite a cube in 3D space, the t_2 readout period used by the ADC to directly sample the decaying signal from the excited cube, and the incremented phase delay, t_1, between the second and third pulses that indirectly samples the coherence transfer between nuclei. The figure shows a single repetition time (TR) of the pulse sequence that is typically repeated 50-100 times depending on the anatomy being scanned. During each TR, the sequence acquires a 1D spectrum along the t_2 dimension from the same excited cube in 3D space, which shows the chemical shift and J-coupled splitting of each of the metabolites present. The coherence transfer evolves between the second and third RF pulses, so when the t_1 delay is incrementally increased from one TR to the next, the coherence transfer phase modulation is indirectly sampled over the 50-100 TRs.

The 2D J Point-Resolved Spectroscopy (JPRESS) pulse sequence can also be used to acquire single-voxel 2D spectra, but does not sample the coherence transfer between coupled spin systems as in L-COSY [108]. JPRESS samples only the J-modulation of coupled spin systems, so the spectral dispersion across the second dimension is lower than in L-COSY because the coherence transfer between nuclei occurs across a wider bandwidth than J-modulation alone. The JPRESS pulse sequence is identical to L-COSY with the exception of the flip angle used for

the third slice selective RF pulse; L-COSY uses (90°_x-180°_y-90°_y) and JPRESS uses (90°_x-180°_y-180°_y). Because JPRESS uses a 180° RF pulse instead of a 90° RF pulse to refocus the Hahn spin echo from the 90°-180° RF pulses, the coherence transfer between nuclei is not sampled; however, because of the increased refocussing efficiency of the 180° RF pulse over a 90° RF pulse, JPRESS has a theoretical sensitivity two times greater than L-COSY. A full JPRESS acquisition can be completed using 50-64 t_1 increments compared to 50-100 increments for L-COSY because of the reduced bandwidth requirements of sampling the J-modulation instead of the coherence transfer.

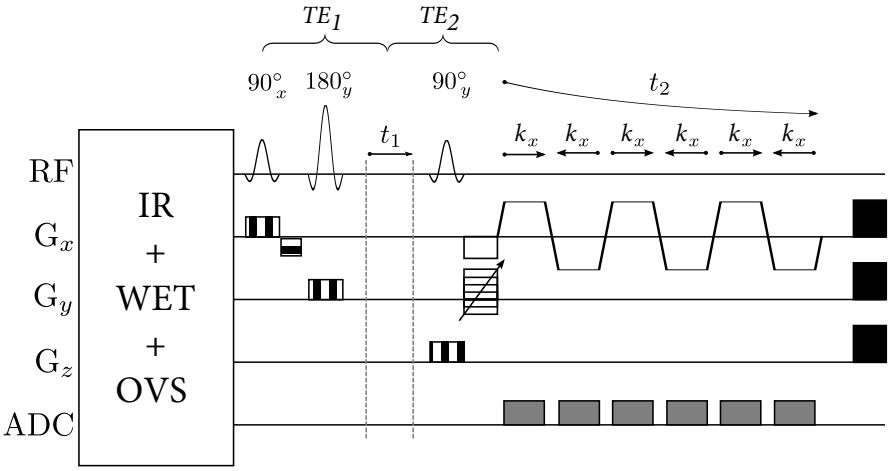

Figure 2.6: Illustration of the EP-COSI pulse sequence used to acquire multi-voxel 4D MRSI spectra *in vivo*.

The L-COSY and JPRESS sequences have been extended to acquire data along two spatial dimensions, (k_x, k_y), as well as the two spectral dimension, (t_1,t_2), during each TR [78, 88]. Figure 2.6 shows a single TR of the Echo Planar Correlated Spectroscopic Imaging (EP-COSI) sequence that is repeated 50-100 times depending upon anatomy, as is done for L-COSY. The 4D Echo Planar J-Resolved Spectroscopic Imaging (EP-JRESI) sequence is the 4D extension of JPRESS, so it is identical to EP-COSI with the exception of using a 180° flip angle for the third RF pulse. As can be seen, the three slice selective RF pulses are still present, as is the t_1 increment between the second and third pulses used to

indirectly sample the coherence transfer or J-modulation; however, an echo planar imaging (EPI) readout train of bipolar gradients has been added along k_x and t_2 as well as a phase encoding gradient along k_y. These are methods borrowed from MRI that allow for fast acquisitions of the spatial dimensions (k_x, k_y) during a single TR [82, 83].

The phase encoding gradient samples the k_y spatial dimension in k-space by incrementally adding a phase shift to the 1D spectra acquired at each TR that can then be mapped to a point in space. The EPI readout interleaves the acquisition of the k_x and t_2 dimensions by repeatedly sampling the same line in k-space multiple times during the same TR. The plateau of each bipolar gradient represents one full traversal across k_x, so the n^{th} point in each plateau represents the n^{th} point in k-space. By making a vector from all of the n^{th} points in each of the plateaus, the full 1D spectra along t_2 for the n^{th} point in space can be created. Therefore, at each TR, the t_1 and k_y dimensions are incrementally sampled while the t_2 and k_x dimensions are readout completely; each TR acquires a single $k_x - t_2$ plane in the 4D, (k_y, k_x, t_2, t_1), space which corresponds to a single point in the $k_y - t_1$ plane. [86, 98].

CHAPTER 3

Non-Uniform Under-Sampling

3.1 Motivation

A typical 2D L-COSY or JPRESS scan with a TR=1.5s, 100 t_1 increments, and 8 averages (for improved SNR) takes 20 minutes to complete. A 4D EP-COSI or EP-JRESI scan that uses a TR=1.5s, 100 t_1 increments, and 16 k_y increments over a 16x16 cm^2 Field of View (FOV) takes 40 minutes to complete. These 2D and 4D scan times are too long to be used in a clinical protocol and must be reduced in order for MRS and MRSI to be used on a routine basis. Because the scan times for each sequence are directly proportional to the number of t_1 or k_y increments used, they can be accelerated by reducing the number of increments during each scan and increasing the step-size of each increment so the same bandwidth is covered in fewer steps. However, this will reduce the spatial-spectral bandwidths and resolution, which may compromise their usefulness or lead to spatial-spectral aliasing.

By skipping t_1 increments and sampling the t_1 dimension non-uniformly, the 2D L-COSY and JPRESS sequences can be accelerated by sampling most of the 1D spectra along F_2, but not all [3, 106]. Under-sampling artifacts caused by non-uniform under-sampling (NUS) can be minimized by ensuring the sampling pattern is random in nature and causes incoherent artifacts instead of the coherent, aliased artifacts from uniform under-sampling [35]. Like 2D under-sampling, the t_1 dimension of an EP-COSI or EP-JRESI scan can be non-uniformly under-

sampled in order to accelerate acquisition, but the k_y dimension is also incrementally sampled and further acceleration can be realized by under-sampling this second dimension. A greater speed-up can be realized in 4D MRSI than 2D MRS because there are two dimensions that can be under-sampled simultaneously. Each point along t_1 or within the $k_y - t_1$ plane that is not acquired represents a missing line in 2D MRS or a missing plane in 4D MRSI, respectively.

As will be discussed in later chapters in this dissertation, the incoherent artifacts caused by NUS can be removed, and the missing sample points restored by iterative, non-linear reconstruction techniques, such as MaxEnt, CS, or GS, while preserving the spatial and spectral resolutions and bandwidths [81, 85]. However, the nature of NUS artifacts in 4D MRSI and a discussion of uniform vs. non-uniform sampling theory must first be presented.

3.2 Sampling Theory Overview

Sampling continuous functions is typically carried out in a regular pattern of evenly spaced points over n-dimensions. The spacing between points along a dimension of the signal dictates the highest frequency that can be reproduced from the sampled points in that dimension. For a sample spacing equal to Δt, this frequency is equal to:

$$N_f = \frac{1}{2\Delta t} \tag{3.1}$$

where N_f is called the Nyquist frequency and Δt is the Nyquist sample rate [58]. The 1D relationship between a sampled dimension of the function and its representation in Fourier space is the following [35]:

$$h(t) = f(t)\sum_{k=-\infty}^{+\infty}\delta(t-k) \xrightarrow{\mathcal{F}} H(w) = F(w) * \sum_{k=-\infty}^{+\infty}\delta(w-k) \tag{3.2}$$

where $f(t)$ is the continuous signal being sampled, $h(t)$ is the discrete, sampled signal, $\mathcal{F}$ indicates the Fourier transform, $F(w)$ is the Fourier representation of $f(t)$, and $H(w)$ is the Fourier representation of $h(t)$.

From equation 3.2 and as illustrated in the top row of figures 3.1a-c, it can be seen the sampled signal, $h(t)$, is the result of multiplying a continuous function, $f(t)$ by a comb function in the time domain and as a result, the function, $H(w)$, is the convolution of $F(w)$ with a comb function in the frequency domain. The Fourier transform of a time domain comb function with spacing equal to Δt is a comb function with spacing $\frac{1}{\Delta t}$. Therefore, convolving $F(w)$ with the comb function in the frequency domain results in the periodic replication of $F(w)$ every $\frac{1}{\Delta t}$. If Δt is less than the Nyquist sample rate, replicas of $F(w)$ will overlap and alias, so there is a mixing of the high and low frequency components of each replica with its adjacent neighbors, as shown in the middle row of figure 3.1c [66].

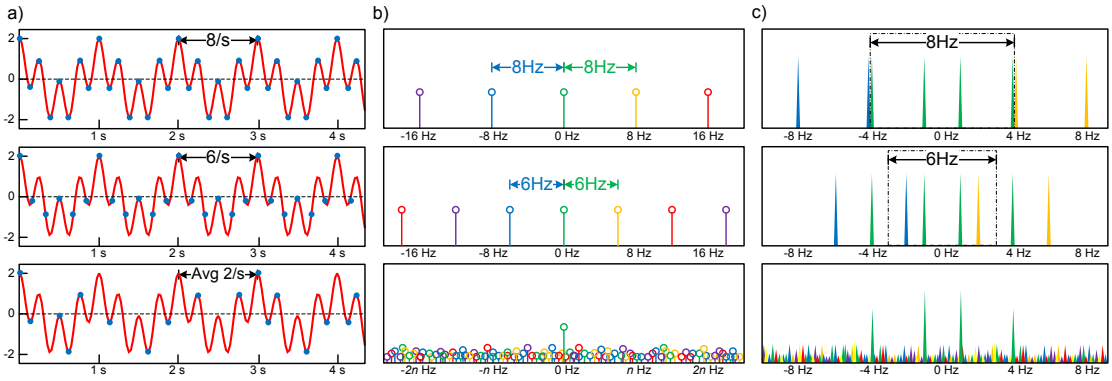

Figure 3.1: Relationship between the function, $f(t) = cos(2\pi 4t) + cos(2\pi t)$, the sample function, $s(t)$, and the DFT of the sampled points, $H(w) = \mathcal{F}(f(t) \cdot s(t))$ **a)** sampling $f(t)$ (top) at the Nyquist rate, $\Delta t = 8/s$ (middle) below the Nyquist rate, $\Delta t = 6/s$ (bottom) an average rate of $\Delta t = 2/s$ NUS **b)** DFT of $s(t)$ showing $\frac{1}{\Delta t}$ is (top) $8Hz$ (middle) $6Hz$ (bottom) undefined for NUS **c)** $H(w)$ showing (top) no aliasing occurs when Δt is equal to or greater then the Nyquist rate (middle) aliasing occurs when Δt is less than the Nyquist rate (bottom) aliasing does not occur under certain circumstances when Δt is random and less than the Nyquist rate on average.

In order to avoid aliasing caused by sampling below the Nyquist rate, non-uniform under-sampling (NUS) can be used that have an average sample rate

much lower than the Nyquist rate [11,12,110]. If the distribution of sample points is derived directly from a random distribution (i.e., Poisson sampling), or if the sample points are from a regular sampling pattern that have been shifted in time according to the uniform or Gaussian distributions (i.e., Jittered sampling), the DFT of the sample function (i.e., Point Spread Function (PSF)) no longer resembles a comb in the Fourier domain, but a single δ function at the center frequency surrounded by incoherent broadband noise as illustrated in figure 3.1b [35]. Sampling in this manner does not result in the periodic replication of $F(w)$ as with regular sampling patterns because the combination of NUS with the time domain sample window act as a low-pass filter that attenuates high frequency components of the signal that would normally alias [30]. The exact nature of this attenuation is dependent upon the sample points' distribution, the Nyquist sampling rate, and the length of the sample window. As a result, the components of $F(w)$ that would normally alias with a uniform sampling pattern resemble incoherent broadband noise whose energy is equal to that of the attenuated components, as illustrated in the bottom row of figure 3.1c.

3.3 Under-Sampling in 4D MRSI

Each sampled point within a 4D MRSI volume exists at the intersection of six planes across three domains: the t_1-t_2 plane in the time domain, the k_x-k_y plane in the spatial domain, and the mixed-domain planes, k_x-t_1, k_x-t_2, k_y-t_1, and k_y-t_2. For the purposes of 4D MRSI NUS and iterative reconstruction, however, only the two mixed-domain planes, k_x-t_2 and k_y-t_1, need to be considered [50]. This is because of the nature of MRSI data acquisition; the k_x and t_2 dimensions are readout simultaneously, which results in a complete k_x-t_2 plane acquired during each TR and the k_y and t_1 dimensions are incrementally phase encoded dimensions so that the k_y-t_1 plane is acquired point-by-point over the duration

of the scan. Because the k_x an t_2 dimensions are uniformly, fully sampled at each TR as the $k_x - t_2$ plane, and the k_y and t_1 dimensions are incrementally sampled, it is far simpler to under-sample the indirect dimensions than the direct dimensions during acquisition. Therefore, for this dissertation the $k_y - t_1$ mixed, domain plane is under-sampled while the $k_x - t_2$ plane is always uniformly, fully sampled. Under-sampling the $k_x - t_2$ readout plane is possible, as was shown previously in under-sampled hyper-polarized ^{1}3C MRSI, which used a series of random phase encoding blips along the readout to under-sample $k_x - t_2$ [62]. However, it is more common to under-sample the indirect dimensions that are incrementally acquired over the course of the scan [51, 81, 102].

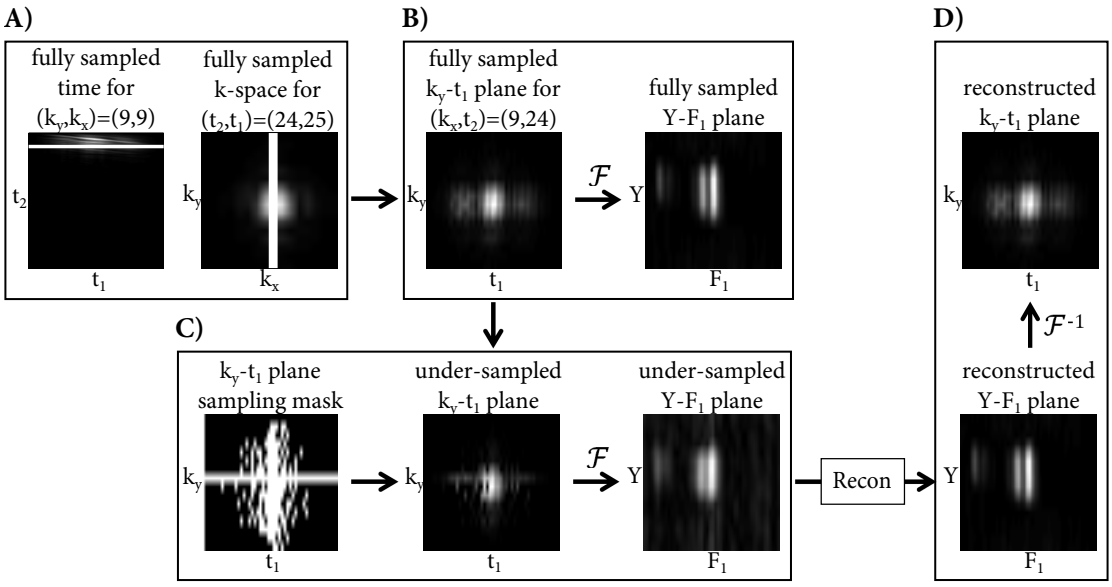

Figure 3.2: Conceptual illustration of 4D NUS MRSI and iterative reconstruction to recover the $k_y - t_1$ plane. **A)** $t_2 - t_1$ and $k_y - k_x$ planes that result from taking a specific point in the $k_y - k_x$ and $t_2 - t_1$ planes, respectively. **B)** fully sampled $k_y - t_1$ plane and its Fourier transform that results from the intersection of the white lines in A). **C)** Applying the sampling mask to the fully sampled $k_y - t_1$ plane results in sampling artifacts in the $Y - F_1$ plane. **D)** Iterative reconstruction applied to the $Y - F_1$ plane removes the NUS sampling artifacts and restores the missing points in $k_y - t_1$.

Figure 3.2 illustrates the $k_x - t_2$ and $k_y - t_1$ mixed domain planes and shows the effects of under-sampling the $k_y - t_1$ plane on the $Y - F_1$ plane. As can be seen in figure 3.2A, the temporal and spatial planes, $t_2, -t_1$ and $k_y - k_x$, are

at the intersection of the 4D MRSI volume and a single point in space or time, respectively. Therefore, the mixed-domain $k_y - t_1$ plane is at the intersection of the 4D MRSI volume and a point in $k_x - t_2$. Because a point in space can be formed by two lines, the white lines in figure 3.2A illustrate the point in $k_x - t_2$ used to form the $k_y - t_1$ plane.

The $Y - F_1$ plane in figure 3.2B shows the F_1 frequency modulation of signals along Y. Because $k_y - t_1$ is fully sampled, there are no artifacts in $Y - F_1$ from the sampling pattern used. However, once the sampling mask is a applied in 3.2C, there are missing samples in the $k_y - t_1$ plane and artifacts are present in $Y - F_1$. Iterative non-linear reconstruction is applied to the $Y - F_1$ plane to remove the sampling artifacts and reconstruct the missing samples in the $k_y - t_1$ plane, as shown in figure 3.2D.

Throughout this dissertation, the sample domain is the under-sampled $k_y - t_1$ plane and the reconstruction domain is the $Y - F_1$ plane where NUS artifacts are present. The $k_x - t_2$ and $X - F_2$ planes are fully sampled and therefore do not require missing samples to be reconstructed or artifacts removed.

3.4 Under-Sampling Artifacts in 4D MRSI

Many of the differences between uniform sampling and NUS of 4D MRSI data are shown in figure 3.3 using data from an EP-COSI acquisition of healthy human breast tissue. The samping mask used to under-sample the $k_y - t_1$ plane is shown on the left, the uniformly sampled data is in the middle, and the 4X NUS data is on the right. A 2D COSY spectrum from each data set is shown in the top of the figure and the spatial distributions of the olefinic unsaturated fatty acid cross peaks from each data set are shown in the bottom.

As can be seen, the uniformly, fully sampled data set shows no periodic replication of any spatial-spectral features within the COSY spectrum or the olefinic

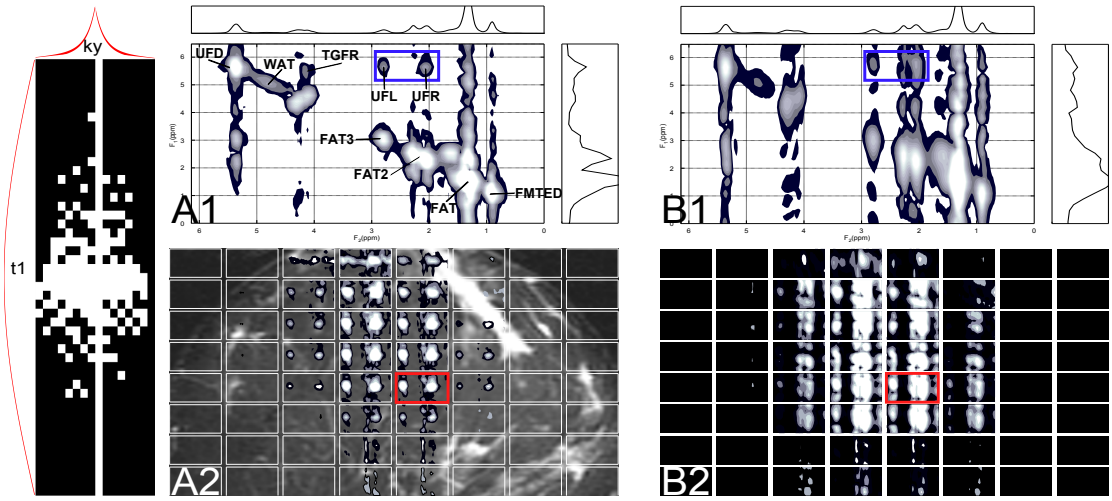

Figure 3.3: (Left) NUS mask used to under-sample the $k_y - t_1$ plane (Top) 2D COSY spectra from a 4D EP-COSI scan of healthy, fatty breast tissue for A1) uniformly sampled B1) 4X NUS (Bottom) Spatial distribution of the olefinic cross-peaks of unsaturated fatty acids A2) uniformly sampled B2) 4X NUS. The spatial locations of the 2D COSY are highlighted in red and the spectral region of the olefinic cross peaks is highlighted in blue.

spatial distribution. The choice of $\Delta t = 0.8ms$ used to sample the t_1 dimension, provided a spectral bandwidth equal to $1250Hz$ over 100 t_1 points, which prevented any spectral aliasing of the high frequency components through replication of the COSY spectrum in Fourier space. Likewise, the $50kHz$ bandwidth used to sample k_y over 16 increments prevented any spatial features from aliasing within the olefinic spatial distribution.

The 4X NUS data set shows significant spatial-spectral artifacts caused by multiplying the continuous EP-COSI signal by the NUS mask on the left of figure 3.3. This resulted in the convolution of the spatial-spectral domain with the PSF of the NUS sampling pattern, which resembles a δ function at the center frequency surrounded by incoherent broadband noise as illustrated in the bottom row of figure 3.1b. The artifacts are spread along the F_1 and Y dimensions in the COSY spectrum and olefinic spatial distribution, respectively. No artifacts are present in the $F_2 - X$ dimensions because the t_2 and k_x are dimensions are uniformly sampled and orthogonal to the under-sampled $k_y - t_1$ plane. Even though the 4X NUS

data set was sampled at an average rate lower than the Nyquist rate, there are no obvious periodic aliasing artifacts present in the spatial-spectral domain. The NUS artifacts are the result of attenuated aliasing of the Y and F_1 dimensions as discussed in section 3.2, not overlapping, periodic replication of the spatial-spectral signals from sub-Nyquist sampling. Because the NUS PSF does not resemble a comb function, the artifacts are caused by low amplitude replication of the spatial-spectral signals by the broadband noise surrounding the central peak of the PSF. This has the effect of blurring the metabolite peak energy over $Y - F_1$, as illustrated in the bottom row of figures 3.1b and c.

3.5 4D MRSI Sample Mask Creation

3.5.1 2D Poisson-Gap Sample Mask Overview

For any non-linear reconstruction technique to successfully remove under-sampling artifacts, the NUS mask's PSF must have a single dominant central peak with small side-lobes, surrounded by low amplitude, incoherent artifacts, as illustrated in the bottom row of figures 3.1b and c [30, 35]. Therefore, when the sampling PSF is convolved with the Fourier transform of the ideal signals, the incoherent sampling artifacts will have low amplitudes and spurious peaks caused by coherent aliasing will be negligible. Large side-lobes or non-central peaks in the PSF will result in higher signal energy dispersion across the under-sampled dimensions and coherent aliasing that cannot be removed by iterative reconstruction.

Compared to other statistical distributions, Poisson distributed sample masks create the fewest aliasing artifacts and better preserve the SNR of the under-sampled signals in the Fourier domain because their PSFs are closest to the ideal of any distribution as described above [11, 12]. They avoid large gaps between samples, which are detrimental to the reconstruction, while ensuring the samples are randomly distributed [81]. Therefore, the sample masks used on the $k_y - t_1$

planes of 4D MRSI data sets in this dissertation are under-sampled using the Poisson distribution.

The sample masks were generated using a modified 1D Poisson-gap mask creation process [65] by extending it to 2D so the sample masks are Poisson distributed across both the k_y and t_1 dimensions. 1D Poisson-gap mask creation allows for the sampling density to be shaped by an arbitrary modulation function, so that the density follows the time-domain MR signal envelope and samples more points at higher SNR. By following the signal envelope, the sample mask can better preserve the line-shapes and SNRs of metabolite peaks and can provide reconstructions with lower Root Mean Square Errors (RMSE) and non-linearity compared to sample masks that do not [81, 85, 106]. Because the t_1 dimension in a filtered EP-COSI scan has a skewed-sine squared signal envelope and the t_1 dimension in an EP-JRESI scan has an exponentially decaying signal envelope, the 2D Poisson-gap sample masks are modulated along t_1 with sine and exponential decay functions, respectively. The k_y dimension of each sample mask for both scan types is modulated by an exponential decay function to follow the k-space signal envelope and maximize spatial SNR [84].

For this dissertation, the 2D Poisson-gap sample masks use the convention that the gaps between *spaces* follow a Poisson distribution, whereas, the original 1D Poisson-gap sample masks use the convention that the gaps between *sampled points* follow a Poisson distribution. It was found that modulating the removal of samples from the mask to create spaces instead of adding samples to the mask was a more consistent method of producing masks with ideal PSFs at every mask size and NUS rate used. Both conventions result in the gaps between the sample spaces and sample points following local Poisson distributions. [33].

The sample density modulation used to create Poisson-gap sample masks is illustrated by equation 3.3. As can be seen, the rate parameter, λ, in a Poisson distribution is used to determine both its mean and variance. Therefore, the

probability of generating a sample gap, g, from a Poisson distribution can be easily characterized if λ is known:

$$p(g, \lambda) = \frac{\lambda^g \cdot e^{-\lambda}}{g!} \tag{3.3}$$

For large λ, large gaps are more likely, and for small λ, small gaps are more likely. Therefore, the probability of g can be modulated by varying the value of λ according to an arbitrary function of k_y or t_1. This allows the local probability of large gaps between spaces to be increased where the SNR is highest in the MR signal envelope [110]. However, to generate g as a function of λ a Poisson process can be simulated using various techniques that do not depend on *a priori* knowledge of g as above [33]. For this dissertation, the $poissrnd(\lambda)$ function in Matlab was used to generate g as a function of λ. It takes as input an array of λ and returns an array of sample spacing gaps with local mean and variance, λ.

Small fluctuations in the chosen sample points may have adverse effects on the reconstruction because of the random nature of the $k_y - t_1$ sample masks. This is especially true at high NUS rates that allow for very few sample points in the mask. These random fluctuations are minimized in Poisson-gap sampling compared to other distributions [65]; however, a *best mask* empirical heuristic was designed in order to increase the probability that a mask generated using 2D Poisson-gap would be close to the ideal and ensure consistency in the masks produced. Because the PSF of an ideal NUS sampling mask has a dominant central peak surrounded by incoherent broadband noise, the heuristic is based on the PSF of the mask:

$$\mathcal{H} = \sqrt{\alpha_{t_1} \cdot \alpha_{k_y}} \cdot \beta \cdot \gamma \tag{3.4}$$

where α_{t_1} and α_{k_y} are the Full-Width Half-Maximums (FWHM) of the PSF's central peak along t_1 and k_y, respectively, β is the normalized power of the incoherent broadband noise surrounding the central peak, γ is the ratio of the largest inco-

herent peak to the central peak of the PSF, and $\mathcal{H}$ is the heuristic value generated for each sample mask. Empirical observations showed that masks with the smallest $\mathcal{H}$ values resulted in masks with narrow PSFs that had very low amplitude broadband noise surrounding the central peak. Therefore, the most ideal sample masks at each NUS rate and size could be automatically chosen from a large pool of candidates using just the $\mathcal{H}$ value with no user input.

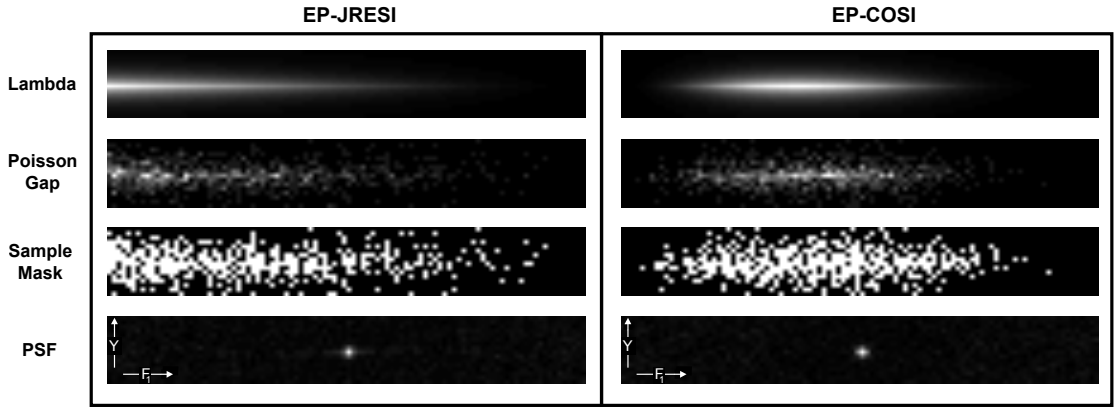

Figure 3.4: Poisson sample mask creation along the $k_y - t_1$ plane for EP-JRESI and EP-COSI. (Top) Exponentially and Sine modulated values for λ along t_1 for EP-JRESI and EP-COSI. (Upper Middle) Poisson distributed values for each λ indicating the sample gap between that space and other spaces in the sample distribution. (Lower Middle) Resulting 2D Poisson-gap sample mask. (Bottom) PSF of the 2D sample mask.

An example of 2D Poisson-gap mask creation is shown in figure 3.4 for the EP-JRESI and EP-COSI pulse sequences with the $k_y - t_1$ plane under-sampled 4X for $k_y = 16$ and $t_1 = 100$. It illustrates the relationships between the $k_y - t_1$ modulated λ values, the Poisson distributed spacing gaps with local mean and variance defined by λ, and the sampling mask derived from the spacing gaps. As the size of λ increases, the spacing gaps increase. As the spacing gaps increase, the sample density increases in that area of the mask because the spaces are further apart. The PSF of each mask is shown and demonstrates the viability of this approach; the single dominant central peak has small side-lobes and is surrounded by low amplitude, broadband noise. Incoherent sampling artifacts from these masks will have low amplitudes and spurious peaks caused by coherent

aliasing will be negligible to non-existent.

3.5.2 2D Poisson-Gap Sample Mask Algorithm

2D Poisson-gap sample masks are iteratively generated in Matlab by combining the 1D distributions of t_1 and k_y until the desired NUS rate over the $k_y - t_1$ plane is reached. The method is not designed to enforce individual NUS rates over k_y and t_1.

Algorithm 3.5.1 shows the pseudocode for 2D Poisson-gap sample mask creation. It takes as input the percent NUS of the $k_y - t_1$ plane, and the lengths of the k_y and t_1 sample dimensions. The algorithm consists of four steps that are repeated until the number of sample points in the mask matches the percent NUS of the $k_y - t_1$ plane:

(i) Calculate the amplitude modulated λ array that follows the signal envelope.

(ii) Calculate the Poisson distributed spacing *gap* array using λ.

(iii) Calculate the sample *mask* array using *gap*.

(iv) Adjust the λ modulation parameters to increase/decrease % NUS in *mask*.

Prior to iterating steps **(i)-(iv)**, the exponential decay rate of the MR signal envelope over k_y is calculated as well as the x and y vectors used to parameterize the t_1 and k_y dimensions. By setting the k_y envelope area equal to the percent NUS in the $k_y - t_1$ plane, the exponential decay rate over k_y that is calculated will provide an average NUS rate over k_y equal to the percent NUS. This rate is used to modulate the sample mask and ensures large spacing gaps have a high probability in the center of k-space.

Algorithm 3.5.1: 2D Poisson-Gap Sample Mask($\%\ NUS, k_y, t_1$)

$r_k \leftarrow \int_0^{k_y} e^{-t \cdot r_k} dt = \%NUS$
$x = \begin{bmatrix} 1 & 2 \cdots t_1 - 1 & t_1 \end{bmatrix}$
$y = \begin{bmatrix} -k_y & -k_y + 2 \cdots k_y - 3 & k_y - 1 \end{bmatrix}$

repeat

(i)
for each y, x
  $\lambda_x = A \cdot sin^2(\pi\,(x/t_1)^{\cdot 7})$ (for EP-COSI)
  $\lambda_x = A - A \cdot sin(\pi\,(x/(2 \cdot t_1)))$ (for EP-JRESI)
  $\lambda_y = e^{|y| \cdot r_k}$
end
$\lambda = \lambda_x / max(\lambda_x) \times \lambda_y / max(\lambda_y)$

(ii)
for each λ
  $gap(i,j) = poissrnd(\lambda(i,j)) + 1$
end

(iii)
$mask = ones(k_y, t_1)$
for each $i \in gap$
  $j = 1$
  while $j < t_1 + 1$
    $mask(i,j) = 0$
    $j = j + gap(i,j)$
  end
end

(iv)
if over % NUS:
  then $A = A \times (1 - \eta)$
  else $A = A \times (1 + \eta)$

until % NUS reached
return $(mask)$

For the λ array calculations in **(i)**, the modulation functions for each dimension are orthogonal in the $k_y - t_1$ plane, such that $\lambda(y(i), x(j)) = \lambda_y(y(i)) \cdot \lambda_x(x(j))$. The k_y modulation is calculated independently of the t_1 modulation, which are then combined into a single function of y and x over the $k_y - t_1$ plane. The choice of t_1 modulation function depends on the pulse sequence used: EP-COSI sample masks are modulated along t_1 using a skewed-sine squared function and EP-JRESI sample masks are modulated along t_1 using a sine function. A sine function is used to model an exponential decay function for EP-JRESI because it provides

more consistent results at all NUS rates and mask sizes than exponential decay functions.

The maximum value of the λ array is governed by the scalar A, which is increased or decreased in step **(iv)** to adjust the number of samples in the $k_y - t_1$ plane so it reaches the desired percent NUS. The adjustment parameter η is defined so that: $0 < \eta < 1$. The decay rate, r_k, used to modulate λ_y across k_y is never updated. The optimal value for r_k has a closed form solution but A must be iteratively modulated until the $k_y - t_1$ plane contains the correct number of sample points.

For each value in the λ array, a sample spacing gap is generated in step **(ii)** with a mean and variance equal to $\lambda(i, j)$ using the Matlab function, $poissrnd()$. Because the gaps are calculated between the sample spaces, not the sample points, $mask$ is initially set to sample every point in the $k_y - t_1$ plane and then uses the gap array in step **(iii)** to determine which points in $mask$ should be set as spaces. The sample point $mask(i, j)$ is initially set to be a space. The corresponding gap value is used to jump to sample point $mask(i, j + gap(i, j))$ and set it as a space. By looping over the k_y and t_1 dimensions and using the gap values to jump between points in the sample mask, the gaps between sample spacings will have local mean and variances determined by λ, which follows the Poisson distribution.

CHAPTER 4

Non-linear Iterative Reconstruction

4.1 Overview

Most early applications of NUS relied on the aliased energy of the artifacts to be far less than the energy of the signals of interest [110]. There was no general framework available to remove NUS artifacts that could be easily implemented. Filters could be used to remove artifacts but distorted the signals of interest [30, 35]. When Total Variation (TV) image denoising was introduced, it could be used to remove many of the artifacts, but it worked most effectively with data that was piece-wise constant, such as images, and was originally intended for denoising, not reconstruction [103]. Maximum Entropy (MaxEnt) reconstruction was one of the first general purpose reconstruction algorithms developed that allowed for arbitrary NUS patterns and could be applied to many different types of data and sampling conditions [46, 114]. It found widespread use on NMR experiments that could typically last for days when fully sampled but were reduced to a fraction of the time when NUS was applied [3, 106]. Recently, the development of the theory of Compressed Sensing (CS) and the numerous non-linear algorithms designed to remove the NUS artifacts has lead to much more widespread use of NUS in many areas of research beyond traditional signal and image processing [21, 36].

This chapter provides background on CS and MaxEnt reconstruction theory, we well as a detailed discussion of the Cambridge algorithm that was developed to solve the MaxEnt reconstruction problem. The Cambridge algorithm was only

partially documented in literature, therefore, the missing elements had to be designed as part of this dissertation.

4.2 Sparsity and Compressed Sensing Reconstruction

Compressed Sensing (CS) exploits the fact that most data is compressible in some transform domain and can be represented by fewer samples than is dictated by the Nyquist rate if certain conditions are met. Given $m < n$ measurements of an unknown vector x of length n, the fully sampled vector can be reconstructed exactly if it is compressible in some transform domain, such as the Fourier, Wavelet, or TV, by minimizing the ℓ_1-norm of the transform coefficients while maintaining fidelity with the sampled points [21, 36]. Minimizing the ℓ_1-norm in the transform domain, attempts to compress the data into as few transform coefficients as possible, such that any artifacts from NUS are removed. CS theory dictates the reconstruction can be made from any random selection of samples that obey the restricted isometry property and are totally non-adaptive [21]. Including adaptive samples, which are measurements made in response to other measurements, does little to improve the reconstruction results as is done in other greedy algorithms [52, 122]. A random sampling mask that obeys the restricted isometry property will approximately preserve the norms of a sparse vector to which it is applied, suggesting the signal energy must be partially preserved by NUS [23].

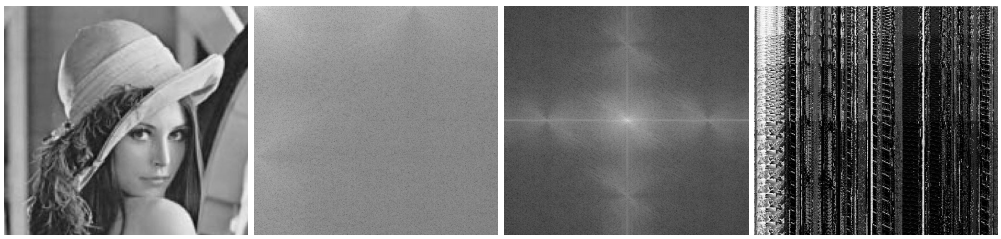

Figure 4.1: Transform domain sparsity of an image. Left to right: Original image, Discrete Cosine Transform (DCT) of image, Discrete Fourier Transform (DFT) of image, and Discrete Wavelet Transform (DWT) of image using Haar wavelets.

Figure 4.1 illustrates the principal of transform sparsity of an image using the Discrete Cosine Transform (DCT), Discrete Fourier Transform (DFT), and Discrete Wavelet Transform (DWT) with Haar wavelets from left to right. Transform sparsity is the necessary condition that a signal is represented by the fewest non-zero coefficients in a transform domain by being compressible in that domain. As can be seen, the original image is not sparse in the image domain or in the Cosine domain. Sparsity is greater in the Fourier domain, but the sparsest representation of the image is in the Haar Wavelet domain which has the fewest non-zero transform coefficients of each domain. Sparsity is decreased by NUS sampling artifacts because they manifest as broadband noise in the transform domain, making fewer coefficients non-zero. By enforcing sparsity of the NUS signal in the transform domain and compressing it into the fewest number of coefficients, minor coefficients which are representative of NUS artifacts are removed and the fully sampled signal can be reconstructed in the sample domain.

CS reconstruction has three main requirements for it to be successfully applied [80]:

1. Transform sparsity: the data should be compressible and have a sparse representation in a known transform domain. Generally, the sparser it can be represented, the fewer samples are needed for the reconstruction. [20]

2. NUS aliasing artifacts must be incoherent: under-sampling artifacts are noise-like in the transform domain and are not the result of sub-Nyquist aliasing.

3. Non-linear reconstruction methods must be used: the data should be reconstructed using a non-linear method that enforces sparsity in the transform domain while maintaining fidelity with the measured samples.

When applied to 4D MRSI, CS maximizes the transform sparsity of the recon-

struction by solving the constrained convex optimization problem:

$$\begin{aligned} \min_{\hat{f}} \quad & \|\psi \hat{f}\|_0 \\ \text{s.t.} \quad & R\mathcal{F}\hat{f} = d \end{aligned} \tag{4.1}$$

where $\hat{f}$ is the spatial-spectral domain reconstruction, ψ is a known sparsifying transform, R is the NUS mask, d is the measured data in the k-space, time domain, $\mathcal{F}$ is the Fourier transform, and $\|\psi \hat{f}\|_0$ is the ℓ_0-norm of the data in a sparse domain [37]. For this dissertation, the NUS 4D MRSI data is reconstructed by CS using the identity transform domain, $\psi = I$. The mixed-domain $k_y - t_1$ plane is self sparse and a sparsifying transform is not required represent the 4D MRSI data in its sparsest representation [50].

The ℓ_0-norm is a direct measure of transform sparsity, however, solving equation 4.1 is an NP-hard combinatorial problem and must be relaxed to the ℓ_1-norm to be solved [37]:

$$\begin{aligned} \min_{\hat{f}} \quad & \|\psi \hat{f}\|_1 \\ \text{s.t.} \quad & ||R\mathcal{F}\hat{f} - d||_2^2 <= \sigma \end{aligned} \tag{4.2}$$

where σ is the noise standard deviation and is added as an additional relaxation to the CS problem to accommodate noisy measurements, where only non-exact reconstruction is possible to within the noise power of the sample data [21]. As Donoho showed, equation 4.2 is equivalent to equation 4.1 and solves the CS reconstruction problem. The minimum ℓ_1-norm of an under-determined system of equations, such as NUS data, is the sparsest, unique solution of the data decomposition into its transform domain coefficients [27, 37]. By solving this problem, the sparsest, unique representation of the sampled data in the transform domain can be found in polynomial time [23].

CS has been successfully applied to MRI [79], dynamic MRI [51], MRSI [50,62], and many other medical imaging modalities. Its popularity can partially be ex-

plained by the ease with which equation 4.2 can be solved. The minimum ℓ_1-norm of a vector has a closed form solution that is simple and fast to compute, so each iteration of the reconstruction can be solved quickly by the *shrink* operation [121].

Equation 4.2 is typically solved by first converting it to an unconstrained convex problem:

$$\min_{\hat{f}} \quad \|\hat{f}\|_1 - \lambda||R\mathcal{F}\hat{f} - d||_2^2 \tag{4.3}$$

where λ is a Lagrange multiplier that determines the point in the solution space of $\hat{f}$ where the feasible set of solutions tangentially intersects with the objective function (i.e., the minimum ℓ_1-norm of the solutions that satisfy the constraint). Figure 4.2 illustrates the solution to a convex optimization problem using Lagrange multipliers for the MaxEnt reconstruction problem, which is similar to CS. When the *shrink* operation is applied to equation 4.3 to solve for the minimum ℓ_1-norm at each iteration, the solution is dependent on the value of λ whose optimal value is not known *a priori*. There are numerous algorithms that have been developed to determine the optimal λ during reconstruction, including Interior Point methods [72], Gradient Projection methods, [43], and Alternating Direction Methods of Multipliers such as the Split-Bregman algorithm [55]. Conjugate gradient optimization has been used to solve equation 4.3 given a specific value for λ that is empirically determined [79]. A number of high quality solver implementations are available for download that were designed as general solvers capable of solving equation 4.3, such as PDC0 [105], and CVX [15], or were designed specifically to solve the problem, such as l_1-magic [22].

For this dissertation, the CS reconstruction problem is solved using either the Cambridge algorithm, which is described in detail in section 4.4; or the Split-Bregman algorithm, which is described in chapter 6. Results for the CS reconstruction of 4D MRSI data are provided in chapters 5 and 6.

4.3 Maximum Entropy Reconstruction

4.3.1 Entropy and the Maximum Entropy Distribution

Entropy as a measure of information content was first proposed by Claude Shannon in 1948 [109]. His goal was to develop a statistical model of a discrete information source in order to reduce the required capacity of a transmission channel through the use of the right data encoding. By knowing *a priori* the probability of each possible state of a variable or combination of those variables, he could design an encoding based on those probabilities that compresses the variables and uses the smallest bandwidth.

According to Shannon, the average entropy of a variable must be used as a measure of the minimum number of bits needed to transmit each variable state based on their frequency of occurrence. Low entropy states have a higher probability and need fewer bits to transmit. Higher entropy states have a lower probability and need more bits to transmit. For example, in English language text, the states *A*,*E*, and *T* have a higher probability of occurring than *Q*, *W*, and *Z*, and should therefore be represented by fewer bits using an entropy compressed encoding scheme. Text compression is most efficient when the most frequent letters are represented by the fewest bits.

The entropy of a variable x, with discrete states $\{x_1, x_2, x_3...x_N\}$ and probabilities per state $p = \{p_1, p_2, p_3...p_N\}$, such that $\sum_{i=1}^{N} p_i = 1$, is defined as:

$$S\left(p_1, p_2, p_3...p_N\right) = -K \sum_{i=1}^{N} p_i \cdot log(p_i) \tag{4.4}$$

where K is a scaling factor typically set to 1 [109]. This equation alone satisfies the three criteria Shannon described for a measure of discrete information compression that he used to derive this result [109]:

1. S should be continuous in p_i.

2. S should be a monotonically increasing function of N if all $p_i = 1/N$.

3. If a choice of variable states is split into multiple choices, the original S should be the weighted sum of the S of each choice.

Equation 4.4 can be derived more formally than Shannon's approach if we borrow from Edwin Jaynes and use a more intuitive approach based on combinatorics [67]. Consider a photographic plate separated into a grid of M cells with N photons incident onto the plate. This is a discrete Poisson process where the number of photons in the i^{th} cell is n_i. If the probability of a photon incident onto a cell is independent of the photon order, the probability of a photon entering the i^{th} cell is $p_i = \frac{n_i}{N}$. The number of realizations of this process for a given distribution $p = \{p_1, p_2, p_3 ... p_N\}$ can be described by the multiplicity factor, W:

$$W = \frac{N!}{(n_1!)(n_2!)(n_3!)...(n_M!)} \tag{4.5}$$

where we can remove the factorial terms from W by using the fact that it is a monotonically increasing function of p:

$$\underset{p}{\operatorname{argmax}} \log W(p) \equiv \underset{p}{\operatorname{argmax}} W(p) \tag{4.6}$$

Using Sterling's approximation, ($\log N! = N \log N - N$), the factorial terms are removed and W can be expressed in terms of p:

$$N_{-1} \log W = -\sum_{i=1}^{M} p_i \cdot log(p_i) \tag{4.7}$$

Equation 4.7 is directly proportional to equation 4.4, the equation for entropy, which indicates the entropy of this process is merely a scaled version of the multiplicity.

By solving $\max_{p} W(p)$ as an unconstrained optimization problem, we can find the distribution $\hat{p}$ that has the greatest multiplicity and can be formed the most number of times by different combinations of p_i. Since $\hat{p}$ occurs the most frequently out of all distributions, it is the maximum entropy distribution [67, 68].

The distribution $\hat{p}$ that maximizes equation 4.5 is the normal distribution: $p = \{1/M, 1/M, 1/M, ...1/M\}$, which indicates the probability that a proton is in any of the M cells is the same. This corresponds to the maximum uncertainty of a proton in each of the M cells and is a totally unbiased process. If we had prior knowledge of any p_i before calculating the multiplicity of this process, the maximum value would be lower than if we had no knowledge of the probability distribution across the M cells; the values of p_i that we knew would not change and the possible number of combinations of p_i would decrease as a result.

The maximum entropy distribution changes given any prior knowledge of a discrete process [69]. If we are given the mean and standard deviation of a process and the possible values from the process can be any real number, the maximum entropy distribution is the Gaussian distribution, if we know the possible values of the process are positive and are given its mean, the maximum entropy distribution is the exponential distribution, and if we only know the possible values are within a given range, and have no knowledge of the process's statistical moments, the maximum entropy distribution is the uniform distribution as described above. This prior knowledge biases our estimate of the maximum entropy distribution for our process, such that $\max_{p} W(p)$ goes from being an unconstrained to a constrained optimization problem. The constraints limit the set of solutions, $\hat{p}$, to only those distributions that conform to the prior knowledge.

By limiting $\hat{p}$ to a set of distributions that match some some known information about a discrete process, the principle of maximum entropy (MaxEnt) can be used to estimate the values from the distribution about which we know nothing [18,46]. As stated above, maximizing the entropy of a discrete process results in the most

statistically likely distribution based on what we know about that process. It makes no assumptions about correlations between values that are not explicitly provided in the form of an optimization constraint [113].

4.3.2 Maximum Entropy Reconstruction in NMR and MRSI

Applying the MaxEnt estimation problem to 4D MRSI reconstruction is fairly straightforward. Any knowledge we have of the spectrum, in the form of sampled points, can be formulated as a convex constraint that biases the MaxEnt distribution towards the fully sampled spectrum. It doesn't matter that the spectrum isn't a probability distribution; the values in the spectrum can be made to resemble a probability distribution by normalizing the spectrum to unit energy, or the values can be used as is, the MaxEnt formalism will not be violated [113].

MaxEnt reconstruction can be formed as a convex optimization problem with a fidelity constraint between the sampled points and the reconstructed data:

$$\begin{aligned} \max_{\hat{f}} \quad & S(\hat{f}) \\ \text{s.t.} \quad & \tfrac{1}{2}||R\mathcal{F}\hat{f} - d||_2^2 <= \sigma \end{aligned} \tag{4.8}$$

where $\hat{f}$ is the reconstructed data, $S(\hat{f})$ is the entropy of $\hat{f}$, d is the sampled data, $\mathcal{F}$ is the Fourier transform, R is the NUS matrix, and σ is the standard deviation of the noise. By applying the Fourier transform to time-domain samples in the constraint equations, correlations among all of the frequency-domain points can be explicitly enforced in the problem by very few points in the time-domain. By its nature as an orthogonal basis, the Fourier transform correlates each point in the time-domain with every point in the frequency-domain when applied to the time-domain sampled points.

MaxEnt estimation as shown in equation 4.8 has been used to estimate missing data points in noisy or incomplete images, NMR spectra, and other types of

data sets [8, 57, 111]. It can be applied to problems with very few points in one-dimension up to large scale optimization problems with millions of points in n-dimensional data sets [17]. However, there is no analytical solution to the MaxEnt estimation problem so non-linear, iterative techniques must be used [16]. This poses a problem as MaxEnt is used to estimate missing values from large, high-dimensional data sets; as the number of data points and dimensions increase, the amount of computer memory and computation time required to compute the solution increase quickly. Any algorithms used to solve the MaxEnt problem must avoid matrix-matrix operations and reduce the number of Fourier transformations per iteration because of their high computational requirements.

A robust and scalable algorithm that made MaxEnt reconstruction a practical option for large scale, high dimensional data sets was developed by Skilling and Bryan at the University of Cambridge in 1984 and was initially used to reconstruct astronomical images [114], but was applied to NMR data sets within a few years [75]. Their algorithm uses a variant of the linear conjugate gradient method to iteratively solve the problem:

$$\max_{\hat{f}} S(\hat{f}) - \lambda ||K\mathcal{F}\hat{f} - d||_2^2 \tag{4.9}$$

where the Lagrange multiplier, λ, has been introduced to make the problem an unconstrained convex optimization problem. The Cambridge algorithm is described in detail in section 4.4. Figure 4.2 shows a 2D projection of the solution space for a 5-point spectrum. If the contour lines represent different values of entropy, the point $\mathbf{Y}$ is the maximum entropy point for the entire solution space. If $\mathbf{X}$ represents the set of feasible solutions determined by the constraint, then their tangential intersection at $\mathbf{Z}$ is the MaxEnt solution to the problem.

The Cambridge MaxEnt algorithm was initially intended for imaging applications, so the spectrum was assumed to be real and positive which is a necessary

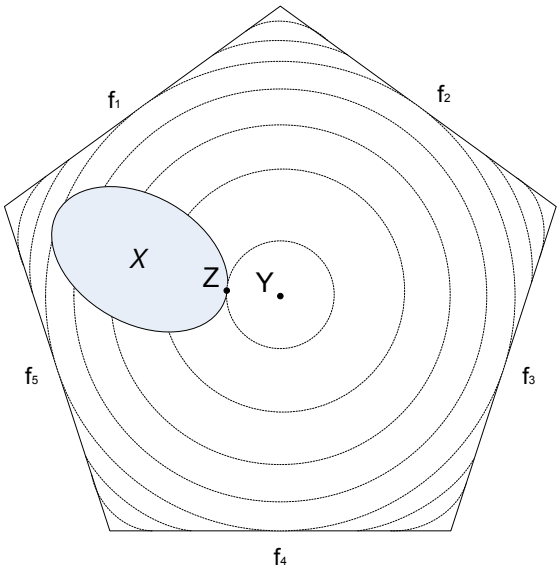

Figure 4.2: A 2D projection of a 5-point MaxEnt solution space. **X** is the constrained region of the solution space. **Z** is the maximum entropy point within the feasible set. **Y** is the maximum entropy point of the entire solution space.

assumption for the entropy of the spectrum to be defined [17, 57, 114]. However, NMR spectra are neither always real nor positive, so modifications to the entropy function had to be made in order to accommodate imaginary and negative components.

Hoch et al used the absolute magnitude of each spectral point, $|f_i|$, in place of each complex f_i, so the entropy at each point was calculated as [59]:

$$S_2 = -|f_i| \log |f_i| \tag{4.10}$$

This yielded a fully sampled 2D power spectrum estimate, however, all phase information was lost in the spectrum so the technique could not be applied to phase sensitive sequences.

Laue et al. addressed the negative, complex value problem by separating the real and imaginary components of each spectral point into a negative and a positive element, such that: $\Re(f) = f^+ - f^-$ and $\Im(f) = f^i - f^{-i}$ where

$\{f^+, f^-, f^i, f^{-i} \geq 0\}$. Any negative values could be wrapped into a larger f^- or f^{-i} element and the real and imaginary components were treated separately [75]. Therefore, the entropy of each spectral point was calculated as:

$$S_4 = -f^+log(f^+) - f^-log(f^-) - f^ilog(f^i) - f^{-i}log(f^{-i}) \tag{4.11}$$

These efforts to find a suitable form for the entropy of a spectrum may have made it possible to mathematically compute the entropy, however, there was no statistical basis for these formulae and therefore, they no longer solved for the maximum entropy distribution of the spectrum [29]. The underlying physical processes that produce the NMR spectrum are not based on particle, or discrete, events so they can not be modeled by simple Poisson processes as required for the derivation of the $f_i \log(f_i)$ form of entropy [48, 49]. They are governed by much more complex quantum mechanical processes that are determined by the spin systems under investigation. Therefore, because NMR signals are not governed by a Poisson process, the multiplicity can not be calculated as in equation 4.5 and the resulting entropy equation must be different than what is commonly used for many image processing applications.

A suitable expression for the entropy of NMR spectra originating from spin-$\frac{1}{2}$ nuclei, such as ^{1}H used in MRS and MRSI *in vivo*, was derived by Daniell and Hore [31]:

$$\begin{aligned} z &= \frac{|\hat{f}|}{def} \\ S_{1/2}(\hat{f}) &= -\sum_{i=1}^{N} \left(z_i \log\left(\frac{z_i + \sqrt{4+z_i^2}}{2} \right) - \sqrt{4+z_i^2} \right) \end{aligned} \tag{4.12}$$

where def is a scaling parameter related to the sensitivity of the scanner. It was derived from first principles using both a classical spin model and a quantum mechanical model. Neither model made any assumptions on the initial state of the

spin system nor the pulse sequence used. For their classical model, they derived the entropy of the spectrum from the distribution of nuclear spins as a function of orientation and frequency, and for their quantum mechanical model, they derived the entropy as a function of the density operator, which describes, in a statistical sense, all of the physically measurable information about an ensemble of spins [1].

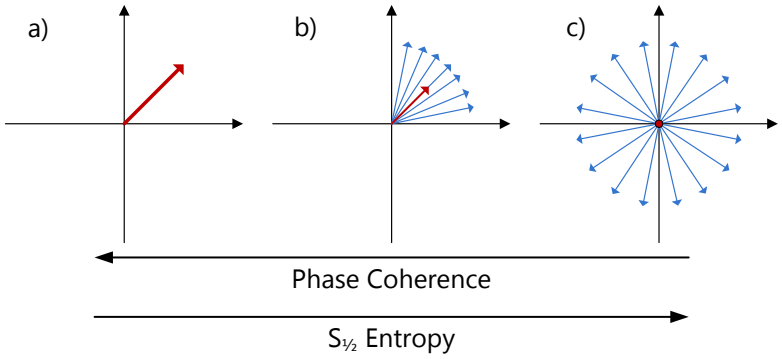

Figure 4.3: Relationship between spin phase coherence (blue), net magnetization (red), and entropy **a**) Full phase coherence has maximum net magnetization and lowest entropy. **b**) Moderate phase coherence has some net magnetization and entropy. **c**) Full phase decoherence has no net magnetization and maximum entropy.

For both of these models, a simplified view of the entropy of an NMR spectrum can be seen in figure 4.3. The directly measurable signal is the red arrow and represents the net magnetization for an ensemble of spins. The blue arrows represent the phase of individual spins within the ensemble. Figure 4.3c shows a state of no phase coherence which has almost zero net magnetization and no measurable signal. Because the phase distribution within the ensemble is normally distributed, our uncertainty of the ensemble phase is the greatest and so is the entropy. Figure 4.3a shows a state of full phase coherence where the net magnetization is greatest and the phase distribution is completely known; there is no uncertainty of the ensemble phase, so the entropy is low. Therefore, for NMR spectra, high-amplitude signals represent a state of full phase coherence with low entropy, and low amplitude signals represent states of lower phase coherence with high entropy; this suggests spin-$\frac{1}{2}$ entropy conforms to Jayne's Principle of Max-

imum Entropy whereby the highest entropy state is one of total uncertainty [67].

A comparison of the three entropies used in NMR defined by equations 4.10,4.11, and 4.12 was performed by Hoch [60]. It was found that spin-$\frac{1}{2}$ entropy was superior to the other entropy functions when the maximum entropy reconstruction was compared against the full spectrum, and in terms of it being indifferent to phase distortions in the spectrum. Therefore, the use of spin-$\frac{1}{2}$ entropy in maximum entropy reconstructions has both a theoretical and practical justification, and has been used as the entropy function in this disseration research.

4.4 Cambridge Algorithm

During this discussion of the Cambridge algorithm, the MaxEnt reconstruction problem is defined as: $Q = S(\hat{f}) - \lambda C(\hat{f})$ where $C(\hat{f})$ is the residual constraint and $S(\hat{f})$ is the spin-$\frac{1}{2}$ entropy as defined in equation 4.12.

Traditional conjugate gradient methods solve for the optimal point in an optimization problem by iteratively stepping through the solution space along a single vector, or search direction, at each iteration. Among all of the iterations, these vectors are conjugate to each other with respect to the data (i.e, $x_i^T A x_{i+1} = 0$ for some matrix A at iterations i and $i+1$, and search directions x_i and x_{i+1}), so at each iteration, the problem is solved along a single dimension. For a dataset of N dimensions there should be N iterations of the conjugate gradients algorithm.

Skilling and Bryan's Cambridge algorithm is a variant of conjugate gradient methods, but is different in four major ways [17, 114]:

1. The algorithm has no memory between iterations, so the search direction chosen at iteration i may not be completely conjugate to the search direction at iteration $i+1$. This is because the solution space for the combined entropy and quadratic constraint functions is highly non-quadratic, so it cannot be

assumed to have constant curvature as in traditional conjugate gradients. Assuming constant curvature places a severe restriction on the step-size at each iteration that decreases efficiency of the algorithm.

2. The solution space is bent by an *entropy metric* so that it is no longer Cartesian. The distance between large values of f_i is reduced while the distance between small values of f_i is increased, while in a Cartesian space they are uniform. This is done in order to reduce the dependence of the $log(f_i)$ term in the entropy on changes to small values of f_i. In a Cartesian space, changes to small f_i affect the curvature of the solution space disproportionately higher than changes to large f_i, because of the curvature's dependence on $\frac{1}{f_i}$ terms, and the entropy metric attempts to balance this so changes to the curvature are minimized between iterations.

3. The algorithm steps through the solution space for the maximum entropy point via a subspace spanned by four or more search directions instead of just one, as is done in traditional conjugate gradients. The search directions are formed by the gradients and Hessians of $S(\hat{f})$ and $C(\hat{f})$, modified by the entropy metric so the subspace is non-Cartesian but has pseudo-quadratic curvature. They are then used to form a local, second-order approximation to the maximization problem at the current iteration.

4. The algorithm implicitly solves for the optimal value of λ while traditional conjugate gradient methods can not accommodate Lagrange multipliers. λ is not solved for explicitly, but a local approximation to its value is solved for within the subspace spanned by the four or more search directions. The local λ, called α, is found by a simple line search for the value which maximizes the entropy while minimizing the constraint within the subspace. By iteratively solving for α, the global maximum entropy point that satisfies $C(\hat{f})$ is found without ever having to calculate λ explicitly.

Algorithm 4.4.1: CAMBRIDGE MAXENT$(d, mask)$

Calculate C_0 and def from d:

$$\begin{cases} C_0 = std(noise) \\ def = \sqrt{\dfrac{C_0}{N}} \\ \hat{f} = 0 \end{cases}$$

repeat

Calculate gradients and hessians:

$$\textbf{(i)} \begin{cases} g_c = \nabla C(\hat{f}),\ g_s = \nabla S(\hat{f}), \\ H_s = \nabla^2 S(\hat{f}),\ H_c = \nabla^2 C(\hat{f}), \\ E_s = -H_s^{-1} = \text{Entropy metric} \end{cases}$$

Calculate search directions to form basis:

$$\textbf{(ii)} \begin{cases} b_1 = \dfrac{g_s}{\|g_s\|_2} - \dfrac{g_c}{\|g_c\|_2} \\ b_2 = E_s g_c, \\ b_3 = E_s g_s, \text{(phase=1 only)} \\ b_4 = g_c, \\ b_5 = E_s H_c E_s \left(\dfrac{g_s}{\|g_s\|_2} - \dfrac{g_c}{\|g_c\|_2} \right) \end{cases}$$

Create local 2^{nd} order approximation from basis:

$$\textbf{(iii)} \begin{cases} S(y) = S(\hat{f}) + y^* b^* g_s - \dfrac{1}{2} y^* b^* H_s \, b \, y \\ C(y) = C(\hat{f}) + y^* b^* g_c + \dfrac{1}{2} y^* b^* H_c \, b \, y \end{cases}$$

Rotate basis to make subspace Cartesian:

$$\textbf{(iv)} \begin{cases} y \Rightarrow x,\ b^* H_s \, b \Rightarrow I,\ b^* H_c \, b \Rightarrow M_{diag} \\ S(x) = S(\hat{f}) + x^* b^* g_s - \dfrac{1}{2} x^* I x \\ C(x) = C(\hat{f}) + x^* b^* g_c + \dfrac{1}{2} x^* M_{diag} x \end{cases}$$

Find x that minimizes C(x) and maximizes S(x) from (iv):

$$\textbf{(v)} \begin{cases} x(\alpha) = \dfrac{M_{diag} + \alpha I}{\alpha b^* g_s - b^* g_c} \\ x = \underset{x(\alpha)}{\operatorname{argmin}} \, C(\hat{f}) + g_s^* b \, x(\alpha) + \frac{1}{2} x(\alpha)^* M_{diag} x(\alpha) \end{cases}$$

Update spectrum and determine phase:

$$\textbf{(vi)} \begin{cases} \hat{f} = \hat{f} + b^T x \\ C(\hat{f}) \leq C_0 \Rightarrow C(\hat{f}) = C_0 \text{ and phase=2} \end{cases}$$

until stopping condition met

return $(\mathcal{F}^{-1} \hat{f})$

Pseudocode for the Cambridge algorithm used to solve the 4D MRSI MaxEnt reconstruction problem is shown in Algorithm 4.4.1. It takes as input the NUS k-space, time domain data d and the sampling mask and returns the reconstructed 4D data set $\hat{f}$. As can be seen, the algorithm repeats six distinct steps for each iteration until the stopping condition is reached and the maximum entropy reconstruction has been found. Specific details on the variables and calculations, as well as required modifications to accommodate complex integers can be found in [61].

The algorithm runs in two phases: phase 1 minimizes the fidelity constraint until the standard deviation of the noise (C_0) is reached and phase 2 maximizes the entropy while maintaining the fidelity constraint at C_0. The reconstruction is initialized to zeros prior to iterating over steps **(i-vi)**.

At step 4.4.1**(i)**, the gradients of $S(\hat{f})$ and $C(\hat{f})$ are calculated as well as the Hessian of $S(\hat{f})$ and the entropy metric used to bend the solution space [61]. The entropy metric is the inverse of the $S(\hat{f})$ Hessian, so numerical issues must be taken into consideration when it is calculated. However, because the Hessian is 2x2 block diagonal it is simple to compute.

At step 4.4.1**(ii)**, the search directions are calculated for the current iteration from the gradients and entropy metric from step 4.4.1**(i)**. During phase 1, there are five search directions used and during phase 2, only four of the directions are used. Most of the search directions are modified by the entropy metric, which was calculated as the inverse of the $S(\hat{f})$ Hessian in the previous step. Each of the ℓ_2 norms is also modified by the entropy metric, such that $\|x\|_2 = \sqrt{x^T E_s x}$. Modifying the search directions and ℓ_2 norms with the inverse of the $S(\hat{f})$ Hessian normalizes the distance between points in the subspace by the curvature at each point, which has the effect of "linearizing" the curvature of the subspace so it resembles that of a more quadratic function (i.e., the Hessian of a quadratic function is a constant which means its curvature is a constant). This biases the

algorithm towards modifying large values of f_i over small values of f_i as well as making the 2^{nd} order-approximation in step **(iii)** possible.

Once the search direction vectors are created in step 4.4.1**(ii)**, they are normalized to be unit length. At this point, a pseudo-quadratic subspace is formed by the basis vectors, $b_1 - b_5$, within the larger solution space for $\hat{f}$. It is within this smaller subspace that a local maximum entropy point can be found. By solving for the local maximum entropy point within the subspace at each iteration and updating $\hat{f}$ to this point, the reconstruction incrementally approaches the global maximum entropy solution.

The 2^{nd} order Taylor expansions of $S(\hat{f})$ and $C(\hat{f})$ are taken within the pseudo-quadratic subspace in step 4.4.1**(iii)**. The Taylor expansions allows us to estimate, based on the curvature of the subspace, where the maximum entropy point is located at this iteration and what the step sizes, y, along each basis vector should be. However, because the metrics, $b^* H_s b$ and $b^* H_c b$, used to form the quadratic part of the expansion are non-Cartesian (i.e., off diagonals are non-zero), the step sizes are coupled to each other and solving for them is non-trivial. Therefore, in step 4.4.1**(iv)** the coordinate system within the subspace is rotated to be Cartesian, such that $b^* H_s b \rightarrow I$ and $b^* H_c b$ are diagonalized. This requires a variable substitution such that: $y \rightarrow x$, $S(y) \rightarrow S(x)$, $C(y) \rightarrow C(x)$.

In step 4.4.1**(v)**, the step sizes, x, within the Cartesian basis are solved for that update the spectrum towards the maximum entropy reconstruction. They are obtained by setting $\nabla_{\hat{x}}(Q(x)) = \nabla_{\hat{x}} S(x) - \alpha \nabla_{\hat{x}} C(x) = 0$, which parameterizes x as a function of α. Because $C(x)$ is a quadratic function of x and x is a function of α, a target value of $C(x)$ can be attained by using a simple line search on α. Typically, the minimum value of $C(x)$ within the subspace is not used as the target because the subspace is only an approximation to the global solution space, so a value slightly larger than $C(x)_{min}$ is used. Further, when the algorithm reaches a point where $C(x)$ is on the order of the noise power, it is not appropriate to push

$C(x)$ below the noise floor. Therefore, the target value used is the greater of the noise power and a value slightly greater than $C(x)_{min}$.

Once the vector x is determined, the reconstructed spectrum is updated in step 4.4.1**(vi)**. If the fidelity constraint is less than C_0, the algorithm enters phase 2 and the fidelity constraint is explicitly set to C_0 until the algorithm finishes. The algorithm runs until the stopping condition, $\frac{g_s}{\|g_s\|_2} - \frac{g_c}{\|g_c\|_2} \leq 10^{-4}$, is met which indicates the gradients of $S(\hat{f})$ and $C(\hat{f})$ are parallel. This is point is the intersection of the spin-$\frac{1}{2}$ entropy with the feasible set of solutions for $\hat{f}$ and was found without having to calculate a value for the Lagrange multiplier, λ.

CHAPTER 5

Maximum Entropy Reconstruction

This chapter is a published manuscript that was written as part of this dissertation research. It is reproduced in full with only the formatting changed to match the dissertation style.

B. Burns, N. Wilson, J. Furuyama, and M. Thomas, "Non-Uniformly Under-Sampled Multidimensional Spectroscopic Imaging *in vivo*: Maximum Entropy versus Compressed Sensing Reconstruction," *NMR in Biomedicine*, vol 27, 2013.

5.1 Abstract

The Four-Dimensional (4D) Echo Planar Correlated Spectroscopic Imaging (EP-COSI) sequence allows for the simultaneous acquisition of two spatial (k_y, k_x) and two spectral (t_2, t_1) dimensions *in vivo* in a single recording. However, because its scan time is directly proportional to the number of increments in the k_y and t_1 dimensions, a single scan take 20 to 40 minutes using typical parameters, which is too long to be used for a routine clinical protocol. The present work describes efforts to accelerate EP-COSI data acquisition by applying non-uniform under-sampling (NUS) to the $k_y - t_1$ plane of simulated and *in vivo* EP-COSI data sets and using Maximum Entropy (MaxEnt) and Compressed Sensing (CS) to reconstruct missing samples. Both reconstruction problems were solved using the Cambridge algorithm, which offers many work flow improvements over other l_1-*norm* solvers. Reconstructions of retrospectively under-sampled simulated

data demonstrate the MaxEnt and CS reconstructions successfully restore data fidelity at SNRs from 4 to 20 at 5X to 1.25X NUS. Retrospectively and prospectively 4X undersampled 4D EP-COSI *in vivo* data sets show both reconstruction methods successfully remove NUS artifacts; however, MaxEnt provides reconstructions equal to or better than CS. Our results show that NUS combined with iterative reconstruction can reduce 4D EP-COSI scan times by 75% to a clinically viable 5 minutes *in vivo* with MaxEnt being the preferred method.

5.2 Introduction

Changes in metabolite concentrations due to the altered metabolism of cancer can potentially be detected non-invasively using one-dimensional (1D) magnetic resonance spectroscopy (MRS) *in vivo* [7, 54, 119]. However, the overlap of spectral peaks in 1D MRS is a major impediment to identifying individual metabolites. Two dimensional (2D) MRS has increased spectral dispersion over 1D MRS and can disentangle overlapping complex spectral peaks [2]. Single vowel 2D MRS has been shown to increase the specificity and sensitivity of tumor grade classification when used with dynamic contrast enhanced (DCE)-MRI in the breast [77]. However, acquiring multiple t_1 increments per voxel to form the second spectral dimension limits its ability to provide multi-voxel coverage due to the long scan times needed to combine two spectral and two spatial dimensions.

With the advent of Echo-Planar Spectroscopic Imaging (EPSI), magnetic resonance spectroscopic imaging (MRSI) scans with one spectral and two spatial dimensions could be completed within clinically acceptable times by interleaving the acquisition of a spatial and spectral dimension within the EPSI readout [83,86,97]. The 4D Echo Planar Correlated Spectroscopic Imaging (EP-COSI) [78] sequence allows the acquisition of two spatial (k_y, k_x) and two spectral (t_2, t_1) dimensions in a single recording to form 4D MRSI. The sequence interleaves the acquisition of the k_x and t_2 dimensions within the EPSI read-out, but k_y and t_1 are incrementally acquired as indirect dimensions during each TR. The EP-COSI sequence has the benefits of increased spectral dispersion

and multi-voxel support, which improves metabolite identification over multiple spatial regions simultaneously; however its scan time is directly proportional to the number of increments in the k_y and t_1 dimensions. An EP-COSI scan using typical parameters of TR/TE= $1.5s/30ms$ and $k_y/t_1 = 16/100$ can take 20 to 40 minutes, which is too long to be used within a routine clinical protocol.

When the Fast Fourier Transform (FFT) is used to transform uniformly sampled 4D MRSI data (k_y, k_x, t_2, t_1) to the spatial-spectral domain (Y, X, F_2, F_1), decreasing scan times requires reducing either the k_y spatial or t_1 spectral dimensions through truncation or lower sampling rates, and a corresponding unwanted reduction in resolution or bandwidth. However, non-uniform under-sampling (NUS) of the spatial, spectral $k_y - t_1$ plane in combination with iterative non-linear reconstruction can be used to accelerate the collection of 4D MRSI data *in vivo* while preserving the spatial and spectral resolutions and bandwidths [50].

Earlier work has demonstrated the feasibility of under-sampling the mixed-domain $k_y - t_1$ plane of a 4D Echo-Planar J-Resolved Spectroscopic Imaging (EP-JRESI) data set and reconstructing the missing points with Compressed Sensing (CS) [50], a popular method of non-linear iterative image reconstruction that promotes data sparsity in the reconstruction domain and data fidelity in the sample domain [23, 36]. The nature of spatial, spectral NUS artifacts in the $k_y - t_1$ plane were explored, and it was shown that l_1-*norm*-based CS reconstruction is a viable means of reducing the scan times of 4D EP-JRESI *in vivo* through NUS. In recent years, CS reconstruction has been successfully applied to under-sampled MRI [14, 79], 3D MRSI [62], and dynamic MRI [51].

Maximum Entropy (MaxEnt) image reconstruction is an alternative non-linear iterative reconstruction technique to CS. Rather than minimizing transform sparsity, it maximizes the entropy of the data in the reconstruction domain while preserving data fidelity in the sample domain [47,114]. MaxEnt has been successfully used to reconstruct under-sampled images in astronomy and multi-dimensional spectra in NMR [31,61,114]. However, MaxEnt has not been applied to the mixed-domain $k_y - t_1$ plane of a 4D MRSI data set *in vivo*.

The use of entropy as a regularizer in image reconstruction predates l_1-*norm*-based CS reconstruction and continues to be used extensively in the reconstruction of under-sampled NMR spectra in spite of the popularity of CS in other fields. It was first suggested by Frieden in the early 1970s [47] after Jaynes proposed the idea of the Principle of Maximum Entropy, which describes the maximum entropy distribution as the maximally non-committal distribution with regard to unavailable data [67,68]. This principle presents the MaxEnt prior as one that assumes nothing about the unavailable data; by assuming nothing about those points, their possible values are all equally likely to occur and the reconstruction is the one that most closely conforms to the uniform distribution, i.e. is flat. Peaks in the reconstruction domain are the result of signals from the sampled data and any artifacts from the missing data points are flattened because they represent states of low entropy that are not the result of k-space or time domain signals.

In this paper, we compare the MaxEnt and l_1-*norm*-based CS reconstructions of NUS 4D EP-COSI data and show that MaxEnt is a viable alternative to CS for reducing scan times 4X in human breast *in vivo*. We quantitatively characterize the MaxEnt and CS reconstructions by comparing results for retrospectively NUS simulated 4D EP-COSI data at varying levels of SNR and NUS rates. We show that retrospectively 4X NUS 4D EP-COSI *in vivo* breast data reconstructed using either MaxEnt or CS has a comparable spatial, spectral resolution to the fully sampled data. Additionally, we show that MaxEnt and CS reconstructions of prospective 4X NUS 4D EP-COSI scans from the same breast study as the retrospective data using the same mask and sequence parameters compare favorably to the retrospective and fully sampled data. Throughout this paper, the NUS data set that has not been reconstructed and has zeros in place of missing samples is referred to as the zero augmented data set to distinguish it from the MaxEnt and CS reconstructions.

5.3 Experimental

5.3.1 4D MaxEnt and CS Reconstruction: Theory

MaxEnt and l_1-*norm*-based CS were used to reconstruct the under-sampled NUS $k_y - t_1$ plane of the 4D EP-COSI data sets. l_1-*norm*-based CS image reconstruction of 4D MRSI data is formulated as a constrained convex optimization problem [23, 36, 50]:

$$\begin{aligned} &\min_m && \|\psi m\|_1 \\ &\text{such that} && \|K\mathcal{F}m - d\|_2^2 \leq C_0 \end{aligned} \tag{5.1}$$

where $m = (y, x, F_2, F_1)$ is the reconstructed spatial, spectral-domain data, F is the 4D Fourier operator, K is the NUS mask that determines which samples were acquired in the $k_y - t_1$ plane, $d = (k_y, k_x, t_2, t_1)$ is the k-space, time-domain sampled data, C_0 is the standard deviation of the noise in d, and Ψ is a known sparse transform. Ψ was chosen to be the identity transform because m was already self-sparse as shown in [50].

MaxEnt image reconstruction of 4D MRSI data solves a similar problem to CS but uses $S_{1/2}$ entropy for instead of the l_1-*norm* [31, 61, 114]:

$$\begin{aligned} &\max_m && S(m)_{1/2} \\ &\text{such that} && \|K\mathcal{F}m - d\|_2^2 \leq C_0 \end{aligned} \tag{5.2}$$

where $S(m)_{1/2}$ is the entropy of the estimated spectrum and the remaining terms are identical to the CS problem. $S_{1/2}$ entropy is a concave function with a global maximum and no local extrema so there is a single solution that satisfies the problem within the feasible set of solutions defined by the data fidelity constraint as shown in Figure 5.1 [16]. As can be seen, $S_{1/2}$ entropy has a global extremum and has slightly more curvature than the l_1-*norm* but has far less curvature than the l_2-*norm*.

The entropy used in the MaxEnt reconstruction was not the often used $-\sum p \cdot log(p)$ entropy introduced by Shannon [109] but the $S_{1/2}$ entropy derived by Daniell and Hore specifically for NMR spectra originating from spin-1/2 nuclei, such as ^{1}H used in

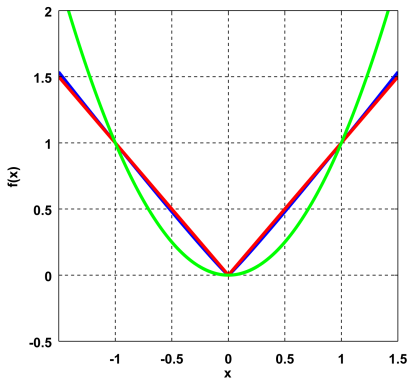

Figure 5.1: Plot showing $-S_{1/2}$ entropy (blue), the l_1-*norm* (red), and the l_2-*norm* (green). Each function has been normalized to equal 1 at $|x| = 1$.

MRSI [31]:

$$S(m)_{1/2} = -\sum_{i=1}^{i=N}\left[r_i \cdot log\left(\frac{r_i + \sqrt{4 + r_i}}{2}\right) - \sqrt{4 + r_i^2}\right] \tag{5.3}$$

where $r_i = {\|m_i\|_1}/{def}$, def is a scaling parameter related to the sensitivity of the scanner and is calculated for m of length N as $\sqrt{(C_0/N)}$ [61]. $S_{1/2}$ is used because the underlying physical processes that produce an MR spectrum are not based on discrete particle events so they cannot be modeled by simple Poisson distributed processes as required for the derivation of Shannon entropy [49]. They are governed by the density matrix of the spin system under investigation so the statistical distribution is different. Equation [3] was derived from first principles using both a classical spin model and a quantum mechanical model. Neither model made any assumptions on the initial state of the spin system nor the pulse sequence used. This equation can be applied to any MR spectrum originating from spin-$^1/_2$ nuclei and addresses previous concerns regarding the use of entropy in MRS and MRI reconstruction [29].

In order to remove any differences between the MaxEnt and CS reconstructions caused by differences in the solvers used, both problems were solved by a Matlab implementation of the Cambridge algorithm [114]. It recasts the image reconstruction problem into an unconstrained convex optimization problem and uses a variant of the conjugate gradient method to iteratively find the extrema in two phases; the first phase minimizes the fidelity constraint, and the second phase minimizes or maximizes the

objective function, while keeping the fidelity constraint minimized. The stopping criterion for the problem is reached when the gradients of the objective, $O(m)$, and fidelity constraint, $C(m)$, are parallel: $\|\nabla O/\|O\|_2 - \nabla C/\|C\|_2\|_1 < .001$. Specific details on the algorithm and modifications to accommodate multidimensional MR data can be found in [61].

The Cambridge algorithm calculates the gradient, $\nabla\|m\|_1 \in C^N$, and Hessian, $\nabla^2\|m\|_1 \in C^{2Nx2N}$, of the objective function which are not defined for $\|m\|_1$ when $m_i = 0$. Therefore, in order to solve the l_1-*norm*-based CS reconstruction problem, $\|m\|_1$ was redefined as:

$$\|m\|_1 = \sum_{i=1}^{i=N} \sqrt{(\mathcal{R}(m_i)^2 + \mathcal{I}(m_i)^2 + \epsilon)} \tag{5.4}$$

where $\mathcal{R}$ and $\mathcal{I}$ were the real and imaginary components of m_i, and ϵ was a small non-zero value to prevent $m_i = 0$. The gradient and Hessian were then defined as:

$$\nabla\|m\|_1 = W^{-1}m \tag{5.5}$$

and

$$\begin{aligned}\nabla^2\|m\|_1 &= |m_i|^{-3}\begin{bmatrix} (|m_i|^2 - \mathcal{R}(m_i)) & -\mathcal{I}(m_i)\mathcal{R}(m_i) \\ -\mathcal{I}(m_i)\mathcal{R}(m_i) & (|m_i|^2 - \mathcal{I}(m_i)) \end{bmatrix} \\ &= 2x2 \text{ block diagonal matrix}\end{aligned} \tag{5.6}$$

where $W \in C^{NxN}$ is a diagonal matrix with $w_{ii} = \|m_i\|_1$ and element, m_i, is associated with the i^{th} $2x2$ block in the Hessian. The gradient and Hessian of $S(m_i)_{1/2}$ are defined in [31, 61]. Only the $2x2$ diagonal blocks of the $\|m\|_1$ and $S_{1/2}$ Hessians were stored in memory during reconstruction, not the full matrices.

5.3.2 Sample Mask Generation

The $k_y - t_1$ plane of the 4D EP-COSI data sets used in these experiments were undersampled using 2D Poisson-gap sample masks that were generated using a modified 1D Poisson-gap process [65]. In 1D Poisson-gap sample masks, the gaps between samples

follow a Poisson distribution, whereas the 2D extension follows the convention that gaps between spaces follow a Poisson distribution. However, both conventions result in the spaces and sample points following Poisson distributions. Poisson distributed masks avoid large gaps between samples, which are detrimental to the reconstruction, while ensuring the samples are randomly distributed [81]. Compared to other distributions, Poisson distributed masks create the fewest aliasing artifacts in the Fourier domain and preserve the SNR of the under-sampled data [110].

The effects of the sample mask on the peak amplitude and line-shape of spectral reconstructions are well documented [81, 85, 106]. Sample mask densities that follow the time-domain NMR signal envelope and sample more points at higher SNR have spectral reconstructions with lower Root Mean Square Errors (RMSE) and less non-linearity compared to sample masks that do not. The t_1 dimension of the EP-COSI data sets in this work were apodized with a sine-squared filter to enhance the cross peaks but because of T_2^* decay, the filtered EP-COSI data had a skewed sine-squared signal envelope; therefore, the 2D Poisson-gap sample mask density was modulated along t_1 with a skewed sine-squared function [130]. The k_y dimension was modulated by an exponential decay function similar to what has been used previously to maximize spatial SNR [84].

The sample density of a Poisson-gap mask can be modulated by the rate parameter, λ, which determines both the mean and variance of a Poisson distribution. The probability of generating a gap, g, from a Poisson distribution is characterized by:

$$p(g, \lambda) = \frac{\lambda^g \cdot e^{-\lambda}}{g!} \tag{5.7}$$

For large λ, large values of g are more likely, and for small λ, small values of g are more likely. Therefore, the probability of g can be modulated by varying the value of λ according to a sine or exponential decay function, and the probability of large gaps between spaces can be increased where the SNR is highest in the MR signal envelope [65]. To generate g as a function of λ, a Poisson process can be simulated using various techniques that do not depend on *a priori* knowledge of g as above [33]. For these

experiments, the $poissrnd(\lambda)$ function in Matlab was used to generate g as a function of λ. It takes as input an array of λ and returns an array of gaps with local mean and variance, λ.

2D Poisson-gap sample masks were iteratively generated in Matlab by combining the 1D distributions of t_1 and k_y until the desired NUS rate was reached.

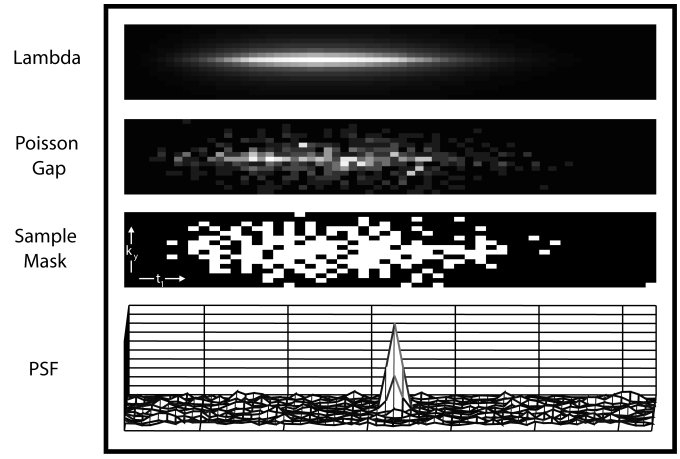

Figure 5.2: Poisson sample mask creation along the $k_y - t_1$ plane for EP-COSI. (Top) Modulated values of λ. (Upper Middle) Poisson distributed values for each λ indicating the gap between spaces in the sample distribution. (Lower Middle) Resulting 2D Poisson-gap sample mask. (Bottom) Magnitude PSF of the 2D sample mask.

An example of the 2D λ, gap, and mask arrays generated by 2D Poisson-gap is shown in Figure 5.2; as the size of λ and the spacing gaps increase, the sample density increases in that area of the mask. The magnitude Point Spread Function (PSF) of the mask is shown and demonstrates the viability of this approach; the single dominant central peak with small side-lobes, surrounded by low amplitude, incoherent artifacts is the desired profile of a random NUS mask PSF [30, 34]. Incoherent sampling artifacts will have low amplitudes and spurious peaks caused by coherent aliasing will be negligible.

5.3.3 MR Simulations

The effects of SNR and under-sampling rate on the reconstructions were quantitatively assessed using a noise-free simulated 4D EP-COSI data set that contained either Choline (Cho) and glycerophosphocholine (GPC) and phosphocholine(PCh) (tCho), Glutamate

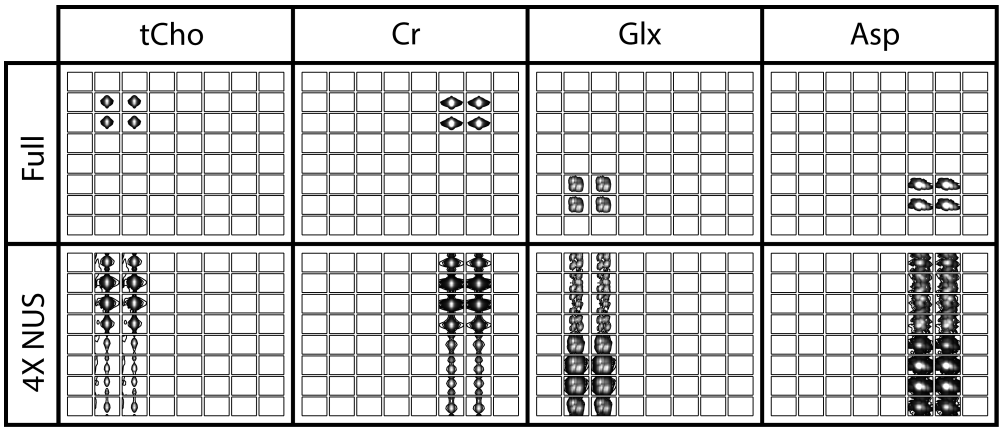

Figure 5.3: Simulated quad phantom illustration. (Top) Spatial distribution of a tCho, Cr, Glx, and Asp diagonal peak when fully sampled. (Bottom) Spatial distribution of the same tCho, Cr, Glx, and Asp diagonal peaks of the 4X NUS zero-augmented data set.

and Glutamine (Glx), Creatine (Cr), Asptartate (Asp), or nothing in each voxel, as represented in the top of Figure 5.3 by a diagonal peak from each metabolite. Each metabolite was simulated using the GAMMA NMR libraries [115] from a 3T Localized 2D Correlated Spectroscopy (L-COSY) sequence [120] with the following parameters: 100 t_1 increments, 1024 points in t_2, TR/TE= $1.5s/30ms$, and spectral bandwidths of $1250Hz$ and $2000Hz$ along F_1 and F_2, respectively. Each 2D spectrum was line-broadened by $10Hz$ and apodized by a sine-squared filter along t_1 and a skewed sine-squared filter with skew parameter 0.5 along t_2. No baseline corrections were performed on the spectra. They were then copied into an 8x8 spatial grid to simulate spatially distributed metabolites as follows: the upper left quadrant contained $2x2$ voxels of tCho, the upper right quadrant contained $2x2$ voxels of Cr, the lower left quadrant contained $2x2$ voxels of Glx, and the lower right quadrant contained $2x2$ voxels of Asp.

As a result of under-sampling the $k_y - t_1$ plane, the spatial, spectral artifacts caused the tCho and Glx voxels to alias into each other and the Cr and Asp voxels to alias into each other, as illustrated by the zero augmented data in the bottom of Figure 5.3. This changed the integrated peak area contained within each metabolite as the spatial, spectral separation between the metabolites broke down.

Noise was added to the simulated noise free 4D EP-COSI data set to model SNRs

of 2 to 20 in increments of 2. It was under-sampled 5X, 2.5X, 1.67X, and 1.25X and then separately reconstructed by MaxEnt and CS. The SNR was varied by simulating different levels of thermal noise in the data set by adding univariate Gaussian noise to the noise-free real and imaginary channels of the 4D EP-COSI data set [95]. The desired SNR was achieved by ensuring the additive noise signal power (σ^2) was equal to 1/SNR of the noise free data set signal power (ω^2), such that:

$$s = d + \frac{\omega^2}{(\sigma^2 * SNR)} * n \tag{5.8}$$

where n is the additive noise, d is the noise free data, and s is the noisy data with the desired SNR. Because the additive noise was random, each SNR was simulated and reconstructed 20 times per sample mask to account for random fluctuations in the reconstruction. The sampling masks were created using the 2D Poisson-gap method described earlier.

5.3.4 MR Spectroscopic Imaging

The breasts of three healthy volunteers were scanned using the 4D EP-COSI sequence on a Siemens 3T Trio scanner with the following parameters: $1x1x1\ cm^3$ voxel size, 50 t_1 increments, TR/TE/averages = $1.5s/30ms/1$, $16x16$ cm^2 FOV, and spectral bandwidths of $1250Hz$ and $1190Hz$ along F_1 and F_2, respectively. Each breast was scanned twice: a 4X prospective NUS scan and a fully sampled scan using the same FOV and shim. The NUS scan took 5 minutes to complete and the fully sampled scan took 20 minutes. Both scans were first apodized using a sine-squared filter along t_1 and a skewed sine-squared filter with skew parameter 0.5 along t_2. No baseline corrections were performed on the *in vivo* breast data. The fully sampled scans were then retrospectively under-sampled 4X using the same mask that was used in the prospective scan shown in Figure 5.9, and then both NUS data sets were reconstructed using MaxEnt and CS.

5.4 Results

5.4.1 MR Simulations

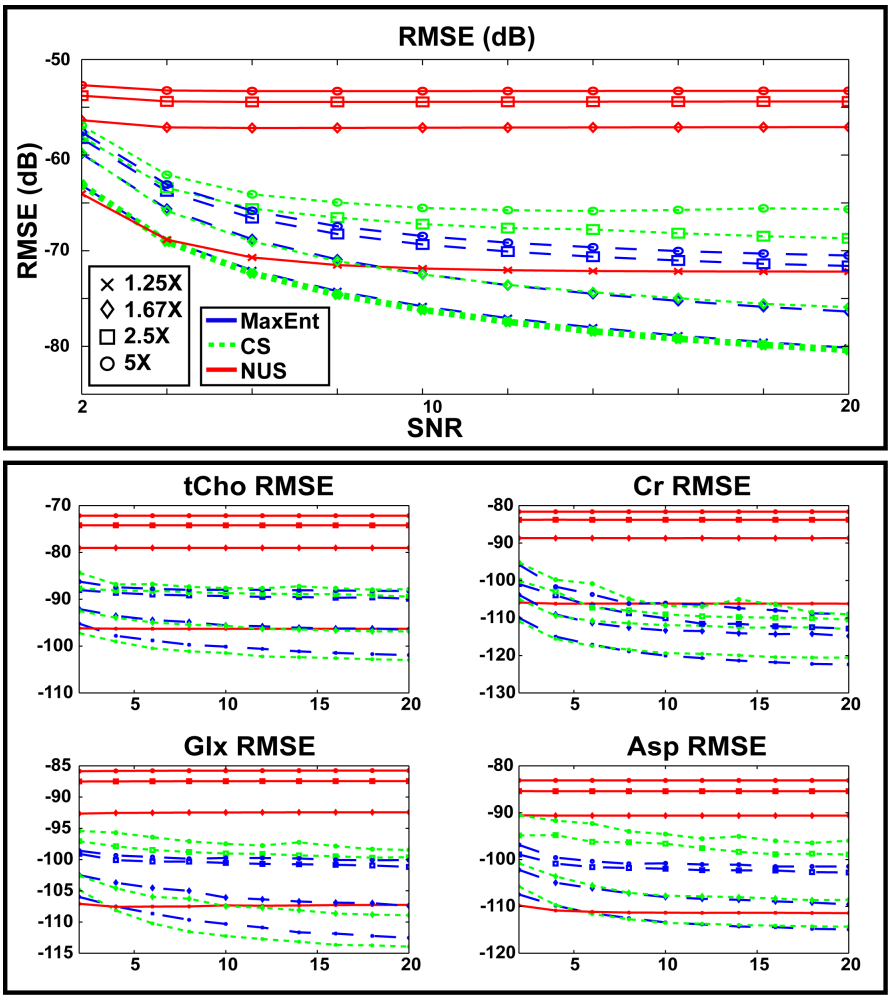

Figure 5.4: Metrics comparing the zero augmented, MaxEnt reconstructed, and CS reconstructed 4D EP-COSI simulated data. (Upper) Overall RMSEs of each data set versus SNR for 5X, 2.5X, 1.67X, and 1.25X NUS. (Lower) tCho, Glx, Cr, and Asp metabolite-specific RMSEs for each data set versus SNR for 5X, 2.5X, 1.67X, and 1.25X NUS.

Quantitative results for the MaxEnt and CS reconstructions of the simulated 4D EP-COSI data set at different NUS rates and SNRs are shown in Figure 5.4. The left upper pane shows the mean RMSE versus SNR for the zero augmented and reconstructed data sets at each NUS rate. The RMSE provides an estimate of reconstruction accuracy with

respect to a fully sampled reference data set that increases as the two data sets become more dissimilar. The RMSE was calculated in the spatial-spectral domain as:

$$RMSE = \frac{1}{N}\sqrt{\sum \left(|data| - |full|\right)^2} \tag{5.9}$$

where N is the number of data points, full is the fully sampled data set, and data is the zero augmented or reconstructed data set. Error bars are not shown because the standard deviations were three to four orders of magnitude smaller than the mean RMSEs and did not vary noticeably over NUS rate or SNR. As can be seen, the RMSE of the zero augmented data set increases as the NUS rate increases but does not vary considerably with SNR except at low NUS rates. Both the CS and MaxEnt reconstructions showed large decreases of the RMSE at each SNR and NUS rate but at low SNRs it begins to rise. At low NUS rates, CS and MaxEnt have comparable RMSEs at each SNR; however, at higher NUS rates the RMSEs for MaxEnt reconstruction are lower than for CS, and this difference increases with SNR.

	tCho	Glx	Cr	Asp
Diagonals (ppm)	(3.2,3.2), (3.5,3.5), (4.0,4.0), (4.3,4.3)	(2.3,2.3), (3.7,3.7)	(3.0,3.0), (3.9,3.9)	(2.8,2.8), (3.9,3.9)
Cross Peaks (ppm)	(3.5,4.0), (3.5,4.3), (4.0,3.5), (4.3,3.5)	(2.3,3.7), (3.7,2.3)	N/A	(2.8,3.9), (3.9,2.8)

Table 5.1: 2D Peak locations (PPM) for selected metabolites.

The lower pane of Figure 5.4 shows the average RMSE of the diagonal and cross peaks of tCho, Glx, Cr, and Asp versus SNR of the zero augmented and reconstructed data sets. The RMSEs were calculated over the metabolite peaks at the ppm locations listed in Table 5.1. Each RMSE was calculated only over the four spatially distributed voxels for each metabolite. For example, the tCho RMSEs were calculated over voxels (2,2), (2,3), (3,2), and (3,3) as illustrated in Figure 5.3. Therefore, these RMSEs reflect local changes to the metabolite peak line-shape and amplitude caused by the spatial, spectral aliasing along the $k_y - t_1$ plane from the NUS and reconstruction.

All of the metabolite RMSEs in the right lower pane of Figure 5.4 show similar trends over SNR as the overall RMSEs in the left upper pane of Figure 5.4 at each under-sampling NUS rate. Both the MaxEnt and CS reconstructions have lower RMSEs than the zero augmented data sets, indicating the metabolite peak line-shapes and amplitudes are being properly reconstructed. The MaxEnt reconstructions have lower RMSEs for many metabolites than the CS reconstructions at higher under-samplingNUS rates, but at lower under-sampling rates their RMSEs are roughly equivalent.

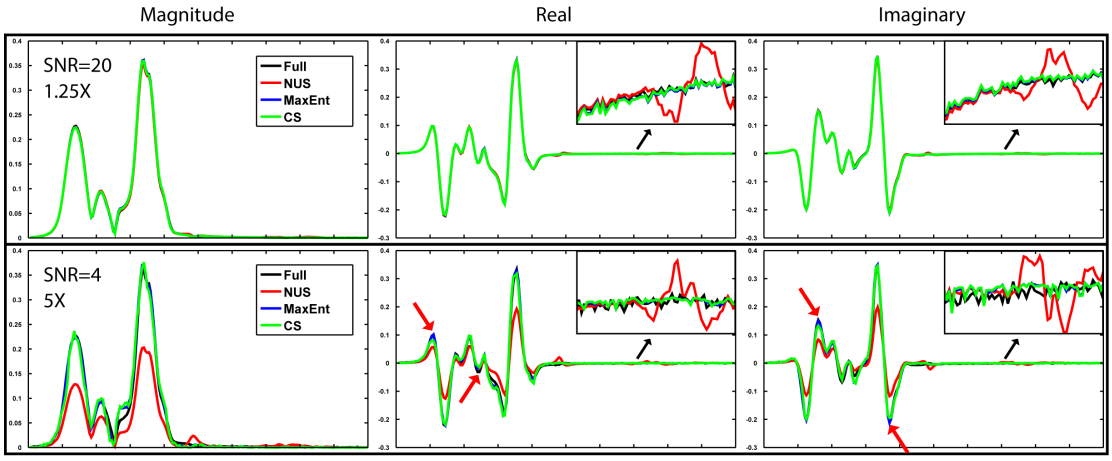

Figure 5.5: 1D magnitude, real, and imaginary cross sections of fully sampled, zero augmented, and reconstructed Glx spectra. (Upper) Cross sections from high SNR spectra 1.25X zero augmented and reconstructed using MaxEnt and CS (Lower) Cross sections from low SNR spectra 5X zero augmented and reconstructed using MaxEnt and CS. (Insets) Magnified cross-sections of spectral baselines.

Figure 5.5 shows a 1D cross-section of the fully sampled, zero augmented, and reconstructed spectra for high and low SNR simulated spectra under-sampled at 1.25X and 5X NUS, respectively. The 1D cross-section is indicated by the dotted-line across F_2 at $F_1 = 3.65$ppm in Figure 5.6 and any NUS artifacts are from aliased peaks above and below the line, not peaks shown in the cross-section. The high SNR, 1.25X NUS zero augmented spectrum shows only small deviations from the fully sampled spectrum, but they are clearly visible in the inset. Both reconstructions restored the baseline to the level of the fully sampled spectrum and preserved the amplitude and line-shapes of the peaks in the full cross sections. The artifacts in the low SNR, 5X NUS zero augmented spectrum show significantly reduced peak amplitudes, broader line-widths,

and Gibbs ringing along the baseline. Both reconstructions successfully restored the line-widths of the peaks in the full cross sections and removed the Gibbs ringing shown in the insets; however, MaxEnt was generally better at restoring the peak amplitude as indicated by the red arrows. Many of the real and imaginary peak amplitudes in the CS reconstructions were lower than the MaxEnt reconstructions, and the baseline for CS was slightly lower as well. However, the CS magnitude peak amplitudes are generally higher than MaxEnt.

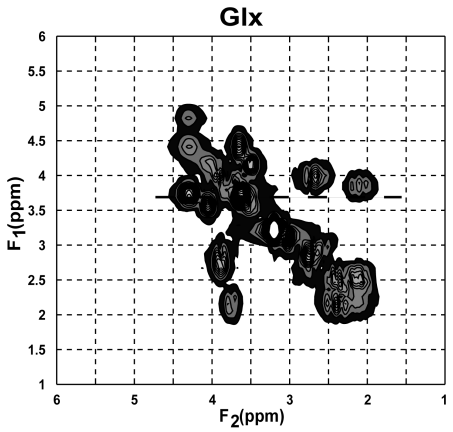

Figure 5.6: Fully sampled 2D COSY Glx spectrum with dotted line dotted-line across F_2 at $F_1 = 3.65$ppm indicating 1D cross section shown in Figure 5.5.

5.4.2 NUS of 4D EP-COSI in Human Breast

The results from a prospective 4X NUS EP-COSI scan of a 31 year-old healthy human breast that has been MaxEnt and CS reconstructed are shown in Figures 5.7A and 5.7B, respectively, with the zero augmented data shown in Figure 5.7C. The contour levels used in the fully sampled results in Figure 5.8A were used in Figure 5.7. The mask used to under-sample the $k_y - t_1$ plane is shown in 5.9 along with the signal envelopes for each dimension and was generated using the 2D Poisson-gap method described earlier in this paper.

Figures 5.7A1 and 5.7B1 show 2D COSY spectra extracted from the MaxEnt and CS reconstructions, respectively. They were taken from the fatty breast regions highlighted in Figures 5.7A2 and 5.7B2. They clearly show the lipid diagonal peaks: olefinic

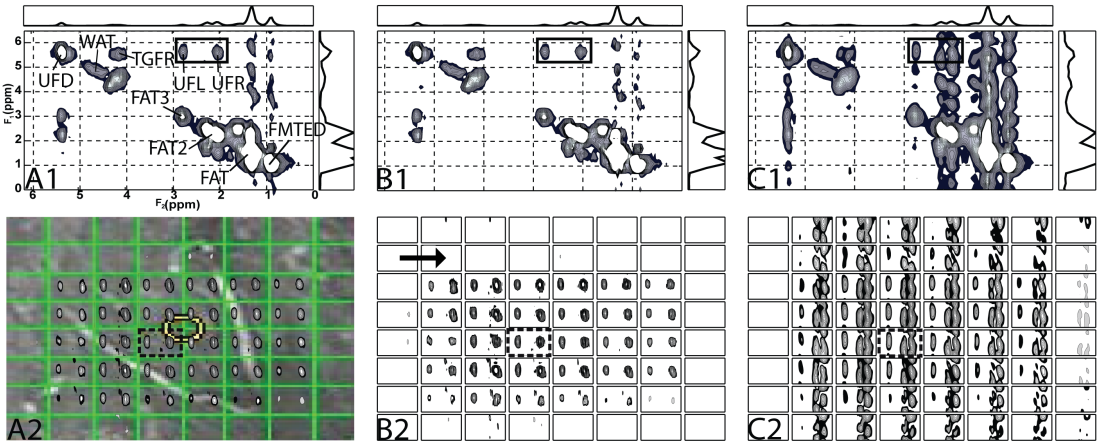

Figure 5.7: Prospective 4D EP-COSI results (Top) Selected 2D COSY spectrum from a 4D EP-COSI scan of healthy, fatty breast highlighted in the bottom images for A1) MaxEnt reconstructed B1) CS Reconstructed C1) 4X NUS zero augmented data. (Bottom) Spatial distribution of the UFL/UFR cross-peaks highlighted in the 2D COSY spectrum for A2) MaxEnt reconstructed B2) CS Reconstructed C2) 4X NUS zero augmented data.

fat (UFD), methyl fat (FMETD), and fat (FAT/FAT2/FAT3) and the cross peaks: unsaturated fatty acid right (UFR), unsaturated fatty acid left (UFL), and triglyceryl fat (TGFR) [77]. The spatial distribution of the UFL/UFR cross-peaks from the reconstructions are shown in Figures 5.7A2 and 5.7B2 with the MaxEnt reconstructions spatial distribution overlaid on the anatomical MRI.

Figure 5.7C1 shows the same 2D COSY spectrum as Figures 5.7A1 and 5.7B1 with 4X NUS applied to the $k_y - t_1$ plane using the mask in Figure 5.9, however, no MaxEnt or CS reconstruction was used. The spatial-spectral incoherent artifacts from the NUS manifest as smeared peaks along F_1, which is illustrated by the collapse of the peaks in the 1D projection of the F_1 dimension on the right. The aliasing of the large diagonal fat peaks around ($F_2 = 2$ppm, $F_1 = 2$ppm) obscure the much smaller UFL/UFR cross-peaks around ($F_2 = 2.1$ppm, $F_1 = 5.4$ppm). Figure 5.7C2 shows the spatial distribution of the UFL/UFR cross-peaks and how spatial artifacts from under-sampling $k_y - t_1$ manifest as errant peaks in adjacent voxels.

Comparing the MaxEnt and CS reconstructed spectra in Figures 5.7A1 and 5.7B1, all of the significant diagonals and cross-peaks are fully resolved in both datasets with

qualitatively similar line-widths and amplitudes. The only major difference between them is the amplitudes of the t_1 ridges centered at ($F_2 = 1.3$ppm, $F_1 = 1.3$ppm) and ($F_2 = 1.0$ppm, $F_1 = 1.0$ppm) for CS are lower than for MaxEnt.

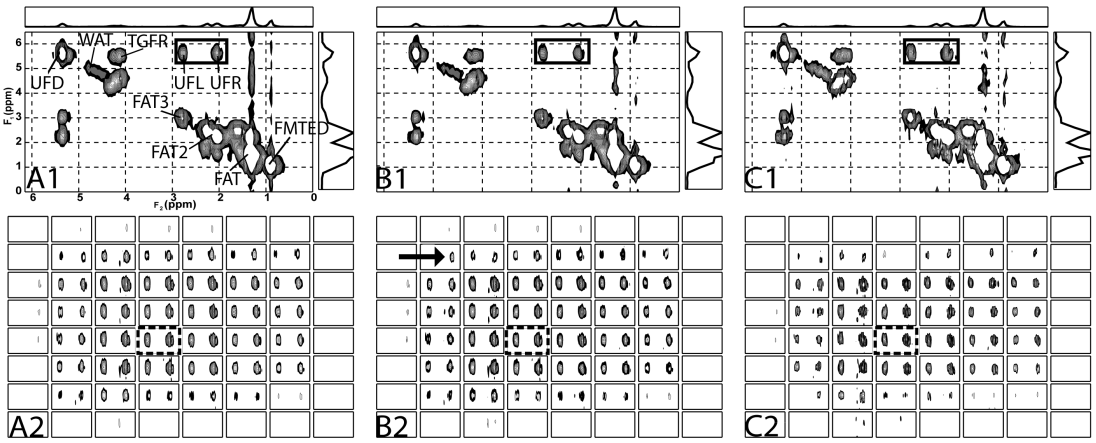

Figure 5.8: Retrospective 4D EP-COSI results (Top) Selected 2D COSY spectrum from a 4D EP-COSI scan of healthy, fatty breast highlighted in the bottom images for A1) fully sampled B1) MaxEnt reconstructed C1) CS Reconstructed data. (Bottom) Spatial distribution of the UFL/UFR cross-peaks highlighted in the 2D COSY spectrum for A2) fully sampled B2) MaxEnt reconstructed C2) CS Reconstructed data.

The results from a fully sampled EP-COSI scan of the same healthy breast shown in Figure 5.7 that has been retrospectively 4X under-sampled using the same mask and MaxEnt and CS reconstructed are shown in Figure 5.8. Figure 5.8A shows the fully sampled data and Figures 5.8B and 5.8C show the MaxEnt and CS reconstructions, respectively. Since the same FOV was used for both scans, the spectra on the top of Figure 5.8 show the same 2D COSY spectra as the top of Figure 5.7, and the bottom shows the spatial distribution of the UFL/UFR cross-peaks. The same contour levels used for the fully sampled data in Figures 5.8A were also used for the MaxEnt and CS reconstructed results in Figures 5.8B and 5.8C.

As can be seen, all of the peaks in the fully sampled spectrum in Figure 5.8A1 are completely resolved in both the prospective and retrospective reconstructions shown in Figures 5.7B1, 5.7C1, 5.8B1, and 5.8C1; their positions, line-widths, amplitudes, and spectral resolutions are all qualitatively comparable. However, the spatial distributions of the fully sampled and the retrospective NUS results have better agreement than

the prospective NUS results in the upper region of the breast; the excited volume of the prospective NUS results is one row smaller than the retrospective NUS results as indicated by the red arrows in Figures 5.7 and 5.8. This change was also observed in the non-water suppressed scans taken prior to the prospective NUS and fully sampled scans, so it is not an artifact of the reconstruction.

Table 5.2 shows the F_1 Full Width at Half Maximum (FWHM) and peak amplitudes of the zero augmented and reconstructed data set magnitude peaks in Figures 5.7 and 5.8. For comparison, they are normalized by the fully sampled peak amplitudes and FWHM from Figure 5.8, so values greater than one are larger than the fully sampled value. As can be seen, there are quantitative differences between the CS and MaxEnt reconstructed peak line-shapes. The zero augmented data set has broader, shorter peaks, as expected and both the CS and MaxEnt reconstructed peak line-shapes are closer to the fully-sampled data; however, the MaxEnt peak line-shapes are almost all closer to the fully-sampled data than the CS peak line-shapes, which are narrower and taller than both the MaxEnt and fully sampled data. The increase in peak amplitudes in the CS reconstruction is greater in the larger peaks (FAT1, FAT2, and FAT3) than the smaller peaks (UFD, UFL, UFR) when compared to MaxEnt.

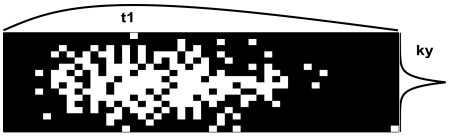

Figure 5.9: NUS mask used to prospectively NUS the $k_y - t_1$ plane 4X in Figures 5.7 and 5.8.

Additional quantitative differences between the MaxEnt and CS reconstructions are shown in Table 5.3; the range of values for the (UFL+UFR)/(FAT3+FAT2) integrated peak area ratios and average errors from the fully sampled ratios for the central 6x6 voxels of three healthy human breasts. As can be seen, NUS caused the ratios to vary considerably from the fully sampled ratios with a high mean ratio error. The reconstructed ratios show much better agreement with the fully sampled ratios and have a much smaller mean ratio error in all three scans than the zero augmented. However, the mean ratio errors for the MaxEnt reconstruction are almost all smaller than their CS counterparts, indicating the peak ratio was more accurately reconstructed by MaxEnt.

Prospective Amplitude								
	FAT1	FAT2	FAT3	FMTED	TGFR	UFD	UFL	UFR
MaxEnt	1.249	1.342	1.232	1.614	0.951	1.125	1.060	1.078
CS	1.427	1.372	1.263	1.655	0.982	1.142	1.150	1.161
Prospective FWHM								
MaxEnt	0.818	0.909	0.818	1.000	0.818	1.000	0.900	0.727
CS	0.727	0.909	0.818	0.900	0.909	1.000	0.900	0.727
Retrospective Amplitude								
Zero Augmented	0.634	0.70	0.662	0.639	0.639	0.627	0.518	0.845
MaxEnt	1.061	1.026	1.090	1.010	1.019	1.029	0.942	0.989
CS	1.237	1.138	1.017	0.961	1.077	0.995	1.071	1.043
Retrospective FWHM								
Zero Augmented	1.273	1.273	1.182	1.30	1.00	1.30	1.40	1.010
MaxEnt	0.818	0.909	0.818	1.00	0.818	1.00	1.00	0.818
CS	0.727	0.818	1.010	1.00	0.727	1.10	0.80	0.727

Table 5.2: Relative FWHM along F_1 and amplitude of metabolite peaks for zero augmented, MaxEnt reconstruction, and CS reconstruction of the voxel shown in Figures 5.7 and 5.8. Values are normalized by the fully sampled peak FWHM and amplitudes.

The retrospective reconstruction results are only slightly better than the prospective results, which is not surprising given the excitation volume differences seen in Figures 5.7 and 5.8.

5.5 Discussion

The simulated 4D EP-COSI data set results in Figure 5.4 demonstrate how the MaxEnt and CS reconstructions perform at different SNRs and NUS rates. Both reconstructions decrease the RMSE significantly at each SNR and NUS rate compared to the zero augmented data set but begin to increase at very low SNR, which indicates their inability to fully reconstruct the data when features and sampling artifacts are obscured by high levels of noise. The data fidelity constraint in equations 5.1 and 5.2 determines how closely the reconstructed points must be to the sampled points to within the standard deviation of noise, which increases as the noise floor increases. This increase in the noise floor effectively loosens the fidelity constraint, which allows the reconstructed points to deviate from their sampled counterparts and increases the entropy or sparsity of the reconstructed spectrum by narrowing peak line-widths and de-noising smaller features. This in turn increases the non-linearity and RMSE of the reconstruction because of the

	Breast 1		**Breast 2**		**Breast 3**	
	Ratio Range	Mean Ratio Error	Ratio Range	Mean Ratio Error	Ratio Range	Mean Ratio Error
Fully Sampled	0.1277-0.0456	N/A	0.1984-0.0656	N/A	0.3542-0.0277	N/A
Zero Augmented	0.2162-0.1496	0.0823±0.0198	0.4699-0.3082	0.2640±0.0734	1.008-0.1785	0.2047±0.0916
Retrospective MaxEnt	0.1061-0.0281	0.0244±0.0071	0.1576-.0413	0.0254±0.0142	0.4134-0.0291	0.0215±0.0149
Prospective MaxEnt	0.1049-0.0216	0.0326±0.0083	0.1215-0.0420	0.0415±0.0164	0.3422-0.0414	0.0404±0.0463
Retrospective CS	0.1103-0.0275	0.0246±0.0073	0.1781-0.1004	0.0357±0.0235	0.4114-0.0269	0.0268±0.0175
Prospective CS	0.1084-0.0211	0.0334±0.0082	0.1276-0.0425	0.0397±0.0140	0.3594-0.0374	0.0434±0.0487

Table 5.3: Range and mean error of (UFL+UFR)/(FAT3+FAT2) integrated peak area ratios for fully sampled, zero augmented, MaxEnt reconstruction, and CS reconstruction of three healthy breasts.

loose fidelity constraint [60]. The data fidelity constraint can be tightened beyond the standard deviation of the noise in an effort to reduce the RMSE and reconstruction non-linearity but this prevents the Cambridge algorithm from completely removing the spatial, spectral NUS artifacts close to the noise floor, which could potentially obscure small features [61].

The metabolite RMSEs in Figure 5.4 show the reconstructions offer significant improvements in the amplitude and line-shape of individual peaks over the zero augmented data, even without using methods to reduce the reconstruction non-linearity [106]. CS and MaxEnt produce very similar results at low NUS rates, but MaxEnt generally has a lower RMSE at higher NUS rates than this implementation of CS. As Figures 5.5 and 5.6 demonstrate, both reconstruction methods successfully restored peaks and removed Gibbs ringing artifacts, however, CS had a tendency to over-smooth smaller features close to the noise floor and narrow peak line-widths. It was this over smoothing that reduced the amplitude of the CS reconstructed fat tails at ($F_2 = 1.3$ppm, $F_1 = 1.3$ppm) and ($F_2 = 1.0$ppm, $F_1 = 1.0$ppm) in Figure 5.7. The differences in peak line-widths between MaxEnt and CS contributed to the disparity in RMSE values at higher NUS rates, but the main contributing factor was the change in noise floor in the non-peak regions of the spectra. The noise floor was slightly reduced over the entire 4D data set in the CS reconstructions, which was the vast majority of points in the volume; therefore, small changes in the noise floor had large effects on RMSE. The over-smoothing in the CS reconstructions may have been caused by choosing $\epsilon = def/1000$ in equation 5.4 and will be investigated in the future, even though previous work has used similar values with success [79].

The healthy human breast results in figures 5.7 and 5.8 show that CS and MaxEnt reconstruction work well for prospective and retrospective NUS, filtered *in vivo* EP-COSI scans. There were minor differences between the prospective and retrospective reconstructions; however these can be attributed to intra-scan variations in the excitation volumes since these differences were reflected in the MaxEnt and CS reconstructions, as well as the non-water suppressed scans. The greater SNR-loss caused by T_2^* decay that was not present in the simulated 4D EP-COSI data set did not reduce

the efficacy of the reconstructions. There was still sufficient SNR in the time domain to reconstruct the *in vivo* diagonal and cross peaks in the spectral domain.

While the MaxEnt and CS reconstructions of healthy human breast were qualitatively similar, Tables 5.2 and 5.3 illustrated quantitative differences between them. Both reconstruction methods improved the ratios of lipid peaks in Table 5.3 and the amplitudes and FWHM of major peaks in Table 5.2, which shows they were able to reconstruct the large, aliased diagonals as well as the smaller cross-peaks that were obscured by the diagonals aliasing over the $k_y - t_1$ plane. However, as shown in Table 5.2, the CS reconstructed peaks were narrower with higher amplitudes than their MaxEnt counterparts. This discrepancy increased with peak amplitude, indicating a higher degree of non-linearity in the CS reconstruction over MaxEnt. Using the relative peak amplitudes and FWHM values from Table 5.2 to calculate the peak area instead of the integrated peak area that was used for Table 5.3, the relative (UFL+UFR)/(FAT3+FAT2) ratios for MaxEnt and CS for the retrospective reconstructions are 0.960 and 0.825, respectively. Because the FAT3 and FAT2 peaks from the CS reconstruction are relatively larger than the MaxEnt peaks from the increased non-linearity, their relative ratio with the UFL and UFR peaks is smaller. This increased non-linearity was a contributing factor in the larger mean ratio errors in Table 5.3 for the CS reconstructions compared to the MaxEnt reconstructions.

The under-sampled data in Figures 5.7C1 and 5.7C2 show artifacts spread along F_1 and Y as well as reduced spectral resolution along F_1 and larger FWHMs in Table 5.2 caused by convolution with the broad NUS PSF. The homogeneous nature of fatty breast spectra coupled with the inherently low spatial resolution of 4D EP-COSI made it difficult to determine from the figures if the spatial resolution along Y decreased as a result of the NUS PSF. However, it is clear the effects of the NUS PSF along F_1 were removed by MaxEnt and CS by the narrower FWHM values in Table 5.2 and the lack of NUS artifacts in Figures 5.7A1, 5.7B1, 5.8A1, and 5.8B1. The errant spectral peaks in the spatial distribution were removed in Figures 5.7A2, 5.7B2, 5.8A2, and 5.8B2, suggesting the spatial PSF along Y was improved as well. Any spectral bleed from the spatial PSF of the EP-COSI pulse sequence along X was orthogonal to the effect of the

NUS PSF along Y and was not affected by the MaxEnt and CS reconstructions.

The results in Figures 5.4-5.8 indicate that MaxEnt and CS produced qualitatively similar reconstructions; however, the MaxEnt results were quantitatively better by a small margin as discussed above. This is not surprising, given the objective functions of CS and MaxEnt are similar, but there are minor differences between them as shown in Figure 5.1. CS uses the l_1-*norm* of the reconstructed spectrum in some transform domain, and MaxEnt uses entropy, which is a log-sum function that can be rewritten as a reweighted l_1-*norm*, $\sum w_i \|m_i\|_1$ where w_i is $log(f(m_i))$, the *log* of a function of the reconstructed spectrum. Previous work has shown reweighted l_1-*norm* objective functions can outperform l_1-*norm*-based CS reconstruction [24] and direct comparisons between MaxEnt and l_1-*norm*-based CS reconstruction showed them to be qualitatively equivalent [116]. This is the first known work to show quantitative comparisons between these techniques, however, and further research into their relative performance is ongoing.

The Cambridge algorithm used to solve the MaxEnt and CS reconstruction problems proved to be robust against different levels of SNR and NUS rates for the simulated and *in vivo* data sets. There are other l_1-*norm* solvers available for the CS reconstruction problem; however, many of them require parameter tuning for different data sets in order to find the optimal reconstruction parameters [28, 72]. The Cambridge algorithm does not have any tuning parameters that must be adjusted to find the optimal reconstruction for a data set, which offers a substantial workflow improvement over other solvers. While the Cambridge algorithm can be modified to solve the CS l_1-*norm* reconstruction problem, it takes on average 5-10 times as long to converge as the MaxEnt problem, which took 7-10 minutes on average using a 64-bit dual core, 3.4 GHz Core i7 processor with 16GB RAM. Therefore, we do not recommend its usage as an l_1-*norm* solver; it was only used for the current work in order to compare results for MaxEnt and CS reconstruction that were not biased by different solver implementations. However, using the Cambridge algorithm as a MaxEnt solver provides results that are equal to or better than CS and is relatively fast, robust to SNR changes, and does not require parameter tuning.

The Poisson-gap sampling masks used in these experiments were generated by a random Poisson distribution, which injects a degree of uncertainty into the reconstruction. It has proven to be a reliable technique that generates masks with desirable PSFs, as shown in Figure 5.2, and the RMSEs of reconstructed data sets using different Poisson-gap sample masks are stable [65]. Previous attempts by our group to use deterministic masks that were not randomly generated were difficult to optimize and suffered from coherent aliasing which cannot be removed by MaxEnt or CS reconstruction [3,106]. Recent work in under-sampled NUS multidimensional NMR data sets using deterministic sample masks has shown promise and could be adapted to 4D MRSI [28, 40].

Because of the random nature of the Poisson-gap sampling masks, they were chosen by an empirical heuristic that minimized the width of the central peak, the total power of the incoherent artifacts, and the ratio of the largest artifact peak to the central peak in the mask PSF. They followed a skewed-sine bell modulation function to maximize the reconstruction SNR, but were not optimized for specific metabolites or post-processing spectral filters. In our experiments, we have observed that mismatches between a sample modulation function and the filtered signal envelope of a metabolite results in a failure to sufficiently sample the high SNR points along t_1 and prevents the full metabolite peak area from being reconstructed [85, 106, 107]. Therefore, it should be emphasized that the sample mask is crucial to the SNR of each reconstructed metabolite for 4D EP-COSI data and there is a dependence on the shape of standard spectral filters applied prior to reconstruction [130].

Further research into reducing the non-linearity of the reconstructed peaks so accurate quantitation is possible and comparisons to additional CS methods are on-going. Additionally, determining whether Poisson-gap or deterministic sample masks should be used and optimizing the modulation functions for specific metabolites and different spectral filters will be addressed in future papers.

5.6 Conclusions

This work has demonstrated MaxEnt is a viable alternative to l_1-*norm* based CS reconstruction for accelerating the acquisition of 4D EP-COSI data *in vivo*. MaxEnt provided reconstructions equal to or better than CS and the robust nature of the Cambridge algorithm without the need for parameter tuning make it a good candidate for clinical use. The CS and MaxEnt reconstructions throughout this work were qualitatively similar; however, the quantitative results indicated increased non-linearity in the CS reconstruction when compared to MaxEnt. Simulated 4D EP-COSI data provided a quantitative characterization of both reconstruction methods at different NUS rates and SNRs, while the 4X NUS *in vivo* EP-COSI breast data showed that a clinically viable 5-minute breast scan is possible.

5.7 Acknowledgments

Authors acknowledge the scientific support of Dr. Rajakumar Nagarajan for recording the *in vivo* NUS EP-COSI data. This work was supported by: 1) a National Institute of Health (NIH) training grant #5T15 LM07356 (BLB), 2) an IDEA Expansion grant from the US Army Department of Defense (DOD) Breast Cancer Research Program (BCRP)#W81XWH-10-1-0743 (MAT)

CHAPTER 6

Group Sparse Reconstruction

This chapter is the proof of a manuscript that was written as part of this dissertation research and will be submitted for publication. It is reproduced in full with only the formatting changed to match the dissertation style. A shorter, conference version of this manuscript has been published in the proceedings of the IEEE International Symposium on Biomedical Imaging (ISBI) Conference 2014.

B. Burns, N. Wilson, and M. Thomas, "Split-Bregman-Based Group-Sparse Reconstruction of Multidimensional Spectroscopic Imaging Data" *IEEE ISBI*, 2014; Beijing, China.

6.1 Abstract

Four-dimensional (4D) Magnetic Resonance Spectroscopic Imaging (MRSI) data combining 2 spatial and 2 spectral dimensions provide valuable biochemical information *in vivo*, however, its 20-40 minute acquisition time is too long to be used for a clinical protocol. Data acquisition can be accelerated by non-uniformly, under-sampling (NUS) the $k_y - t_1$ plane but this causes artifacts in the spatial-spectral domain that must be removed by non-linear, iterative reconstruction. Previous work has demonstrated the feasibility of accelerating 4D MRSI data acquisition through NUS and iterative reconstruction using Compressed Sensing(CS), Total Variation (TV) denoising, and Maximum Entropy (MaxEnt) reconstruction. Group Sparse (GS) reconstruction is a variant of CS that exploits the structural sparsity of transform coefficients to achieve higher acceleration factors than traditional CS. In this article, we derive a solution to

the GS reconstruction problem within the Split-Bregman iterative framework that uses arbitrary transform grouping patterns of overlapping or non-overlapping groups. 4D Echo-Planar Correlated Spectroscopic Imaging (EP-COSI) gray matter brain phantom and *in vivo* brain data are retrospectively under-sampled 2X, 4X, 6X, 8X, and 10X and reconstructed using CS, TV, MaxEnt, and GS with overlapping or non-overlapping groups. Results show that GS reconstruction with overlapping groups outperformed the other reconstruction methods at each NUS rate for both phantom and *in vivo* data. These results can potentially reduce the scan time of a 4D EP-COSI brain scan from 40 minutes to under 5 minutes *in vivo*.

6.2 Introduction

Magnetic Resonance Imaging (MRI) exploits the resonant frequency of ^{1}H protons within water *in vivo* to generate anatomical images of the human body. Magnetic Resonance Spectroscopic Imaging (MRSI) is a similar imaging technique to MRI, however in lieu of the resonant frequency of ^{1}H protons in water, the resonant frequencies of ^{1}H protons in metabolites including but not limited to: creatine (Cr), choline (Cho), glutamate (Glu), glutamine (Gln), lactate (Lac), aspartate (Asp), and N-acetyl-aspartate (NAA) are used to generate a metabolic image instead [104,120]. Each of these metabolites has a unique resonance spectrum *in vivo* caused by their chemical environment and covalent bonding structure that can be used to identify and quantify their concentrations within each voxel [108]. Using this concentration information, the biochemical compositions of healthy and diseased tissues can be determined without the need for invasive biopsies and the altered metabolism of cancers can be detected [89].

The four-dimensional (4D) Echo-Planar Correlated Spectroscopic Imaging (EP-COSI) is an MRSI pulse sequence allows for the simultaneous acquisition of two spatial and two spectral dimensions, (k_y,k_x,t_2,t_1), in one scan *in vivo* [78]. This 4D sequence provides a 2D spectrum for each voxel in a slice, which differs from other MRSI sequences that only provide a single spectral dimension per spatial voxel [87, 98]. The overlap of resonance peaks within a single spectral dimension is a major impediment

to identifying individual metabolites and the increased spectral dispersion offered by a second spectral dimension can disentangle complex over-lapping spectral peaks [2]. Two spectral dimensions have been shown to increase the specificity and sensitivity of tumor grade classification when used with dynamic contrast enhanced (DCE)-MRI in the breast [119]. However, 4D EPCOSI acquisitions are slow compared to most MRI sequences and can require up to 40 minutes for a typical scan, which is too long to be used on a routine clinical basis.

4D EP-COSI data acquisition is a rasterized scan that acquires a 2D spatio-temporal plane, $k_x - t_2$, from the 4D volume during each TR. The second spatial (k_y) and spectral (t_1) dimensions are incrementally acquired between rasters until the entire 4D volume is sampled. k_y is acquired using standard phase encoding techniques from MRI and t_1 is acquired as a series of phase shifted 1D spectra [78]. 4D EP-COSI data acquisition can be accelerated *in vivo* by non-uniformly under-sampling (NUS) the incrementally acquired dimensions, k_y and t_1. However, NUS produces artifacts in the spatio-spectral mixed domain that can be removed by reconstructing the missing samples in the $k_y - t_1$ plane through non-linear, iterative reconstruction [23, 36].

Previous work has accelerated MRI acquisition by under-sampling k_y in k-space and reconstructing the missing samples with Compressed Sensing (CS) reconstruction [14,79]. CS has been applied to under-sampled, spatio-temporal and spatio-spectral mixed domains in dynamic MRI [51] and 3D spatial, 1D spectral MRSI [62]. The feasibility of under-sampling the mixed-domain $k_y - t_1$ plane of a 4D MRSI data set and reconstructing the missing samples with Total Variation (TV) denoising or Maximum Entropy (MaxEnt) reconstruction has been shown previously [19, 50]. NUS rates as low as 5X were demonstrated *in vivo* and showed that it is possible to accelerate the acquisition of 4D MRSI data down to a clinically acceptable 5-10 minute scan time.

The current work derives a solution to the Group Sparse (GS) reconstruction problem for 4D MRSI data within the Split-Bregman iterative framework and compares the results to CS, TV, and MaxEnt reconstructions of 4D EP-COSI phantom and *in vivo* brain data under-sampled at 2X, 4X, 6X, 8X, and 10X [55, 129]. The Split-Bregman algorithm has been modified to allow for arbitrary coefficient grouping patterns of over-

lapping or non-overlapping groups with no a priori assumptions on the grouping patterns used. The Split-Bregman algorithm has been previously used for TV-based reconstruction of NUS MRSI data [50] and for multi-channel reconstruction of NUS MRI data where the multiple measurement vector (MMV) problem was solved by extending the algorithm to accommodate row-wise grouping of jointly sparse samples [131]. GS reconstruction has previously been applied to the under-sampled $k_y - t$ planes of 2D cine and perfusion cardiac MRI and provided superior results to CS [99, 123].

In this article, an over view of the Split Bregman algorithm and GS reconstruction problem are provided in sections 6.3.2 and 6.3.3, respectively. The derivation of the solution to the GS reconstruction problem within the Split Bregman framework is provided in section 6.3.4. A brief overview of the CS, TV, and MaxEnt reconstruction problems is provided in section 6.3.1 with a description of the non-linear algorithms and parameter settings used to solve them in section 6.4.2. The experimental setup for the 4D EP-COSI gray matter brain phantom and *in vivo* brain scans is provided in section 6.4.1. Results from retrospectively under-sampled phantom and *in vivo* data sets then reconstructing the NUS $k_y - t_1$ plane with CS, TV, MaxEnt, and GS with overlapping and non-overlapping groups, are shown in sections 6.5.1 and 6.5.2. These experiments show that GS reconstruction with overlapping coefficient groups provides reconstructions with lower metabolite Root Mean Square Errors (RMSE) than the other methods used, as well as qualitatively superior spectra down to 8X NUS in both phantom and *in vivo* data sets. This acceleration translates to a clinically acceptable 5 minute 4D EP-COSI brain scan that previously took 40 minutes to complete.

6.3 Theory

6.3.1 CS, TV, and MaxEnt Based MRSI Reconstruction

The under-sampling of 4D MRSI data sets and subsequent non-linear reconstruction by CS, TV, or MaxEnt has been described by previous work and will only be covered here briefly [19, 50]. Each of these methods can be used to iteratively reconstruct missing

samples from an NUS MRSI data set by enforcing a fidelity constraint in the sample domain and either a maximum sparsity, minimum differences, or maximum entropy signal model in some transform domain [36, 103, 114]:

$$\begin{aligned} &\min_u && \phi(u) \\ &\text{such that} && \|R\mathcal{F}u - f\|_2 \leq \sigma \end{aligned} \tag{6.1}$$

where $u \in \mathbb{C}^N$ is the reconstructed spatial, spectral-domain (Y, X, F_2, F_1) data, $\mathcal{F}$ is the 4D Fourier operator, $R \in \mathbb{R}^{MxN}$ is the under-sampling mask that determines which samples were acquired in the $k_y - t_1$ plane, $f \in \mathbb{C}^M$ is the sampled k-space, time-domain (k_y, k_x, t_2, t_1) data, and σ is the standard deviation of noise in f.

The choice of $\phi(u)$ depends on the signal model used during reconstruction. The transform sparsity signal model used in CS uses $\phi(u) = \|\Psi u\|_1$, which is the l_1 norm of the reconstructed data in some transform domain, Ψ, and attempts to remove NUS artifacts by reducing the amplitude of each transform coefficient and increasing the sparsity of Ψu [37]. The minimum TV signal model uses $\phi(u) = \|\nabla_y \cdot \Psi u + \nabla_{F_1} \cdot \Psi u\|_1$, where ∇_y and ∇_{F_1} are anisotropic differential operators applied to Ψu along the y and F_1 dimensions, respectively, and removes NUS artifacts by minimizing the differences between adjacent transform coefficients. Because the mixed-domain $k_y - t_1$ plane of a 4D EP-COSI data set is self-sparse, no sparsifying transforms are applied to u for the CS and TV reconstruction so $\Psi = I$ [50]. The MaxEnt signal model uses $\phi(u) = -S_{1/2}$, which is the spin-1/2 entropy derived from the statistical distributions defined by the density matrices of spin-1/2 nuclei, such as ^{1}H [31]. It removes NUS artifacts by modeling each transform coefficient in the spatial-spectral domain as the byproduct of an ensemble of ^{1}H spins whose phase dispersion determines the signal amplitude; in-phase spin ensembles have high signal amplitude and low phase entropy, while high entropy ensembles have low phase coherence and no signal. Because Shannon entropy is derived for discrete processes that result from a Poisson-based distribution, it can not be used for reconstructing NMR data, which do not follow a Poisson distribution. Therefore, spin-1/2 entropy must be used, which is derived from ^{1}H-spin density matrices [31, 48].

6.3.2 Split Bregman Algorithm

The Split-Bregman algorithm is from the class of Alternating Direction Method of Multipliers (ADMM) that split a constrained problem into a sequence of simpler unconstrained sub-problems [10, 55]. It differs from continuation-based methods by keeping the values of any Lagrange multipliers fixed between iterations and modifies the data instead. This has the benefits of increased numerical stability and a lower dependence on the initial choice of Lagrange multiplier values. If we wish to use the Split Bregman algorithm to solve a problem of the form:

$$\begin{aligned} &\min_{u,z} && E(u,z) \\ &\text{such that} && H(u,z) \end{aligned} \tag{6.2}$$

where $E(u,z)$ is a convex, non-differentiable function and $H(u,z)$ can be assumed to be of the form $Au = z$, we first convert it to an unconstrained problem:

$$\min_{u,z} E(u,z) + \lambda H(u,z) \tag{6.3}$$

where conventional continuation-based methods would increase $\lambda \to \infty$ as $H(u,z) \to 0$ to find a solution; however, we apply the Bregman distance relaxation to equation 6.3 and split it into sub-problems instead. The Bregman distance for the function $E(u)$ at the point u^k is:

$$D_E^p(u,u^k) = E(u) - E(u^k) - \langle p_u^k, u - u^k \rangle \tag{6.4}$$

where the Bregman parameter p_u^k is the sub-gradient of $E(u)$ at u^k. The Bregman distance and iteration scheme are then applied to equation 6.3 by defining the u, z, and Bregman parameter updates at each iteration over k:

$$\begin{aligned} (u^{k+1}, z^{k+1}) &= \min_{u,z} D_E^p(u, u^u, z, z^k) + \lambda H(u,z) \\ p_u^{k+1} &= p_u^k - \lambda \nabla_u H(u^{k+1}, z^{k+1}) \\ p_z^{k+1} &= p_z^k - \lambda \nabla_z H(u^{k+1}, z^{k+1}) \end{aligned} \tag{6.5}$$

λ is never increased and under fairly weak assumptions on $E(u,z)$ and $H(u,z)$, $\nabla_u H$ and $\nabla_z H \to 0$ as $k \to \infty$ so that $p^{k+1} \to p^k$ and the Bregman parameters converge [55]. However, because $H(u,z)$ is of the form $Au = z$, equation 6.5 can be simplified to the equivalent problem [92]:

$$\begin{aligned} (u^{k+1}, z^{k+1}) &= \min_{u,z} E(u,z) + \lambda \|z - Au - b^k\|_2^2 \\ b^{k+1} &= b^k + \left(Au^{k+1} - z^{k+1}\right) \end{aligned} \tag{6.6}$$

where b^{k+1} is a Bregman parameter that ensures $Au \to z$ as $b^{k+1} \to b^k$ converges without increasing λ and sacrificing stability. Because $E(u,z)$ is convex and non-differentiable, equation 6.6 is split into its u and z subproblems, which are solved separately at each iteration, decoupling u from z [10]:

$$\begin{aligned} u^{k+1} &= \min_u E(u, z^k) + \lambda \|z^k - Au - b^k\|_2^2 \\ z^{k+1} &= \min_z E(u^k + 1, z) + \lambda \|z - Au^{k+1} - b^k\|_2^2 \\ b^{k+1} &= b^k + \left(Au^{k+1} - z^{k+1}\right) \end{aligned} \tag{6.7}$$

6.3.3 Group Sparse Reconstruction

GS reconstruction is an extension of CS that exploits the correlations among adjacent transform coefficients caused by their structured sparsity [42, 64, 129]. Structured sparsity, or block sparsity as it is also known, is the tendency of large transform coefficients to be adjacent to each other and form clusters rather than be evenly distributed across the transform domain. In GS reconstruction, adjacent transform coefficients are reconstructed together in groups rather than individually, as is done in CS. By reconstructing groups of coefficients, the GS signal model correlates individual transform coefficients with their neighbors allowing them to influence each other during reconstruction. Because of the structured sparsity relationships among transform coefficients, it has been shown the GS signal model provides results equal to or better than CS with respect to RMSE, which does not exploit these relationships [41, 64].

GS reconstruction can be formed as a constrained convex optimization problem that uses the $l_{1,2}$-norm as the objective function instead of the l_1-norm used in CS. The

$l_{1,2}$-norm over a vector $u \in \mathbb{C}^N$ is defined as:

$$\|u\|_{1,2} = \|u_{g1}\|_2 + \|u_{g2}\|_2 + ... + \|u_{gL}\|_2 \tag{6.8}$$

where $u_{gi} \in \mathbb{C}^P = \{u_j, u_k ... u_n\}$ and $j, k, n \in \{S = 1...N, P \leq N\}$ is one of the L groups of u. Because the u_{gi} groups may overlap, $\|u\|_{1,2}$ is non-convex and variable substitution must be used on u to ensure that GS reconstruction is a convex optimization problem:

$$\begin{aligned} &\min_{u,z} && \|z\|_{1,2} \\ &\text{such that} && \|R\mathcal{F}u - f\|_2 \leq \sigma \\ & && z = Gu \end{aligned} \tag{6.9}$$

where z is defined as $z = Gu$ and $G \in \mathbb{R}^{LPxN}$ is the group matrix of 1s and 0s that determines which transform coefficients from u belong to each group in z [125]. G is defined as having a single 1 per row so no z_{gi} overlap but each z_{gi} may contain any number of coefficients from u. The remaining terms are unchanged from equation 6.1. Because each transform coefficient from u may be within more than one z_{gi} group and separate reconstructions must be created for each version of that coefficient, the set of transform coefficient groups, z, may contain more points than u and is an over-complete reconstruction of u.

The GS problem reduces to the CS problem when each group contains one coefficient, thus making $G = I$ and $z = u$. As implemented for these experiments, the grouping pattern must offer complete coverage of the entire 4D MRSI volume so that each spatial, spectral-domain coefficient is contained in at least one group.

6.3.4 Split-Bregman Based Group Sparse Reconstruction

The GS reconstruction problem is generally considered difficult to solve due to its mixed norm structure and the non-smooth nature of the $l_{1,2}$ objective function. However, by applying Split-Bregman iterative relaxation, we can solve equation 6.9 for the optimal MRSI reconstruction to within the standard deviation of noise with ADMM convergence guarantees [55]. In order to apply the Split-Bregman algorithm, equation 6.9 is formed

as an unconstrained problem and both constraints converted to equality:

$$\min_{u,z} E(u,z) + \lambda H(u,z) \tag{6.10}$$

where

$$\begin{aligned} E(u,z) &= \|z\|_{1,2} + \mu\|R\mathcal{F}u - f\|_2^2 \\ H(u,z) &= \|z - Gu\|_2^2 \end{aligned} \tag{6.11}$$

Relaxing equation 6.9 into 6.10, forms $E(u,z)$ as a combination of the objective function and fidelity constraint through the Lagrange multiplier, μ, which would normally cause the reconstruction result to depend heavily on the initial value for μ; however, as will be shown, the Bregman iterative framework reduces the dependence on μ by treating the sampled data, f, as a Bregman parameter and updating it accordingly throughout the reconstruction [92].

Because $H(u,z)$ is of the form $Au = z$, we can use the simplified Bregman distance and iterative scheme from equation 6.6 to relax equation 6.10:

$$\begin{aligned} (u^{k+1}, z^{k+1}) &= \min_{u,z} \|z\|_{1,2} + \mu\|R\mathcal{F}u - f\|_2^2 \\ &\qquad +\lambda\|z - Gu - b^k\|_2^2 \\ b^{k+1} &= b^k + \left(Gu^{k+1} - z^{k+1}\right) \end{aligned} \tag{6.12}$$

Iterating over k until convergence, the Bregman parameter $b^{k+1} \to b^k$ ensures that $z \to Gu$ and the equality constraint from equation 6.9 is satisfied. Because $E(u,z)$ was previously split into its $l_{1,2}$ and l_2 components during the variable substitution of equation 6.9, we split equation 6.12 into its u and z sub-problems, which can be efficiently solved by separately minimizing with respect to u and z [10, 55]:

$$\begin{aligned} u^{k+1} &= \min_u \mu\|R\mathcal{F}u - f\|_2^2 + \lambda\|z^k - Gu - b_z^k\|_2^2 \\ z^{k+1} &= \min_z \|z\|_{1,2} + \lambda\|z - Gu^{k+1} - b_z^k\|_2^2 \\ b_z^{k+1} &= b_z^k + \left(Gu^{k+1} - z^{k+1}\right) \end{aligned} \tag{6.13}$$

The u^{k+1} sub-problem is now a function of u with z^k treated as a constant, and the z^{k+1} sub-problem treats u^{k+1} similarly. The z^{k+1} sub-problem is non-differentiable,

however, its equivalent problem can be solved as:

$$\begin{aligned} z^{k+1} &= \min_z \sum_{i=1}^{L} \left[\|z_{gi}\|_2 + \lambda \|z_{gi} - (Gu^{k+1})_{gi} - (b_z^k)_{gi}\|_2^2 \right] \\ &= gshrink(Gu^{k+1} + b_z^k, \tfrac{1}{\lambda}, G) \end{aligned} \tag{6.14}$$

where $gshrink$ is group-wise shrinkage over each group, instead of individual coefficients, and has the closed form solution:

$$z_{gi}^{k+1} = \quad max\left(0, 1 - \frac{1}{\lambda \|x_{gi}\|_2}\right) \cdot x_{gi} \tag{6.15}$$

where $x_{gi} = (Gu^{k+1})_{gi} - (b_z^k)_{gi}$. The u^{k+1} sub-problem is differentiable, therefore, optimality conditions can be derived for u and simplified to:

$$(\mu \mathcal{F}' R' R \mathcal{F} + \lambda G' G) u^{k+1} = \mu \mathcal{F}' R' f + \lambda G' \left(z^k - b_z^k\right) \tag{6.16}$$

where $G'G$ is a diagonal matrix with each $(G'G)_{ii}$ being the number of groups that contain transform coefficient u_i^{k+1} [125]. If each transform coefficient is in the same number of groups, so that $G'G$ is a multiple of I, the left-hand side of equation 6.16 is circulant and can be easily inverted by the Fourier transform [55]:

$$u^{k+1} = \mathcal{F}' K^{-1} \mathcal{F} \left(\mu \mathcal{F}' R' f + \lambda G' \left(z^k - b_z^k\right)\right) \tag{6.17}$$

where $K = (\mu R' R + \lambda G' G)$ is diagonal. If each transform coefficient is not in the same number of groups and $G'G$ is not a multiple of I, u^{k+1} in equation 6.16 can be solved for by the Gauss-Seidel method or other iterative solvers for linear systems..

Iterating the u and z sub-problems and Bregman update over k in equation 6.12 solves the unconstrained problem from equation 6.10, where the Lagrange multiplier, μ, was introduced; however, to solve the constrained problem in equation 6.9 and reduce the dependence of the reconstruction result on the initial value of μ, an outer iteration is completed over i that updates f based on changes to the reconstruction, u^{k+1}:

$$f^{i+1} = f^i + \left(f - R\mathcal{F} u^{k+1}\right) \tag{6.18}$$

where f is the initial value of the sampled data. By replacing f with f^i in equation 6.12 then applying equation 6.18 during each outer iteration, $f^{i+1} \rightarrow f^i$ and $R\mathcal{F}u^{k+1} \rightarrow f$ as the algorithm converges to the solution of the constrained problem [92].

The pseudocode for the Split-Bregman GS MRSI reconstruction algorithm is shown in Algorithm 6.3.1 and incorporates equations 6.12 to 6.18. The inner loop iterates over k and updates u and z, and the outer loop iterates over i and updates the sampled data f^i as a Bregman parameter.

Algorithm 6.3.1: SBGS RECONSTRUCTION(f_0, G, R)

Initialize: $f^0 = f_0, K = (\mu R'R + \lambda G'G)$ and $u^0 = z^0 = b_z^0 = 0$
repeat
 For $k = 1$ to M
  $rhs^{k+1} = \mu\mathcal{F}'R'f^i + \lambda G'\left(z^k - b_z^k\right)$
  $u^{k+1} = \mathcal{F}'K^{-1}\mathcal{F}rhs^{k+1}$
  $z^{k+1} = gshrink(Gu^{k+1} + b_z^k, \frac{1}{\lambda}, G)$
  $b_z^{k+1} = b_z^k + \left(Gx^{k+1} - z^{k+1}\right)$
 end
 $f^{i+1} = f^i + \left(f_0 - R\mathcal{F}u^{k+1}\right)$
until stopping condition met (loop over i)
return $(\mathcal{F}u^{k+1})$

The number of iterations over k is application dependent, but for the 4D MRSI GS problem, we use $M = 15$ iterations over k for each iteration over i and iterate over i until the normalized residual error between u^{k+1} and f^i is less than $10e^{-6}$.

6.4 Methods

6.4.1 MRSI Scans

The CS, TV, MaxEnt, and GS reconstruction methods were quantitatively compared using phantom data from six fully-sampled 4D EP-COSI scans of a 500mL gray matter brain phantom, which contained *in vivo* concentrations of the metabolites: aspartate (Asp), choline (Ch), creatine (Cr), gamma amino butyric acid (GABA), glucose (Glc), glutamate (Glu), glutamine (Gln), glutathione (Gsh), lactate (Lac), myo-Inositol

(mI), N-acetyl-aspartate (NAA), N-acetyl-aspartyl-glutamate (NAAG), phosphocholine (PCh), phosphoryl ethanolimine (Pe), taurine (Tau), and threonine (Thr). The scans were acquired with the volume-based 4D EP-COSI sequence on a Siemens 3T Trio scanner using a 12-channel head coil with the following parameters: 32x32cm^2 FOV, 2x2x2 cm^3 voxel size, 100 t_1 increments, TR/TE/averages = 5s/23ms/1, 256 time points along the t_2 readout, and spectral bandwidths of 1250Hz and 1190Hz along F_1 and F_2 , respectively. The volume of interest (VOI) was positioned within the phantom to allow for a 4x4 grid of voxels to be acquired per phantom scan. Standard phase corrections and channel combination were applied to each scan, with no baseline corrections used. The phantom data was then apodized using a sine-squared filter along t_1, and a skewed sine-squared filter with skew parameter 0.5 along t_2. Following phase correction and apodization, the fully sampled scans were retrospectively under-sampled 2X, 4X, 6X, 8X, and 10X along the $k_y - t_1$ plane using the 2D Poisson-gap sample masks shown in figure 6.2 [19].

In addition to the phantom data comparisons, each reconstruction method was also evaluated on retrospectively under-sampled *in vivo* 4D EP-COSI brain data acquired with the same sequence parameters, except for TR/TE=1.7s/23ms and outer volume suppression (OVS) prior to each TR to suppress the scull marrow fat resonances. The brains of two healthy human volunteers aged 23 and 36 years were scanned using the Siemens 3T Trio scanner with a 12-channel head coil and used the same post-processing and retrospective NUS sample masks as the phantom scans prior to reconstructing with CS, TV, MaxEnt, and GS.

6.4.2 MRSI Scan Reconstruction

Separate reconstructions of each NUS phantom and *in vivo* scan were performed using CS, TV, MaxEnt, GS with non-overlapping groups (GS_1), and GS with 50% overlapping groups (GS_2) [26]. The grouping patterns were within the spectral domain and were comprised of equal-sized groups of $(F_2, F_1) = (8, 4)$ coefficients. No grouping of the coefficients within the spatial dimensions was used. The CS and TV reconstruction

problems were solved using the Split-Bregman algorithm [55] and MaxEnt was solved using the Cambridge algorithm [19, 61]. Because GS simplifies to the CS problem with group sizes of one coefficient, $(F_1, F_2) = (1, 1)$, the CS and GS problems were solved using the same code base, but with different groupings. In order to simplify any necessary parameter tuning, the optimal Lagrange parameters used by the CS reconstruction were used by the GS reconstructions, but scaled by $\frac{1}{G}$, where G is the number of coefficients per group. The optimal TV, CS, and GS Lagrange parameters were chosen by empiric determination and because the Split-Bregman algorithm reduces the dependence of the reconstruction results on the initial value of the Lagrange parameters used, the same values were used for the phantom and *in vivo* scans at each of the NUS rates tested. The Lagrange parameters used by each reconstruction type are shown in Table 6.1.

	μ	λ	γ
CS	1	$1/2$	N/A
TV	1	$1/50$	$1/100$
GS$_1$	1	$1/(2 \cdot 32)$	N/A
GS$_2$	1	$1/(2 \cdot 32)$	N/A
MaxEnt	N/A	N/A	N/A

Table 6.1: Lagrange multiplier values used during reconstruction. The GS reconstructions use the CS parameter values scaled by the number of coefficients per group. The MaxEnt reconstruction does not use Lagrange multipliers.

The MaxEnt algorithm converged when the normalized difference between the gradients of the entropy (S) and residual (C) were parallel: $\|\nabla S/\|S\|_2 - \nabla C/\|C\|_2\| \leq .001$ [19]. The CS/GS and TV implementations of the Split-Bregman algorithm used 15 inner loops per outer loop and converged when the normalized residual error between u^{k+1} and f^i was less than $10e^{-6}$. The maximum number of outer loops was limited to 25 but was never reached.

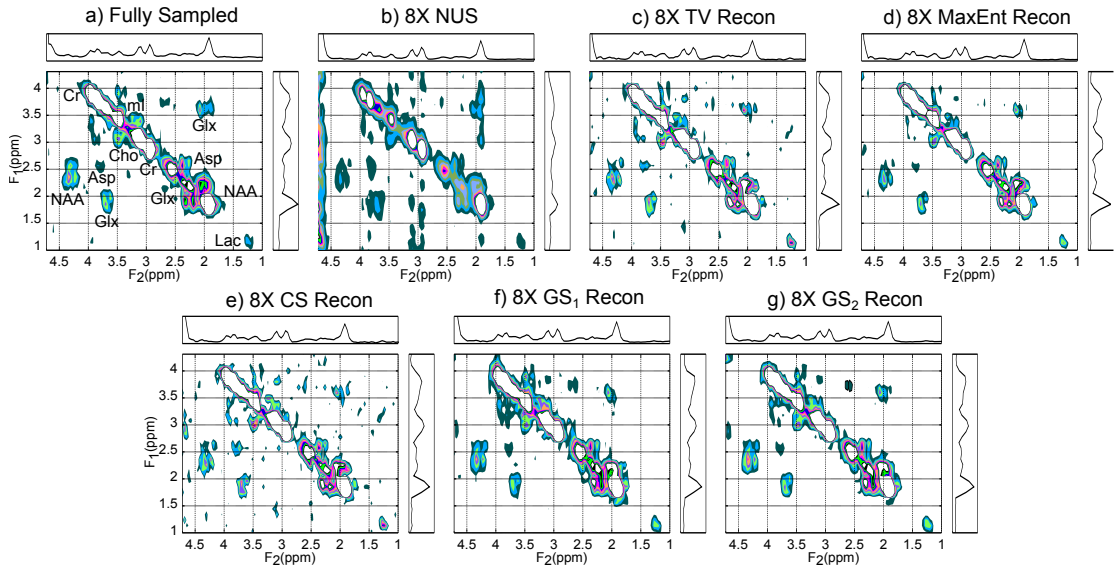

Figure 6.1: Select 2D COSY spectrum from the central voxel of a (a) fully sampled 4D EP-COSI brain phantom scan (b) 8X NUS and the (c) 8X TV (d) 8X MaxEnt (e) 8X CS (f) 8X GS_1 (g) 8X GS_2 reconstructions.

6.5 Results

6.5.1 Gray Matter Brain Phantom

Figure 6.1 shows a select 2D COSY spectrum from the central voxel of a 4D EP-COSI gray matter phantom scan that was retrospectively under-sampled 8X using the phantom mask in Figure 6.2 and reconstructed by CS, TV, MaxEnt, GS_1, and GS_2. Because of the homogeneity of the phantom spectra, a single representative 2D spectrum was chosen to illustrate the qualitative effectiveness of each reconstruction method. The 1D projections of the F_1 and F_2 dimensions are shown to the right and above each 2D spectrum, respectively. The spectrum from the fully sampled phantom scan is shown in the top left of the figure and the 8X NUS spectrum with zeros in place of missing samples is shown to its right. The contour levels of each spectrum are the same as those used for the fully sampled scan to allow noise levels and peak heights to be compared between reconstructions.

As can be seen in the 8X NUS spectrum, the broad point spread function (PSF) of the under-sampling mask caused the large diagonal peaks of NAA, Cr, Cho, and mI

to alias along the F_1 dimension and obscure the much smaller NAA, Glx, mI, and Asp cross-peaks, which have also been spread along F_1 by convolution with the PSF. Because the t_2 dimension was fully sampled, the F_2 projections of the fully sampled, 8X NUS, and reconstructed spectra have similar peak amplitudes and line widths; however, the t_1 under-sampling caused the spectral peaks shown in the fully sampled F_1 projection to collapse in the 8X NUS projection. The F_1 projections of each reconstruction method show reasonable agreement with the fully sampled data set, indicating the peak energy of major diagonals, such as NAA, Cr, Cho, and mI has been deconvolved from the broad PSF by each of the reconstructions.

There are noticeable differences among the reconstructions that should be highlighted. The noise floors of the CS and TV reconstructions are higher than all of the other spectra, which makes identifying cross peaks difficult. The CS and TV reconstructed diagonal peaks have lost their Lorentzian line-shape and the cross peaks are present but *choppy* in appearance, further indicating issues with proper line-shape reconstruction. The MaxEnt and GS reconstructions have noise floors equal to or lower than the fully sampled data set. Cross peaks and diagonals are not *choppy* in appearance, and most of the cross peaks shown in the fully sampled data set can be identified. The MaxEnt reconstruction has lower peak amplitudes than the GS reconstructions and possibly TV, but its low noise floor means low amplitude peaks are not obscured, which was confirmed by adjusting the contour levels down. The peak amplitudes and line shapes of the GS reconstructions are the most similar to the fully sampled data set from all of the reconstructions, as illustrated by the low amplitude NAA and Glx cross peaks, whose complex multiplet structures have been properly reconstructed with reasonable line shapes and widths.

4D EP-COSI data sets are self-sparse along the $Y - F_1$ plane [50]. There are large regions between the metabolite peaks that are dominated by noise, therefore Root Mean Square Errors (RMSE) calculated over the entire data set can be heavily biased by changes to the noise distribution from non-linear reconstruction methods like CS, TV, MaxEnt, and GS. Previous work has demonstrated that constraining the RMSE calculations to the metabolite peaks and ignoring the noise regions is a suitable quantitative

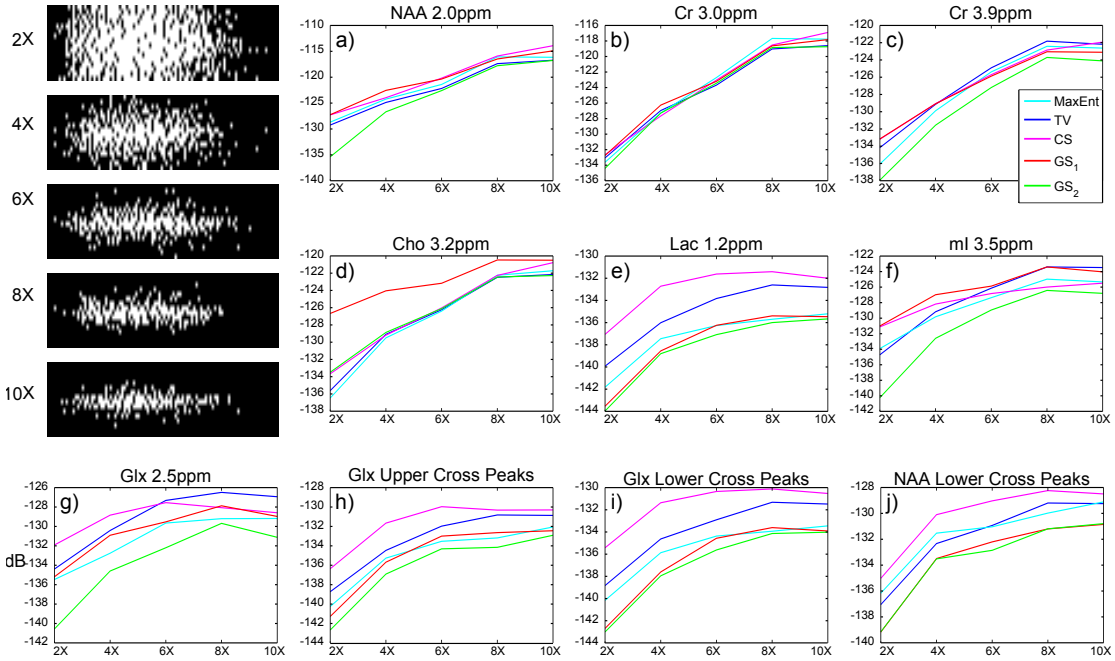

Figure 6.2: (Top Left) NUS masks used to under-sample the $k_y - t_1$ plane of 6 brain phantom scans 2X, 4X, 6X, 8X, and 10X (a-j) Mean metabolite peak RMSEs of under-sampled 4D EP-COSI brain phantom scans versus NUS rate for TV, MaxEnt, CS, GS_1, and GS_2 reconstructions.

metric of reconstruction accuracy that coincides with qualitative observations because it measures amplitude, line-width, and line-shape simultaneously with minimal influence from the noise distribution [19]. Therefore, the mean metabolite peak reconstruction RMSEs of six EP-COSI gray matter brain phantom scans versus NUS rate are shown in figure 6.2 along with the 2X-10X NUS masks used to under-sample the $k_y - t_1$ planes of the phantom and *in vivo* data sets used in these experiments. The RMSEs were calculated for each metabolite peak using the ppm ranges shown in table 6.2. The means were calculated from the central 4x4 VOI of the six phantoms scans used, yielding 96 voxel measurements per metabolite peak. The standard deviations are not shown because they were 2-3 orders of magnitude lower in value than the means.

As can be seen in figure 6.2, the mean reconstruction RMSEs for the large diagonal peaks, NAA 2.0ppm, Cr 3.0ppm, and Cr 3.9ppm are shown at the top of the figure, while smaller diagonal peaks and cross peaks are shown in the middle and bottom, respectively. For the large diagonals, all of the reconstruction RMSEs follow similar

trends at each NUS rate, which is in agreement with the qualitative results from figure 6.1 that indicated each of the reconstruction methods was able to accurately reconstruct the diagonal peaks. However, for the smaller diagonals and cross peaks, the general trend at lower NUS rates is for CS to have the highest RMSE, followed by TV, MaxEnt, GS_1, and GS_2, but at higher NUS rates, MaxEnt has RMSEs equal to or lower than GS_1. The RMSEs of GS_1 for Cho and mI do not follow the general trends of the large diagonal peak RMSEs, nor those of the smaller diagonals and cross peaks; the Cho RMSEs for GS_1 are higher than all other methods for each NUS rate and one of the highest for mI. However, the mean RMSEs for GS_1 of the other metabolites are some of the lowest of the methods tested.

These results demonstrate GS reconstruction has the lowest RMSEs for each metabolite peak and NUS rate, with either GS_2 or GS_1 providing the lowest mean RMSE. The mean RMSEs for GS_2 are consistently lower than GS_1 indicating over-lapping groups may be a more reliable method of metabolite peak reconstruction than non-overlapping groups.

	$F_1(ppm)$	$F_2(ppm)$
Diagonals:		
Cho	3.1 - 3.4	3.1 - 3.4
Cr303	2.9 - 3.1	2.8 - 3.2
Cr391	3.8 - 4.1	3.7 - 4.1
Glx	2.4 - 2.6	2.3 - 2.5
Lac	1.1 - 1.7	1.0 - 1.6
mI	3.5 - 3.8	3.4 - 3.7
NAA	1.7 - 2.3	1.7 - 2.1
Cross Peaks:		
Glx (Lower)	1.7 - 2.2	3.4 - 4.1
Glx (Upper)	3.4 - 3.9	1.7 - 2.4
NAA (Lower)	2.0 - 3.0	4.0 - 4.5

Table 6.2: F_1,F_2 ppm ranges used to calculate the metabolite RMSEs shown in figure 6.2

6.5.2 *in vivo* Brain

The reconstruction results for an *in vivo* 4D EP-COSI brain scan of a healthy 23 year old male are shown in figure 6.3. A representative 2D COSY spectrum was chosen from

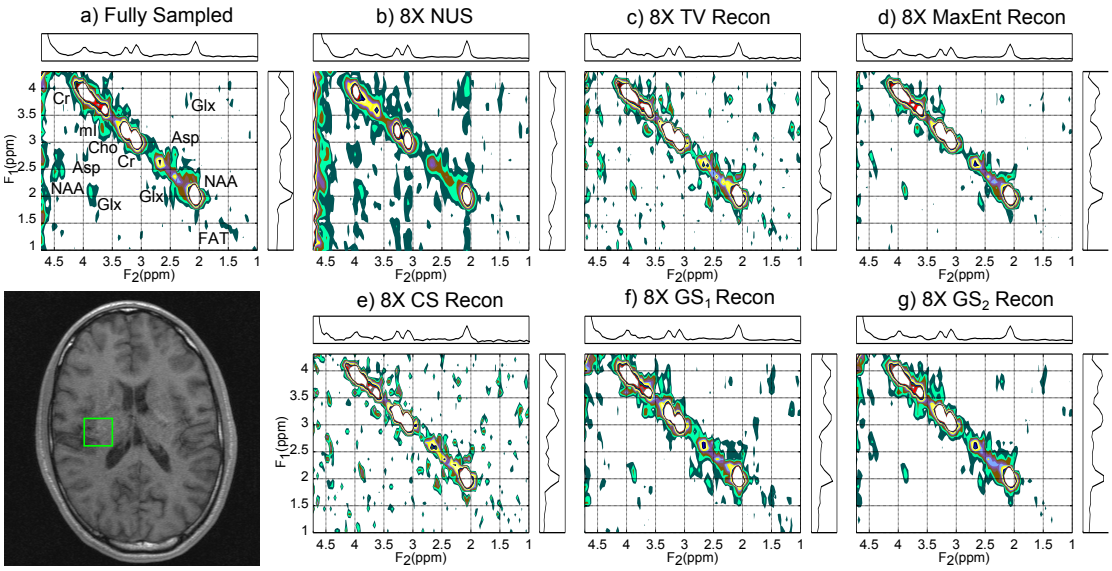

Figure 6.3: Select 2D COSY *in vivo* spectrum from a central voxel of the brain from the (a) fully sampled 4D EP-COSI scan of a healthy 23 year old male (b) 8X NUS and the (c) 8X TV (d) 8X MaxEnt (e) 8X CS (f) 8X GS_1 (g) 8X GS_2 reconstructions.

a central voxel of the brain that shows each of the metabolites of interest with low fat and water contamination, as illustrated by the green square on the T1-weighted image in the bottom left of figure 6.3. The fully sampled spectrum in the top left corner of the figure was under-sampled 8X using the sample mask from figure 6.2, then reconstructed by CS, TV, MaxEnt, GS_1, and GS_2 as shown.

As is seen in figure 6.1, the 8X NUS spectrum shows significant aliasing of the diagonal peaks along F_1 and a collapse of the peaks within the F_1 projection. The CS and TV reconstructions have higher noise floors than the other reconstructions and narrower line-widths, as can be seen at the base of each diagonal peak. The GS reconstructions produced the most accurate reconstructions of the peak line-widths and were able to maintain the noise level. The NAA and Glx cross peaks can be partially seen in each of the reconstructions; however, they are obscured by noise in the CS and TV reconstructions and have low amplitudes in the MaxEnt and GS_1 reconstructions. GS_2 was able to reconstruct the cross peaks to a reasonable degree in spite of the large water tail along F_1 at $F_2 = 4.72ppm$ that nearly obscured the lower NAA cross peak.

Figure 6.4 shows the spatial distribution of a 1.5x1.5ppm region of a 2D COSY

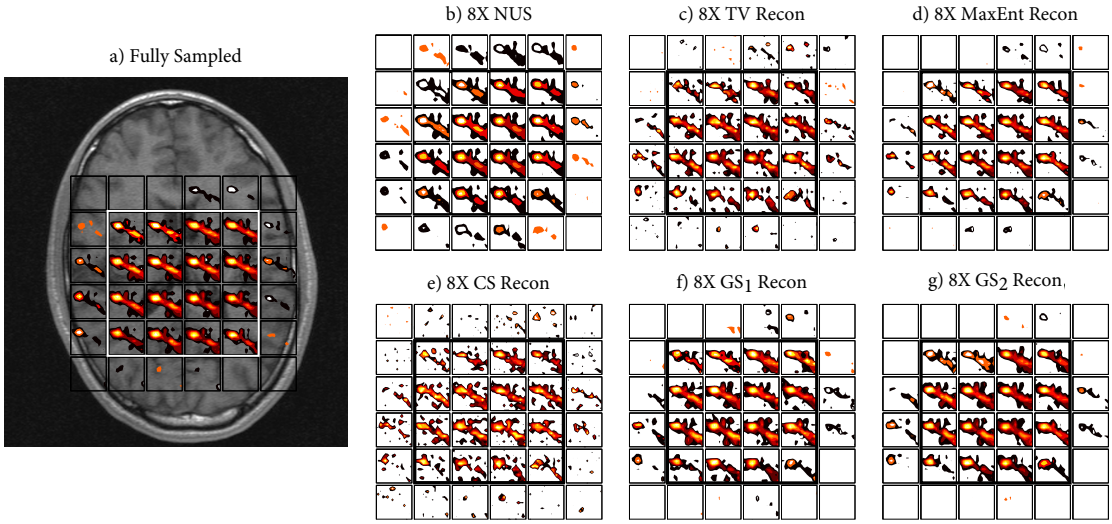

Figure 6.4: Spatial distribution of a 1.5x1.5ppm spectral region centered at 2.5ppm that contains the Glx and NAA/NAAG diagonal peaks from the (a) fully sampled *in vivo* 4D EP-COSI brain scan of a healthy 23 year old male (b) 8X NUS and the (c) 8X TV (d) 8X MaxEnt (e) 8X CS (f) 8X GS_1 (g) 8X GS_2 reconstructions.

spectrum centered at F_2=2.5ppm taken from each voxel of the fully sampled, 8X NUS, and reconstructed *in vivo* 4D EP-COSI brain scan shown in figure 6.3. The fully sampled data is superimposed onto a T1 weighted image from the middle of the EP-COSI slice that was acquired during the same study. Each spectral region contains the metabolite diagonals and cross peaks of NAA/NAAG and Glx in that region. The acquisition VOI used during the scan is shown as the white bolded line in the fully sampled image on the left and the black bolded line in the images on the right. The contour levels used for the fully sampled spectra were used for the 8X NUS and reconstructed spectra. As can be seen, the NAA/NAAG and Glx peaks are well resolved within the VOI of the fully sampled image with minimal spatial aliasing along Y and noticeably more aliasing along X, which was caused by the PSF of the EP-COSI pulse sequence. The peak amplitudes of the NAA/NAAG and Glx peaks are roughly equivalent over the VOI, with the exception of reduced peak amplitudes in the anterior-left and posterior-right voxels. The 8X NUS metabolite peak amplitudes are lower than in the fully sampled image, a trend also seen in figures 6.1 and 6.3, and the increased spatial aliasing along Y is evident from the presence of NAAG and Glx peaks outside of the VOI. The CS and TV reconstructions show increased noise both inside and outside of the VOI, with CS

failing to properly reconstruct many of the peaks in the posterior row of the VOI with the *choppy* line-shapes that were seen in figures 6.1 and 6.3. The MaxEnt reconstruction shows better denoising properties than the CS and TV reconstructions with most of the NAA/NAAG and Glx peak amplitudes and line-widths restored within each voxel of the VOI. The NAA/NAAG and Glx peaks are properly localized within the VOIs of the MaxEnt and GS reconstructions to within the same levels of spatial aliasing seen in the fully sample image. The line-widths and amplitudes of the GS_1 and GS_2 reconstructed peaks are the most qualitatively similar to the fully sampled scan.

	CS			**TV**			**MaxEnt**		
	4X	6X	8X	4X	6X	8X	4X	6X	8X
Lac 1.2	-136.6	-134.8	-134.4	-140.2	-138.5	-137.9	-141.3	-140.4	-140.0
NAA 2.0	-130.9	-127.8	-126.1	-131.9	-127.9	-124.6	**-133.9**	-129.8	-126.8
Glx 2.2	-132.2	-129.4	-128.9	-136.6	-131.7	-131.6	-137.3	-134.2	-134.0
Cr 3.0	-130.3	-128.6	-126.1	-130.8	-128.1	-124.9	**-133.4**	**-132.0**	-126.2
Cho 3.2	-131.6	-129.9	-127.6	-133.3	-130.7	-126.2	-134.2	-131.5	-128.2
mI 3.5	-129.1	-128.5	-128.1	-132.0	-130.9	-127.3	-131.3	-131.5	-129.0
Cr 3.9	-131.0	-130.0	-128.2	-132.6	-129.4	-126.6	-134.3	-131.8	-129.5
Glx UCP	-136.3	-134.9	-133.6	-140.7	-139.2	-136.4	-144.6	-142.0	-141.4
Glx LCP	-135.5	-134.8	-133.7	-139.7	-138.1	-137.2	-142.2	-139.7	-138.3
NAA LCP	-134.3	-132.9	-132.5	-137.8	-136.0	-135.2	-139.2	-137.8	-136.1

	GS_1			**GS_2**		
	4X	6X	8X	4X	6X	8X
Lac 1.2	-143.0	-141.0	-138.7	**-143.4**	**-142.1**	**-141.1**
NAA 2.0	-125.9	-124.5	-122.4	-133.0	**-130.8**	**-127.1**
Glx 2.2	-139.3	**-138.2**	-134.3	**-139.6**	-137.4	**-135.0**
Cr 3.0	-130.3	-127.7	-126.3	-131.8	-131.7	**-127.6**
Cho 3.2	-126.0	-126.1	-122.8	**-135.1**	**-133.4**	**-130.2**
mI 3.5	-131.3	-131.2	-128.8	**-138.2**	**-136.3**	**-133.3**
Cr 3.9	**-137.5**	-133.5	**-132.5**	-136.6	**-134.4**	-130.1
Glx UCP	-146.0	-142.6	-137.9	**-146.1**	**-143.1**	**-141.6**
Glx LCP	-143.1	-139.5	-138.3	**-144.5**	**-141.7**	**-139.9**
NAA LCP	-140.3	-137.2	-134.5	**-141.4**	**-139.4**	**-136.9**

Table 6.3: Mean meatbolite peak RMSEs (dB) for the 4X, 6X, and 8X NUS reconstructions calculated over the 4x4 VOI of the *in vivo* 4D EP-COSI brain scan shown in figures 6.3 and 6.4. The lowest RMSE per metabolite peak and NUS rate is highlighted.

Table 6.3 shows the mean metabolite peak RMSEs calculated over the 4x4 voxel VOIs of the 4X, 6X, and 8X NUS reconstructions of the *in vivo* 4D EP-COSI brain scan shown in figures 6.3 and 6.4. The RMSEs were calculated using the ppm locations shown in table 6.2 and the lowest values calculated for each metabolite peak and NUS rate are highlighted. As can be seen, the majority of highlighted RMSEs are from the GS_2

reconstructions with a handful highlighted for the GS_1 and MaxEnt reconstructions. These results are similar to what was shown in the metabolite RMSE plots in figure 6.1, which showed GS_2 and GS_1 having most of the lowest values followed by MaxEnt. Additionally, the values of the RMSEs for the large diagonal peaks of NAA and Cr are more tightly grouped than the smaller diagonal and cross peak RMSEs, and the high GS_1 RMSEs for Cho 3.2ppm indicate it had trouble reconstructing the metabolite peak, as in figure 6.1.

6.6 Discussion

In this article, an algorithm to solve the GS reconstruction problem using the Split-Bregman framework was derived that allows for arbitrary grouping patterns of transform coefficients and was applied to reconstructing retrospectively under-sampled 4D EP-COSI data. Results for GS reconstruction using overlapping and non-overlapping, equal sized groups were compared against results from CS, TV, and MaxEnt reconstructions at NUS rates of 2X, 4X, 6X, 8X, and 10X on gray matter phantom and *in vivo* brain data. Figures 6.1, 6.3, and 6.4 show that spectra reconstructed by GS reconstruction using overlapping coefficient groups (GS_2) are the most qualitatively similar to the fully sampled spectra with respect to the noise floor, metabolite peak amplitudes, line-widths, and spatial localization. The metabolite peak RMSEs calculated over the VOIs of the phantom and *in vivo* data sets in figure 6.2 and table 6.3 show that the GS_2 reconstructed spectra also have the lowest values for the majority of peaks evaluated, which indicates they are more accurately reconstructed than the other methods tested. The agreement between these results indicate that GS_2 is the most effective means of reconstructing NUS 4D EP-COSI phantom and *in vivo* data tested. The higher noise floor and dynamic range from water and fat contamination in the *in vivo* scans did not prevent GS_2 from successfully reconstructing the highly under-sampled data.

Compared to the other non-GS reconstruction methods, GS_1 produced high quality spectra and was able to reconstruct the metabolite peaks to a higher degree of fidelity; however, as indicated by the mean metabolite peak RMSEs in figure 6.2 and table 6.3,

the Cho 3.2ppm diagonal peak was not reconstructed by GS_1 as accurately as it was by the other reconstruction methods. This discrepancy was caused by the nature of the grouping method used for GS_1, which used equally sized non-overlapping groups of $(F_2, F_1) = (8, 4)$ coefficients. The Cho 3.2ppm diagonal peak was located at the intersection of multiple coefficient groups, therefore, the structural block of coefficients that comprised the peak were divided into multiple groups and were not correlated with one another. Instead of increasing the sparsity of the coefficients around the peak and reducing it at the peak, this division had the opposite effect and prevented the Cho 3,2ppm peak from being properly reconstructed. In contrast, GS_2 was able to reconstruct the Cho 3.2ppm diagonal peak to a higher degree of fidelity with the same sized coefficient groupings because of their overlap and the increased coverage that it provided. It is clear from this result that the coefficient groupings correlate the reconstructed values of adjacent transform coefficients, but overlapping groups correlate the reconstructed values of adjacent groups and minimize the effects of grouping patterns that don't effectively take advantage of structural sparsity.

These results agree with previous work that showed MaxEnt reconstruction outperforming CS reconstruction of NUS 4D EP-COSI simulated and *in vivo* breast data [19]; however, other work reconstructing NUS 4D EP-JRESI phantom and *in vivo* data showed TV results at a higher data fidelity than was shown here. 4D EP-JRESI reconstructions of phantom and *in vivo* data were completed as part of this work, but were excluded for brevity. In the experiments not shown, TV reconstruction performed as well or better than some of the other reconstruction methods. The main difference between these experiments is the phase characteristics of 4D EP-COSI versus 4D EP-JRESI data. EP-COSI has a high degree of phase modulation across t_1 that must be preserved during reconstruction. EP-JRESI does not have the same degree of phase variation across t_1 as EP-COSI, so the signal phase is of less importance. Because TV applies the differential operators in magnitude mode and only imparts phase information into the reconstruction through the fidelity constraint, the phase characteristics of EP-COSI data are not adequately reconstructed. A phase sensitive TV reconstruction, in which separate TV regularizers are applied to the real and imaginary channels, may

have improved results with 4D NUS EP-COSI reconstruction. This dependence on the sequence phase characteristics and the effect each reconstruction method has on it is a topic of future research and will be explored further.

As it is currently implemented, the Split-Bregman GS problem converges in fewer outer iterations than the CS problem, however, it takes more time to compute per iteration because of the group-wise shrink. A typical 4D EP-COSI reconstruction of GS_2 takes 15 minutes to converge on a 64-bit dual core, 3.4 GHz Core i7 processor with 16GB RAM, while CS takes 5 minutes. A more efficient implementation of group-wise shrink using distributed processing techniques is currently under development.

6.7 Conclusion

This work shows that GS reconstruction is a viable alternative to CS, TV, and MaxEnt-based reconstruction of 4D NUS EP-COSI data. The Split-Bregman based GS algorithm was derived and evaluated on phantom and *in vivo* data sets under-sampled 2X, 4X, 6X, 8X, and 10X. GS reconstruction with over-lapping groups results demonstrated the best metabolite peak reproduction, lowest mean metabolite peak RMSEs, and best denoising characteristics of the iterative reconstruction methods tested. Further work is required to determine the optimal grouping strategies under different experimental conditions and how they affect the reconstruction results.

CHAPTER 7

INSEP-JRESI

This chapter is the proof of a manuscript that was written as part of this dissertation research and will be submitted for publication. It is reproduced in full with only the formatting changed to match the dissertation style. The planned title of this manuscript is: *Spatio-temporal Artifact Corrections of Multi-dimensional Spectroscopic Imaging Data.*

7.1 Abstract

Multi-dimensional spectroscopic imaging (MRSI) acquisitions occur in the presence of numerous sources of phase error that can produce non-linear shifts in the spatial-spectral domain, which blur the true locations of metabolite peaks and distort their spectral lineshapes. Existing phase correction techniques do not take into account the coupled nature of these phase errors and attempt to address them individually or within the incorrect spatio-temporal domain. This work categorizes phase errors in MRSI as time varying, space varying, or space and time varying, and proposes a post-processing pipeline that decouples these phase errors from each other so that they can be addressed in the appropriate domain and removed from the data. The 4D Interleaved Navigator Scan corrected Echo Planar J-Resolved Spectroscopic Imaging (INSEP-JRESI) sequence is proposed, which incorporates an interleaved water navigator scan into each TR to track $\Delta B_0(t)$ field drifts and correct them in post-processing. A k_x-dependent first-order phase correction along F_2 is derived that allows the even and odd echoes of an EPI-based readout to be combined in phase. Eddy currents are removed in k-space so that the spatial Point Spread Function (PSF) is narrowed and their effects on the spatial distribution of metabolite peaks is minimized. Results for gray matter phantom scans

using the INSEP-JRESI sequence and proposed pipeline are compared to results from a popular phase deconvolution technique called Klose's method. These results show that the new processing pipeline produces metabolite peak amplitudes up to 10% higher with improved line-shapes and spatial distributions when compared to Klose's method. The cost of these improvements in spectral localization and SNR is minimal increases in post-processing and scan time.

7.2 Introduction

In vivo changes to metabolite concentrations can be detected non-invasively using single voxel magnetic resonance spectroscopy (MRS). Because of the altered metabolism of cancer, it has the potential to aid in tumor classification and detection based on the biochemical differences between healthy and diseased tissues [7, 54, 77, 119]. Two dimensional MRS, which has increased spectral dispersion over 1D MRS, can be used to disentangle over-lapping 1D spectral peaks that make it difficult to identify individual metabolites and estimate their concentrations [2]. With the advent of Magnetic Resonance Spectroscopic Imaging (MRSI), timely multi-voxel support was added to MRS by interleaving the acquisition of one spectral and one spatial dimension along an echo-planar spectroscopic imaging (EPSI) readout [83, 86, 97]. Like 1D MRS, EPSI-based sequences were limited to a single spectral dimension until the introduction of the 4D Echo-Planar based Correlated Spectroscopic Imaging (EP-COSI) and 4D Echo Planar J-Resolved Spectroscopic Imaging (EP-JRESI) sequences, which allow for the simultaneous acquisition of two spatial (k_y, k_x) and two spectral (t_2, t_1) dimensions during a single scan [78, 88]. Like EPSI, the EP-COSI and EP-JRESI sequences interleave the acquisition of the k_x and t_2 dimensions within the EPI read-out, and use standard MRI phase encoding techniques to acquire k_y. The t_1 dimension is acquired as an incrementally increasing delay within the sequence timing, thus forming a second spectral dimension.

MRSI data are acquired in the presence of numerous sources of B_0 field shifts and phase errors that can distort the pulse sequence's spatio-temporal Point-Spread Function

(PSF). These sources of phase error can be grouped into three distinct categories [4]: those that are time varying and spatially invariant during the scan ($\Delta B_0(t)$), such as B_0 field drift, those that are spatially dependent but independent of time ($\Delta B_0(x,y)$), such as susceptibility variations across the VOI and $\Delta\Phi^c(x,y)$ spatial phase gradients imposed by the multi-channel phased array coils [101, 128], and those that are both spatially and temporally dependent ($\Delta B_0(x,y,t)$), such as eddy-currents and ^{1}H spin motion from patient movement or diffusion. For the purposes of this article, only the eddy current component of $\Delta B_0(x,y,t)$ is considered.

The time dependence of $\Delta B_0(x,y,t)$ eddy currents produces frequency shifts and phase modulation along F_2 that broaden spectral peaks and distort phase sensitive spectra acquired over multiple TRs [61, 73], while the k-space dependent portion of $\Delta B_0(x,y,t)$ eddy currents induces phase changes in k-space that blur and shift the true locations of spectra along X [71, 100]. Because EPI-based MRSI sequences read out the k_x and t_2 dimensions simultaneously, eddy currents caused by the EPSI readout gradients broaden the PSF of the mixed-domain (k_x, t_2) plane and distort the spatial distribution of spectral peaks after convolution with the (X, F_2) plane.

$\Delta B_0(t)$ magnetic field drift is caused by heating of the shim coils by gradient switching induced vibrations and other external sources of field instability that introduce time dependent phase shifts into the data [38, 45]. These time-domain phase errors create frequency dependent spectral peaks shifts in F_2 and add time-dependent phase shifts to k_y, which blur the spatial localization along Y. These ΔB_0 phase shifts have a disproportionate effect on the low SNR cross-peaks within a 4D MRSI spectrum. The 2D spectral cross-peaks are the result of indirectly sampling the J-modulation between coupled spin systems with a uniformly increasing phase delay along F_1, which becomes time-varying in the presence of $\Delta B_0(t)$. Because t_1 is increased every k_y TRs, a 1.5s TR with 16 phase encodes along k_y will increment t_1 every 24 seconds. During that sample spacing, t_1 incurs unwanted phase evolution from $\Delta B_0(t) = 0.3 - 0.1$ppm/hr at 3T, which is on the order of the 5-15Hz J-modulation frequencies being sampled [38, 56, 118].

The spatially dependent $\Delta B_0(x,y)$ and $\Delta\Phi^c(x,y)$ terms cause first and zeroth order phase shifts within the spectra, respectively [128]. $\Delta B_0(x,y)$ also interferes with water

suppression and spatial localization by causing spatially dependent frequency shifts over the VOI [70], while $\Delta\Phi^c(x, y)$ imposes a coil dependent phase gradient on multi-channel data sets that can cause destructive interference of phase sensitive spectra during channel combination if not removed.

Previous work in single voxel MRS to correct for ΔB_0 errors removed the time domain component of $\Delta B_0(x, y, t)$ eddy current induced phase evolution using Klose's method, a deconvolution of the metabolite data with a non-water suppressed (NWS) signal acquired using the same pulse sequence [73]. The NWS signal provides a single resonance peak whose phase can be used to model t_2 dependent eddy currents and off-resonance B_0 shifts. The NWS samples the t_2 phase evolution during one TR, therefore it does not model the $\Delta B_0(t)$ field drift over the course of the scan. It models the t_2 phase evolution within a single TR well, and can be used to remove the dominant phase error terms caused by eddy current and phased array coil gradients. However, deconvolution of the time domain signal with a NWS reference can cause ringing in the frequency domain and inject additional noise into the metabolite data when the reference decays close to zero [112, 126]. For multi-voxel MRSI, this method is used with a spatially localized NWS reference to remove time dependent $\Delta B_0(x, y, t)$ phase shifts caused by eddy currents along t_2, but must be applied in the spatial domain in order to preserve the spatial information encoded in the (k_x, k_y) phase modulation in k-space. This is problematic because eddy current phase shifts are time and k-space dependent, therefore, removing them in the time, spatial domain through Klose's method does nothing to remove the $\Delta B_0(x, y, t)$ induced phase evolution of k-space, leaving spatial artifacts in place.

$\Delta B_0(t)$ magnetic field drift was first addressed by Thiel et al. in single-voxel MRS using a NWS interleaved navigator scan (INS) within each TR that was acquired using the same pulse sequence as the metabolite data but with a reduced excitation flip angle [118]. By interleaving the NWS, they could model and deconvolve the $\Delta B_0(t)$ induced phase shifts at each TR as well as t_2 dependent eddy-current effects using Klose's method. INS was later refined by using the interleaved navigators to perform real-time $B_0(t)$ tracking, which allowed the center frequency to be adjusted after each

TR and ensured water suppression was not compromised by $\Delta B_0(t)$ drift [74]. Multi-voxel INS has been incorporated into EPSI and CSI-based sequences that used the t_2 phase evolution at the center of k-space and an excite-acquire INS, respectively, to estimate $\Delta B_0(t)$ [39, 96]. However, these multi-voxel techniques use Klose's method in the spatial dimension, thus leaving spatial artifacts in place.

The question of decoupling estimates for the error terms: $\Delta B_0(t)$, $\Delta B_0(x, y, t)$, $\Delta B_0(x, y)$, and $\Delta\Phi^c(x, y)$ from each other has not been addressed for MRS and MRSI. Eddy currents from $\Delta B_0(x, y, t)$ and spatial phase gradients from mutli-channel phased array coils $\Delta\Phi^c(x, y)$ can offset $\Delta B_0(t)$ estimates and cause over or under-estimation of $\Delta B_0(t)$ field drift [38]. Additionally, $\Delta B_0(x, y)$ and $\Delta\Phi^c(x, y)$ phase gradients in the spatial domain, shift k-space so its true center is unknown, while $\Delta B_0(x, y, t)$ eddy currents shift the locations and phases of spectral peaks along the (X, F_2) plane. Ideally, $\Delta B_0(t)$ estimates should be made without the influences of any other sources of phase error, and $\Delta B_0(x, y, t)$ induced eddy currents should be removed from k-space, not the spatial domain, which is currently not possible using Klose's deconvolution. Once $\Delta B_0(x, y, t)$ eddy currents are removed and the spatial PSF is narrowed, $\Delta\Phi^c(x, y)$ phase gradients should be removed from the spatial domain so that multi-channel coil combination can be done in phase. By decoupling B_0 phase shifts and $\Delta\Phi^c(x, y)$ phase gradients in this way and addressing them within the domain in which they occur, estimates for each source of error can be more accurately estimated and removed.

In the present work, we propose the 4D Interleaved Navigator Scan corrected EP-JRESI (INSEP-JRESI) pulse sequence in section 7.3.1 and a multi-step phase correction post-processing pipeline that decouples each of the sources of phase error discussed above in sections 7.3.2, 7.3.3, and 7.3.4. The multi-step phase corrections begin by making phase estimates for the initial off-resonance and $\Delta B_0(t)$ field drift at each TR using an adapted form of the Dynamic Off-resonance in k-space (DORK) technique, which isolates $\Delta B_0(t)$ phase shifts by using a reference line in k-space to remove eddy-current and spatial offsets from phase estimates in fMRI time series data [94]. Once $\Delta B_0(t)$ field drift and off-resonance along t_2 are removed, even-odd echoes along the readout can be k_x and t_2 phase aligned using a k_x dependent phase-shift along F_2 that has

been developed as part of this work [97]. The $\Delta B_0(x, y, t)$ eddy current phase shifts are then removed using a modified Interleaved Dual-Echo Acceleration Echo Planar Imaging (IDEA-EPI) readout with complex echo averaging that removes eddy currents by combining the even-odd EPI echoes [63, 96, 124]. Lastly, because the $\Delta B_0(t)$ and $\Delta B_0(x, y, t)$ phase errors have been removed from k-space, the zero order phase offsets from $\Delta B_0(x, y)$ and $\Delta\Phi^c(x, y)$ are all that remain and can be removed in the spatial domain by standard first point methods. Results for gray matter phantom scans of INSEP-JRESI phase corrections with comparisons to existing techniques using Klose's method are presented in section 7.4. These results show the new technique increase metabolite peak SNR for all metabolites, but especially those furthest from the center frequency, as well as a more uniform spatial distribution of metabolite peaks with less signal bleed along both the X and Y dimensions. These improvements are achieved with increases of only 10-12% in scan time and only minimal increases in the post-processing time.

7.3 Methods

7.3.1 4D INSEP-JRESI Pulse Sequence

A single TR of the 4D INSEP-JRESI pulse sequence is shown in the bottom of Fig. 7.1. It begins with global fat and water suppression using a combination of fat saturation, outer volume suppression (OVS) bands, and four spectrally selective WET pulses centered on water [91]. The fat is suppressed by a spectrally selective 90° pulse at 0.3ppm with a bandwidth of 2ppm and dephasing crushers between the 3^{rd} and 4^{th} WET pulses. The fat and water suppression are immediately followed by the metabolite acquisition using a two pulse, slice-based EP-JRESI excitation with EPI readout [78, 88]. Prior to the navigator water acquisition, any longitudinal fat signal that has regrown during the metabolite acquisition is suppressed using the same fat suppression scheme as before with the saturation pulse centered at 1.3ppm. The fat saturation and dephasing is played immediately before the water excitation to ensure the interleaved navigator contains a single dominant resonance.

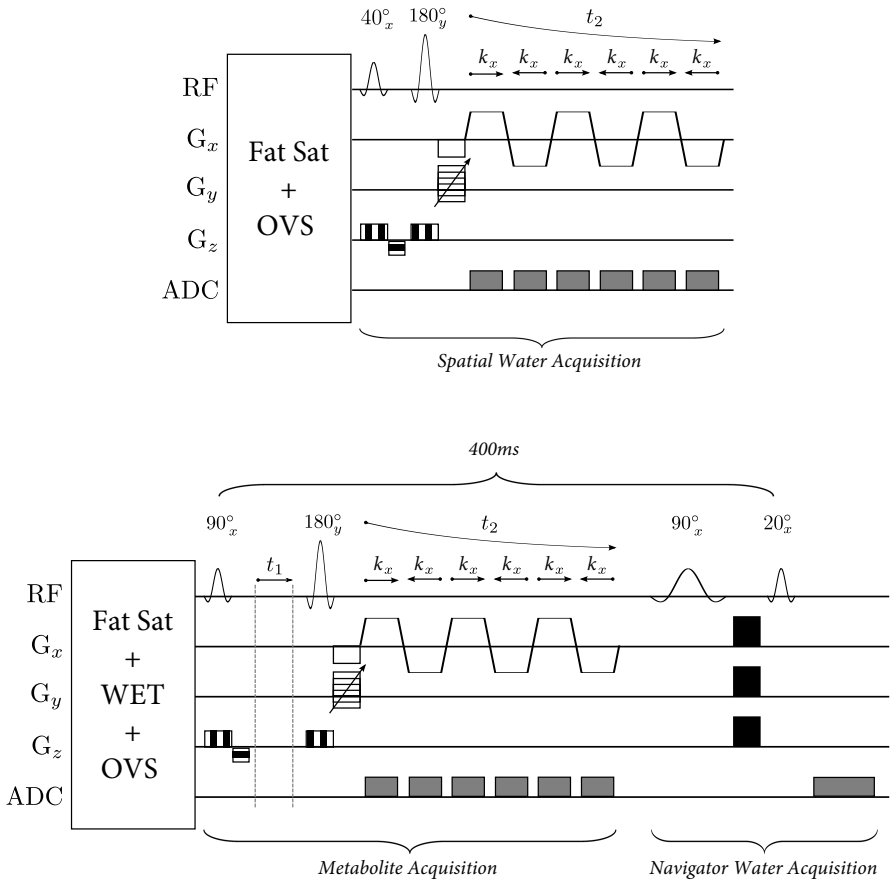

Figure 7.1: 4D INSEP-JRESI pulse sequence. (top) A single TR of the NWS sequence (bottom) A single TR of the WS scan with interleaved navigators sequence.

The 4D EP-JRESI sequence has been described in detail previously [88]. It acquires a spatial and spectral dimension simultaneously by interleaving the k_x and t_2 dimensions along the EPI readout and incrementally acquires the phase encoded k_y spatial dimension as shown [83, 86, 97]. The EP-JRESI sequence acquires a second spectral dimension by incrementing the t_1 delay between the RF pulses, which indirectly samples the J-modulation among coupled spin systems. This causes the resonances for J-coupled spin systems to rotate within the 2D spectrum, so that multiplets split above and below $F_1 = 0$Hz as cross-peaks, and all other resonances appear along $F_1 = 0$Hz. The cross-peak resonances, provide increased spectral dispersion over 1D MRS and can help disambiguate over-lapping metabolite diagonal peaks [2].

The water navigator excitation occurs 400ms after the metabolite excitation to allow

the water signal to regrow after WET water suppression and is held constant for each TR irrespective of the t_1 increment. In order to not disrupt the metabolite signal grow-back for the next TR but acquire a water signal with sufficient SNR, a 20° flip angle is used. No spatial encoding or slice selection is used for the navigator FID acquisition, which uses a 1 kHz spectral bandwidth over 256 sample points. The phase evolution of the navigator over t_2 is used to estimate and remove the $\Delta B_0(t)$ field drift of the metabolite data at each TR during the scan.

The top of Fig. 7.1 shows a single TR of the spatial water acquisition that is performed as part of the 4D EP-JRESI sequence with full k_y, k_x spatial encoding. Instead of running a separate NWS scan using the 4D EP-JRESI sequence with no t_1 increments, the NWS scan is run at the beginning of the pulse sequence prior to the metabolite acquisitions using a reduced TR=1000ms and acquires the spatial phase distribution, $\Delta\Phi^c(x, y)$. The flip angle of the initial excitation pulse is reduced to 40° to accommodate the shorter TR. No WET water suppression is used, however, the same fat suppression scheme used prior to the metabolite acquisition is applied immediately before OVS. The spatial water acquisition is used to remove the spatially dependent phase gradients caused by the multi-channel phased array coil and the initial off-resonance phase evolution of the metabolite acquisition [128]. It acquires a single t_1 with otherwise identical parameters to the metabolite acquisition. The water EPI and metabolite EPI acquisitions are timed to begin a multiple of 1/1190Hz, the spectral bandwidth, after the 180°_y refocussing pulse to ensure their initial on-resonance phases are as close as possible.

There were 7 INSEP-JRESI gray matter brain phantom scans acquired for this work using a 12-channel head phased array coil with the following sequence parameters: TR/TE=1.7s/13ms, 16x16 FOV with 1x1x1.5cm^3 voxels, and F_1/F_2 spectral bandwidths of 1250Hz and 1190Hz, respectively. Each k_x readout acquired 32 oversampled points in each gradient of the 256 bipolar readout pairs. There were 100 t_1 increments and 256 t_2 points from the EPI readout for a total scan time of 45 minutes. The 500mL gray matter brain phantom contained *in vivo* concentrations of the following metabolites: aspartate (Asp), choline (Ch), creatine (Cr), gamma amino butyric acid (GABA),

glucose (Glc), glutamate (Glu), glutamine (Gln), glutathione (Gsh), lactate (Lac), Myo-inositol (mI), N-acetyl-aspartate (NAA), N-acetyl-aspartyl-glutamate (NAAG), phosphocholine (PCh), phosphoryl ethanolimine (Pe), taurine (Tau), and threonine (Thr).

7.3.2 $\Delta B_0(t)$ Field Drift Correction

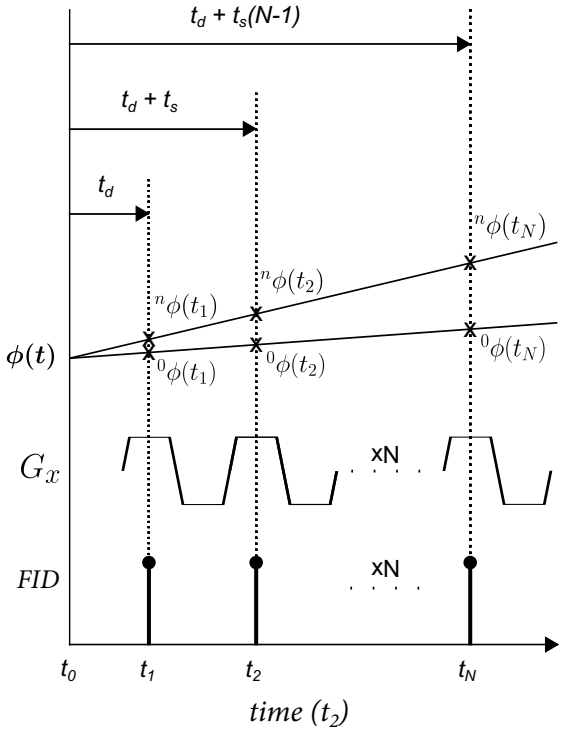

Figure 7.2: Phase along t_2 of 0^{th} and n^{th} TR for FID and EPI-type readouts.

$\Delta B_0(t)$ field drift is a slowly varying process that changes on a time-scale larger than TR=1.7s; therefore, it can be assumed to be pseudo-static within each TR [38]. With this assumption in mind, any off-resonance as a result of $\Delta B_0(t)$ causes the readout to acquire a linear phase evolution along t_2 that is proportional to the field drift and the readout timing. Fig. 7.2 illustrates the unwrapped phase evolution along t_2 for a scan's 0^{th} and n^{th} EPI or FID-based readouts, where the slope of the n^{th} readout's phase evolution has changed due to $\Delta B_0(t)$. The first point of each readout is sampled t_d seconds after the water excitation pulse and has a t_s dwell time between each of the N samples. For EPI-based readouts, the sample point is the center of k_x within each echo.

Using the linear phase model for $\phi(t)$ in Fig. 7.2, the phase of any sample along t_2 can be computed as:

$$\phi(t) = \phi^0 + \omega t + \phi^e(t) \tag{7.1}$$

where $\phi^e(t)$ is due to phase offsets from the phased array coil and eddy current phase terms, $\Delta\Phi^c(x,y)$ and $B_0(x,y,t)$, ϕ^0 is the zeroth-order term describing $\Delta B_0(t)$, and ω is the off-resonance frequency, $\Delta B_0(t)$, within each TR. Because the t_1 timing increments and k_y phase encoding gradients do not alter the INSEP-JRESI pulse sequence considerably between TRs, we can assume the $B_0(x,y,t)$ eddy currents are roughly the same during the 0^{th} TR as they are at any time, p, during the n^{th} TR [71]. Therefore, because the $B_0(x,y,t)$ phase terms are intra-TR dependent, not inter-TR dependent, and the $\Delta\Phi^c(x,y)$ phase is time invariant over the course of a normal 4D EP-JRESI scan, the $\phi^e(t)$ phase term from the 0^{th} and n^{th} TRs are equivalent:

$${}^0\phi^e(t_p) = {}^n\phi^e(t_p) = \phi^e(t_p), \forall p \in t_2 \tag{7.2}$$

Expanding this further, the phase at each point along the t_2 readout from the 0^{th} TR can be defined as:

$$\begin{aligned} {}^0\phi(t_1) = &\ {}^0\phi_1^0 + {}^0\omega_1 \cdot t_1 + \phi^e(t_1) \\ {}^0\phi(t_2) = &\ {}^0\phi_2^0 + {}^0\omega_2 \cdot t_2 + \phi^e(t_2) \\ &\ \vdots \\ {}^0\phi(t_N) = &\ {}^0\phi_N^0 + {}^0\omega_N \cdot t_N + \phi^e(t_N) \end{aligned} \tag{7.3}$$

and the phase at each point along t_2 from the n^{th} TR can be defined as:

$$\begin{aligned} {}^n\phi(t_1) = &\ {}^n\phi_1^0 + {}^n\omega_1 \cdot t_1 + \phi^e(t_1) \\ {}^n\phi(t_2) = &\ {}^n\phi_2^0 + {}^n\omega_2 \cdot t_2 + \phi^e(t_2) \\ &\ \vdots \\ {}^n\phi(t_N) = &\ {}^n\phi_N^0 + {}^n\omega_N \cdot t_N + \phi^e(t_N) \end{aligned} \tag{7.4}$$

At any arbitrary sample time $(p,n) = (t_2, TR)$, where TR is a point in the (k_y, t_1) sample plane, the ϕ^0 and ω phase terms vary from one TR to the next, whereas the $\phi^e(t_p)$ phase terms do not. All phase terms are time dependent on t_2, however, only the

ϕ^0 and ω phase terms are dependent on the TR. Therefore, we can remove the $\phi^e(t)$ phase term by using the phase difference between the t_2 sample points of the n^{th} TR and a reference TR instead of the absolute measured phase. Isolating the (k_y, t_1) dependent phase terms between TRs allows us to estimate $\Delta B_0(t)$ without additional phase offsets from $\Delta\Phi^c(x,y)$ and $B_0(x,y,t)$, which are not the result of field drift. Using $\Delta^n\phi(t)$ instead of ${}^n\phi(t)$ removes these pseudo-static spatial and t_2-dependent phase shifts but leaves (k_y, t_1) dependent phase shifts in place:

$$\begin{aligned}\Delta^n\phi(t_p) &= {}^n\phi(t_p) - {}^0\phi(t_p) \\ &= ({}^n\phi_p^0 - {}^0\phi_p^0) + ({}^n\omega_p - {}^0\omega_p)\cdot t_p + (\phi^e(t_p) - \phi^e(t_p)) \\ &= \Delta^n\phi_p + \Delta^n\omega_p \cdot t_p + 0\end{aligned} \tag{7.5}$$

where $\Delta^n\phi_p^0$ has now been simplified to $\Delta^n\phi_p$. Because the phase contributions from $\phi^e(t_p)$ are assumed to be constant between TRs, they are subtracted out of the phase change estimate and only contributions from $\Delta^n\phi_p$ and $\Delta^n\omega_p$ are left. This modifies equations 7.3 and 7.4 to be:

$$\begin{aligned}\Delta^n\phi(t_1) &= \Delta^n\phi_1 + \Delta^n\omega_1 \cdot t_1 \\ \Delta^n\phi(t_2) &= \Delta^n\phi_2 + \Delta^n\omega_2 \cdot t_2 \\ &\vdots \\ \Delta^n\phi(t_N) &= \Delta^n\phi_N + \Delta^n\omega_N \cdot t_N\end{aligned} \tag{7.6}$$

The resulting phase evolution described by equation 7.6 is only due to $\Delta B_0(t)$ and is linear over t_2. Because $\Delta^n\phi(t_p)$ is now a linear function of $\Delta^n\phi_p$ and $\Delta^n\omega_p$, a general linear model can be fit to the phase differences at each point using Weighted Linear Regression (WLS), which estimates the $\Delta^n\phi$ and $\Delta^n\omega$ terms that describe all of the sampled points within the n^{th} TR. Rewriting equation 7.6 in matrix form and adding a weighting term based on the magnitude of each sampled point, we can solve for $\Delta^n\phi$

and $\Delta^n\omega$ using:

$$\begin{bmatrix} {}^n y_1 \\ {}^n y_2 \\ \vdots \\ {}^n y_N \end{bmatrix} \begin{bmatrix} \Delta^n\phi(t_1) \\ \Delta^n\phi(t_2) \\ \vdots \\ \Delta^n\phi(t_N) \end{bmatrix} = \begin{bmatrix} {}^n y_1 \\ {}^n y_2 \\ \vdots \\ {}^n y_N \end{bmatrix} \begin{bmatrix} 1 & t_1 \\ 1 & t_2 \\ \vdots & \\ 1 & t_N \end{bmatrix} \begin{bmatrix} \Delta^n\phi \\ \Delta^n\omega \end{bmatrix} \tag{7.7}$$

where ${}^n y_p = {}^{|^n x_p|}/_{\sum_{i=1}^{N} |^n x_i|}$ and $|^n x_p|$ is the signal magnitude at time p during the n^{th} TR and t_p is the t_2 sample timing from Fig. 7.2.

$\Delta^n\phi$ and $\Delta^n\omega$ are estimated from the interleaved navigator scan's unwrapped phase at each TR using equation 7.7 and are calculated independently of other TR estimates. The first TR of the interleaved navigator scan is used as the $\Delta^0\phi_p$ reference in each of the calculations. The estimates are assumed to be valid over the entire TR so they can be used to unwind the $\Delta B_0(t)$ phase shifts of the metabolite data acquired prior to the navigator acquisition. The field drift is removed from the metabolite data by multiplying each echo by:

$$e^{-2\pi i \cdot (\Delta^n\phi + \Delta^n\omega \cdot t)} \tag{7.8}$$

where t is the t_2 sample timing of each point within the EPI-based metabolite acquisition after the 180°_y refocussing pulse, not the FID-based interleaved navigator sample timing.

Any initial off-resonance of B_0 must be estimated separately from $\Delta^n\phi$ and $\Delta^n\omega$. It is a constant t_2 dependent phase offset that is present at both the 0^{th} and n^{th} TRs, so it is not part of the field drift estimates above. Therefore, initial off-resonance estimates are made from the central k-space point in the NWS using equation 7.7 with no reference. Prior to this, however, the complex mean of the even and odd EPI echoes in the NWS is taken, which will remove t_2 dependent $\Delta B_0(x, y, t)$ eddy current phase evolution as described in section 7.3.3. A 0^{th} and 1^{st} order phase term for B_0 off-resonance is estimated from the combined even and odd echoes. Any phase offsets caused by the spatial coil phase gradients, k_x phase modulation, or off-resonance phase evolution between the echoes will affect the 0^{th} order phase term, which are ignored. Once the 1^{st} order phase term for the initial off-resonance is calculated, it is added to the $\Delta^n\omega$

estimates at each TR and removed from the metabolite data using equation 7.8.

For estimates of off-resonance, $\Delta^n\phi$, and $\Delta^n\omega$ in multi-channel acquisitions, a separate estimate is calculated for each channel, which is then averaged across the channels. Any values greater than one standard deviation from the mean are discarded and the mean recalculated with that value removed. The mean values are then used to remove any off-resonance and $\Delta B_0(t)$ from each channel.

7.3.3 $\Delta B_0(x, y, t)$ Eddy Current Correction

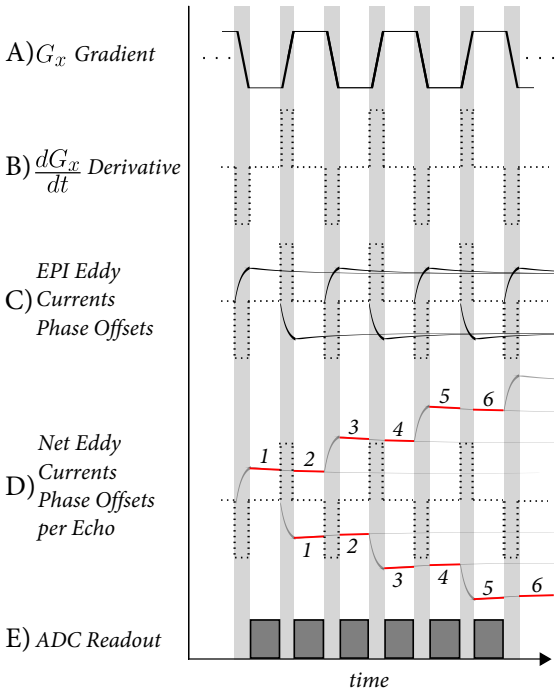

Figure 7.3: Illustration of the relationship between even-odd $\Delta B_0(x, y, t)$ eddy currents during EPI readout. (A) Bipolar gradients for even-odd echo k_x encoding. (B) Time derivative of bipolar gradients. (C) $\Delta B_0(x, y, t)$ eddy current phase offsets induced by gradient switching are proportional to gradient time derivative. (D) Cumulative eddy current phase offsets over t_2 are equal and opposite between adjacent even-odd echo pairs. (E) ADC readout over bipolar gradient flat tops.

During the EPI readout of INSEP-JRESI, $B_0(x, y, t)$ eddy currents distort the trapezoidal bipolar readout gradients, which induces a (k_x, t_2) dependent phase evolution along the readout direction of the 4D volume. As described in sections 7.2 and 7.3.2, the eddy current phase evolution, $\phi^e(t)$, is independent of (k_y, t_1) and only varies across

the (k_x, t_2) plane. Therefore, their effect is to broaden and shift spectral peaks along the (X, F_2) plane and do not affect the (Y, F_1) plane considerably.

As illustrated in fig 7.3, the magnitude of gradient induced eddy currents is proportional to the negative of the gradient waveform's time derivative. The eddy currents created by a single bipolar gradient are primarily induced during the fast gradient switching between gradient flat tops, and then decay to zero over the course of many echoes [9]. Because the INSEP-JRESI pulse sequence reads out during the gradient flat tops and not the gradient ramp times, eddy current distortions along (k_x, t_2) from a single bipolar gradient are restricted to the eddy current's slow decay period, as shown in fig 7.3E [9, 70]. The decay rate for EPI eddy currents is on the order of 10s to 100s of ms [71], so once eddy currents are induced they are present over many bipolar gradients, whose flat top duration is $320\mu s$. Because the decay rate for eddy currents is so much greater than the echo readout time over a single gradient, we can assume that eddy currents are pseudo-static across each echo. However, because of the additional eddy currents induced by subsequent bipolar gradients, they vary between echoes as illustrated in fig 7.3d [63, 96, 124]. Therefore, $B_0(x, y, t)$ eddy currents are assumed to be constant across k_x but vary along t_2.

The even and odd gradients of the bipolar EPI readout have the same ramp and flat top durations, but equal and opposite amplitudes. Therefore, the $B_0(x, y, t)$ eddy currents induced by switching from an even to an odd EPI gradient are equal and opposite to those induced by switching from an odd to an even EPI gradient [9, 71]. Comparing an even echo to the previous odd echo, the cumulative eddy current phase dispersion across k_x from earlier even echoes is equal and opposite to the cumulative odd echo phase dispersion, but sampled one gradient lobe later in time, as illustrated by the echo numbering in fig 7.3D, such that:

$$\begin{aligned} phase(S^+(k_x, t_2)) = &\quad \phi^+(k_x, t_2) + \phi^e(t_2) \\ phase(S^-(k_x, t_2)) = &\quad \phi^-(k_x, t_2) - \phi^e(t_2) \end{aligned} \tag{7.9}$$

where $S^+(k_x, t_2)$ and $S^-(k_x, t_2)$ are adjacent even and odd echoes, $\phi(k_x, t_2)$ is the (k_x, t_2) encoded spatial signal phase for an even or odd echo, and $\phi^e(t_2)$ is the eddy current

induced phase evolution during the flat top gradient. As was first proposed by Hu [63] and later refined by van der Zwaag [124] and Poser [96], $\phi^e(t_2)$ can be removed from the readout by taking the complex mean of adjacent even and odd echoes to produce an eddy current free signal along t_2; however, because the even echoes are sampled an echo time later and must be reversed to align k-space, there are phase differences between $\phi^+(k_x, t_2)$ and $\phi^-(k_x, t_2)$ that must be removed before eddy current echo cancellation can be used.

Once the even echoes are reversed to account for the negative readout trajectory across k-space compared to odd echoes, there is a one point shift along k_x between the even and odd echoes so that the center of k-space occurs one point later in odd echoes versus the even echoes. Because the echoes are oversampled to 32 points, we can align them along k_x by sacrificing the extra spatial resolution by taking only the odd samples from the even echoes and the even samples from the odd echoes.

In addition to the k-space misalignment after reversing the even echoes, the reversal creates a k_x-dependent t_2 timing difference between the even and odd echoes that misaligns their F_2 phase [98]. Prior to the reversal, each point in the even echoes is sampled exactly one echo time after the corresponding point in the previous odd echo. However, after the reversal, this uniform delay becomes k_x-dependent so the points that were sampled at the beginning of the even echo are now shifted toward the end of the echo, and the points that were sampled at the end of the echo are shifted toward the beginning. This delay varies over k_x but is the same between all odd-even echo pairs, so it is a fixed t_2 delay that causes a first order phase shift along F_2 in each even echo [61].

Because the k_x and t_2 sample timings of the even and odd echoes are known, the delay can be calculated for the n^{th} k_x sample as:

$$\Delta t_n(k_x) = t_s - t_d \cdot (2 \cdot n - N_x - 1) \tag{7.10}$$

where t_s is the odd-even echo sampling delay along the readout, t_d is the sample spacing between k_x points within the echo, and N_x is the total number of k_x points per echo. The delay is linear across k_x and takes into account the 1 point k-space shift between

even and odd echoes after the reversal. From the k_x-dependent even echo delay, the phase evolution correction across F_2 can be computed as:

$$\Delta\phi_{m,n}(k_x, t_2) = e^{2\pi i \cdot f_m \Delta t_n(k_x)} \tag{7.11}$$

where f_m is the F_2 frequency being corrected.

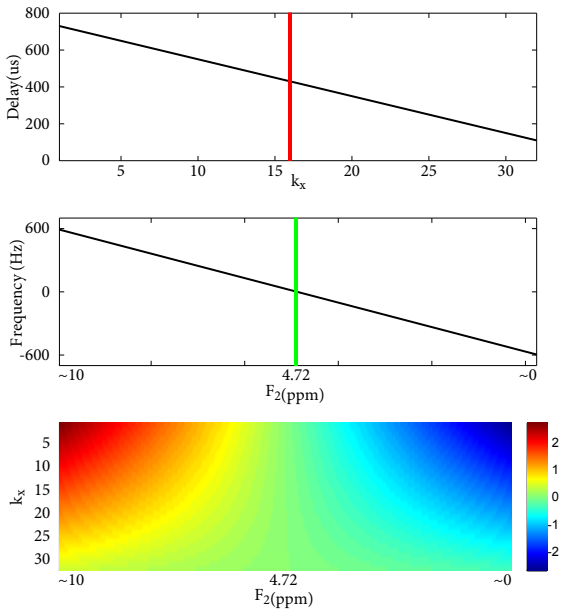

Figure 7.4: Calculation of the k_x dependent, first order frequency shift across F_2 caused by reversing the even echoes (top) Time delay, $\Delta t(k_x)$, between corresponding odd-even k_x points after even echo reversal for 32 k_x points, 320μs readout per echo, and 420μs delay between echoes (middle) Frequency, f, across F_2 with water at 0Hz in the center of an 1190Hz bandwidth (bottom) Frequency dependent phase correction across F_2 caused by k_x dependent t_2 delay, calculated as: $e^{2\pi i \cdot f \Delta t(k_x)}$

Fig. 7.4 illustrates how the first order F_2 phase shift in the even echoes can be calculated and removed. As can be seen, the k_x-dependent t_2 delay is bound by 730μs and 110μs with the center of k-space on the red line at 410μs, which are the expected values for N_x=32, t_s = 420μs, and $t_d = \frac{320\mu s}{N_x}$. The values for f_m are centered about water at the green line ± one-half the spectral bandwidth of 1190Hz. The resulting phase correction, $\Delta\phi_{m,n}(k_x, t_2)$ is greatest for k_x points early in the reversed echo and the least for points later in the echo. This corresponds to the earlier points having a greater timing error, and thus, a larger phase shift along F_2 to correct.

Once the even echoes are k_x-reversed and phase corrected using equation 7.11 to account for the k_x-dependent t_2 delay from the reversal, equation 7.9 can be rewritten as:

$$\begin{aligned} phase(S^+(k_x,t_2)) &= reverse(\phi^+(k_x,t_2)) + \Delta\phi_{m,n}(k_x,t_2) + \phi_e(t_2) \\ &= \phi^-(k_x,t_2) + \phi_e(t_2) \\ phase(S^-(k_x,t_2)) &= \phi^-(k_x,t_2) - \phi_e(t_2) \end{aligned} \tag{7.12}$$

where $reverse()$ signifies the reversal of the k_x dimension in each even echo and $\phi_e(t_2)$ is constant with respect to k_x. After reversal and F_2 phase corrections, the (k_x, t_2) encoded spatial signal phase of the even echoes, $\phi(k_x,t_2)$, is in phase with the phase evolution of the odd echoes with only the equal and opposite t_2 dependent eddy current phase difference between them. Therefore, taking the complex mean of adjacent even-odd echoes in the k-space, time domain cancels out the eddy current phase term and adds the echoes in phase [96,124]. This method allows both echoes from the EPI readout to be used and combined as separate averages without increasing the line-width along F_2 by combining them out of phase.

7.3.4 4D INSEP-JRESI Data Processing

Fig. 7.5 shows a flowchart of the full INSEP-JRESI processing pipeline from the initial raw data extraction to a fully processed data set with all phase errors corrected, echoes and channels combined, and any filtering or zero filling applied. As shown, the order of ΔB_0 error corrections must be: (1) $\Delta B_0(t)$ field drift and initial off-resonance removed from the k-space, time domain as discussed in section 7.3.2, (2) $\Delta B_0(x,y,t)$ eddy current and even-odd echo timing errors removed from the k-space, time domain as discussed in section 7.3.3, and (3) $\Delta B_0(x,y)$ and $\Delta\phi^c(x,y)$ corrections applied in the spatial domain using first-point methods from the NWS data.

Any initial off-resonance and $\Delta B_0(t)$ field drift must be removed before the even and odd echoes can be combined to remove eddy current effects in k-space. The even echoes have acquired additional phase evolution from the echo timing delay and off-resonance,

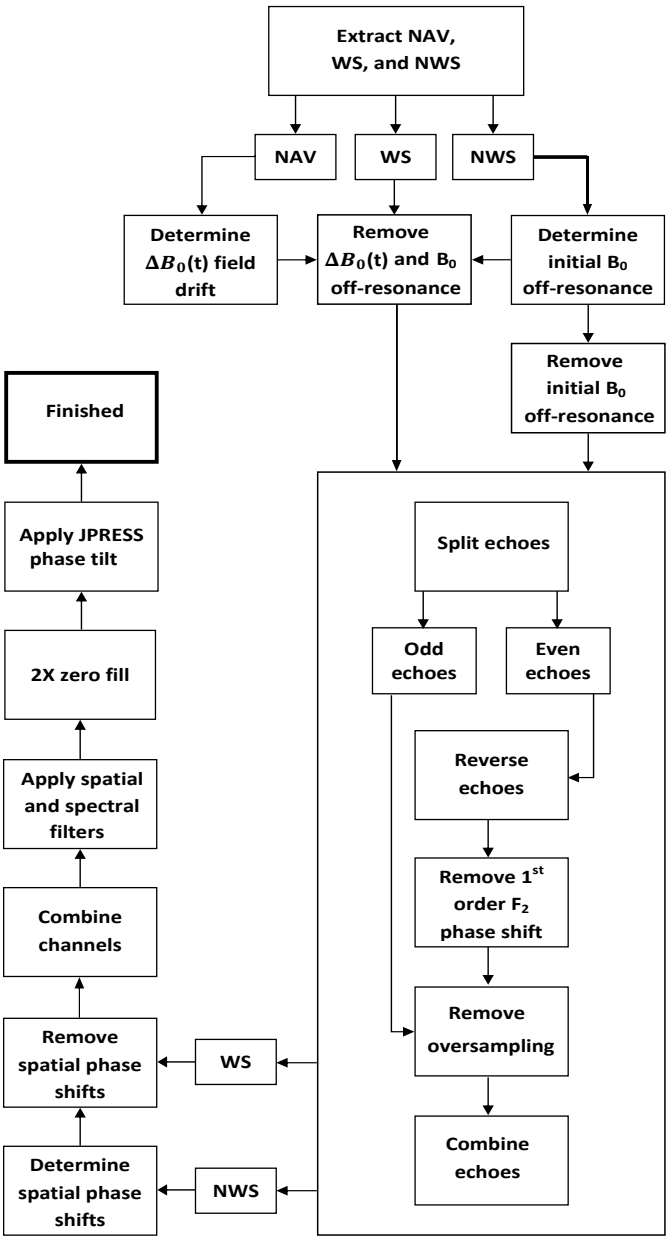

Figure 7.5: Data processing flowchart for 4D INSEP-JRESI data extraction, phase correction, and channel combination.

therefore it must be removed for the echoes to be combined in phase. Additionally, the k_x-dependent, first-order phase correction in equation 7.11 that is applied to F_2 in the even echoes assumes water is on resonance and at the center of the spectral bandwidth in both echoes. $\Delta B_0(x, y, t)$ eddy currents are removed in the k-space, time domain to narrow the PSF of the sequence along the (X, F_2) plane and to remove any effects they

may have on the spatial phase distribution. Lastly, the $\Delta\phi^c(x,y)$ 0^{th} order spatial phase distribution from the phased array coils is removed in the spatial, time domain by first point phase corrections using the NWS data. The NWS data has had any initial $B_0(t)$ off-resonance removed using equation 7.8 and $\Delta B_0(x,y,t)$ eddy currents corrected by taking the complex mean of the even and odd echoes as in section 7.3.3. The phased-array coil channels are then combined in-phase by taking their complex mean in k-space, time. A Hamming filter is applied to k-space to reduce spatial artifacts and the spectral dimensions are apodized using a skewed sine-squared filter with skew parameter 0.5 along t_1 and t_2 to enhance cross peaks and reduce residual water. Optional two-times zero-filling of the spectral dimensions may be applied prior to tilting the JPRESS spectra 45° to account for the maximum echo sampling used during acquisition [108].

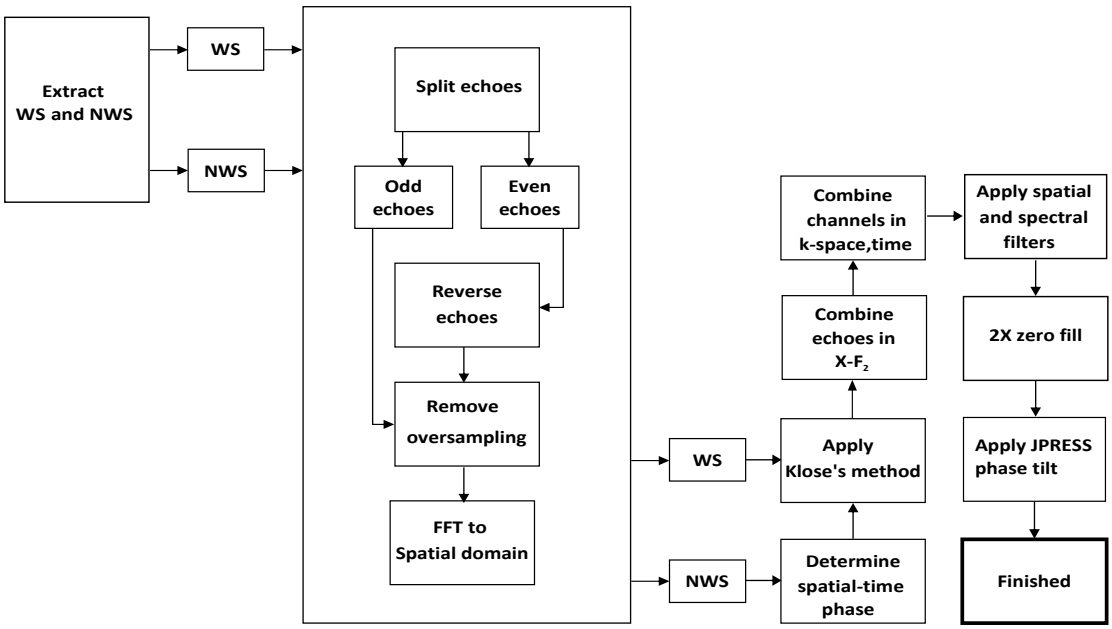

Figure 7.6: Data processing flowchart for Klose's method-based data extraction, phase correction, and channel combination.

Figure 7.6 shows a flowchart of a Klose's method-based post-processing pipeline that is used as a comparison to the INSEP-JRESI post-processing shown in figure 7.5. It uses standard techniques that have all been published in earlier work [78, 98]. As can be seen, the even echoes are reversed and the oversampling is removed from both echoes as in section 7.3.3. The echoes are then FFT'd to the spatial, time domain where

Klose's phase deconvolution is applied using the NWS data as the phase reference. The even and odd echoes are then combined in a mixed-domain, X-F_2, projection space in order to prevent combining the phase misaligned k_x-t_2 planes directly. The channels are then combined in the k-space, time domain and the remaining post-processing steps are identical to those in figure 7.5.

7.4 Results

7.4.1 Gray Matter Brain Phantom Data

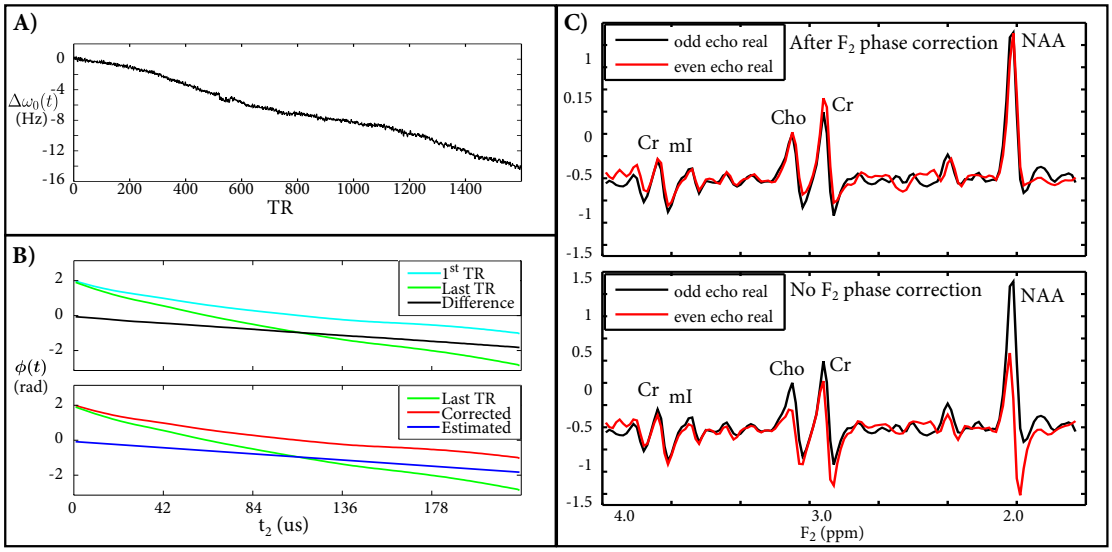

Figure 7.7: Phase corrections for gray matter brain phantom data (A) $\Delta\omega_0(t)$ center frequency drift estimated over 45 minute INSEP-JRESI scan (B) t_2 phase estimates of the 1^{st} and last TR navigators, their difference, the estimated phase correction, and the corrected phase of the last TR navigator (C) Real 1D spectra along F_2 taken from the center of the phantom at $F_1 = 0$Hz after k_x reversal for the even and odd echoes with and without F_2 phase correction.

Results for a representative INSEP-JRESI gray matter brain phantom scan at different steps in the post-processing pipeline are shown in figure 7.7. Part A shows the estimated changes in $\omega_0(t)$ caused by $\Delta B_0(t)$ field drift as calculated by equation 7.7 over the 45 minute acquisition time. As can be seen, the center frequency decreases nearly 16 Hz over the scan duration, which is roughly a 0.1ppm frequency shift along

F_2 that will blur peaks and dephase cross peaks along F_1 by varying the t_1 phase increment. Changes in the k_y phase encoding step-size from $\Delta B_0(t)$ also affect the spatial localization of metabolite peaks along Y. The top of part B in figure 7.7 shows the t_2 phase evolution of the 1^{st} and last interleaved navigator scans and their phase difference. The phase evolutions of the navigator scans demonstrate linear trends over t_2, however, they contain non-linear phase rolls caused by eddy-currents and large offsets from the phased array coils. On the other hand, their difference as calculated by equation 7.5, does not contain these phase rolls nor offsets and is linear over t_2. The bottom pane of figure 7.7B shows the estimated t_2 phase correction calculated using the difference phase in the upper pane, as well as the original and corrected phases of the last TR navigator. As can be seen, the estimated phase drift calculated using the values from equation 7.7 and the navigator sample timing matches the phase difference from the upper pane in figure 7.7B. This phase estimate was used to correct the last TR navigator so that its phase matches the phase of the 1^{st} TR, as shown in the bottom pane of figure 7.7B, including eddy current and phased array coil offsets.

Figure 7.7C shows real 1D F_2 spectra from the same scan used in figures 7.7A and B. They are from the center of the phantom at the F_1=0Hz center diagonal and show spectra from both the odd and k_x-reversed even echoes after the $\Delta B_0(t)$ field drift and off-resonance have been removed, which is the only post-processing that has been applied to the data. The top of the figure shows the spectrum before the k_x-dependent F_2 phase correction from equation 7.11 is applied and the bottom shows the result after it is applied. As can be seen, before the correction many of the metabolite peaks in the real spectrum from the even echo are mixed phase (neither absorptive nor dispersive) and do not match the phases of the odd echo. The phases between the echoes are more dissimilar at peaks further from the center frequency, so that the Cr 3.91ppm peak is nearly in phase between the even-odd echoes, however the NAA 2.0ppm peak in the even echoes is nearly 90° out of phase with the NAA peak in the odd echo. After the F_2 phase correction is applied to the even echoes, the phase of each metabolite peak is more similar to the odd echo peak. The Cr 3.91ppm peak in the even echo is still in phase with the odd echo peak, however, the phase dispersion in the NAA 2.0ppm peak

has been completely removed so that it is almost purely absorptive and matches the phase of the peak in the odd echo. Aligning the phases of the peaks along F_2 in this way will result in taller, narrower peaks further from the center frequency.

Figure 7.8 shows the results from a representative gray matter brain phantom INSEP-JRESI scan that has been fully post-processed using the pipeline shown in figure 7.5 compared to the same scan processed using the Klose's method-based post processing shown in figure 7.6. The top of the figure shows the spatial distribution of the magnitude 1D JPRESS diagonal along F_1=0Hz from 4.5ppm to 1.5ppm over the entire phantom and immediately surrounding voxels. Spectra are shown for the INSEP-JRESI post-processing in red and the Klose's method-based post-processing in black. The bottom of the figure shows 2D JPRESS spectra from the edge and center of the phantom for both post-processing methods. All of the 2D JPRESS spectra are shown using the same contour levels for an accurate comparison.

As can be seen in the top of figure 7.8, the NAA, Glx, Cr, Cho, and mI peaks are well resolved within the 1D JPRESS spectra throughout the spatial distribution of the phantom with partial volume effects reducing the peak amplitudes around the edges for both methods. However, in the Klose's method-based post-processed scans, the peak amplitudes for each metabolite are lower than the INSEP-JRESI processed scan throughout the phantom. The Klose's method-based post-processed data also exhibits more variation in the spatial distribution of metabolite peak amplitudes than INSEP-JRESI. The differences in peak amplitude are greatest away from the center of the phantom where the INSEP-JRESI scan demonstrates the highest peak amplitude increases without also increasing the level of spatial aliasing along the X-Y plane, and in peaks along F_2 that are farthest from the center frequency.

The 2D JPRESS spectra shown in the bottom of figure 7.8 highlight the differences in metabolite peak amplitudes between Klose's method and INSEP-JRESI post-processing at the edges and center of the phantom. As can been seen in figures 7.8B1 and B2, there are only small differences between the spectra processed using the two methods at the center of the phantom. Many of the peak amplitudes and line-widths are similar between the two methods; however, the INSEP-JRESI processed spectrum in B1 has

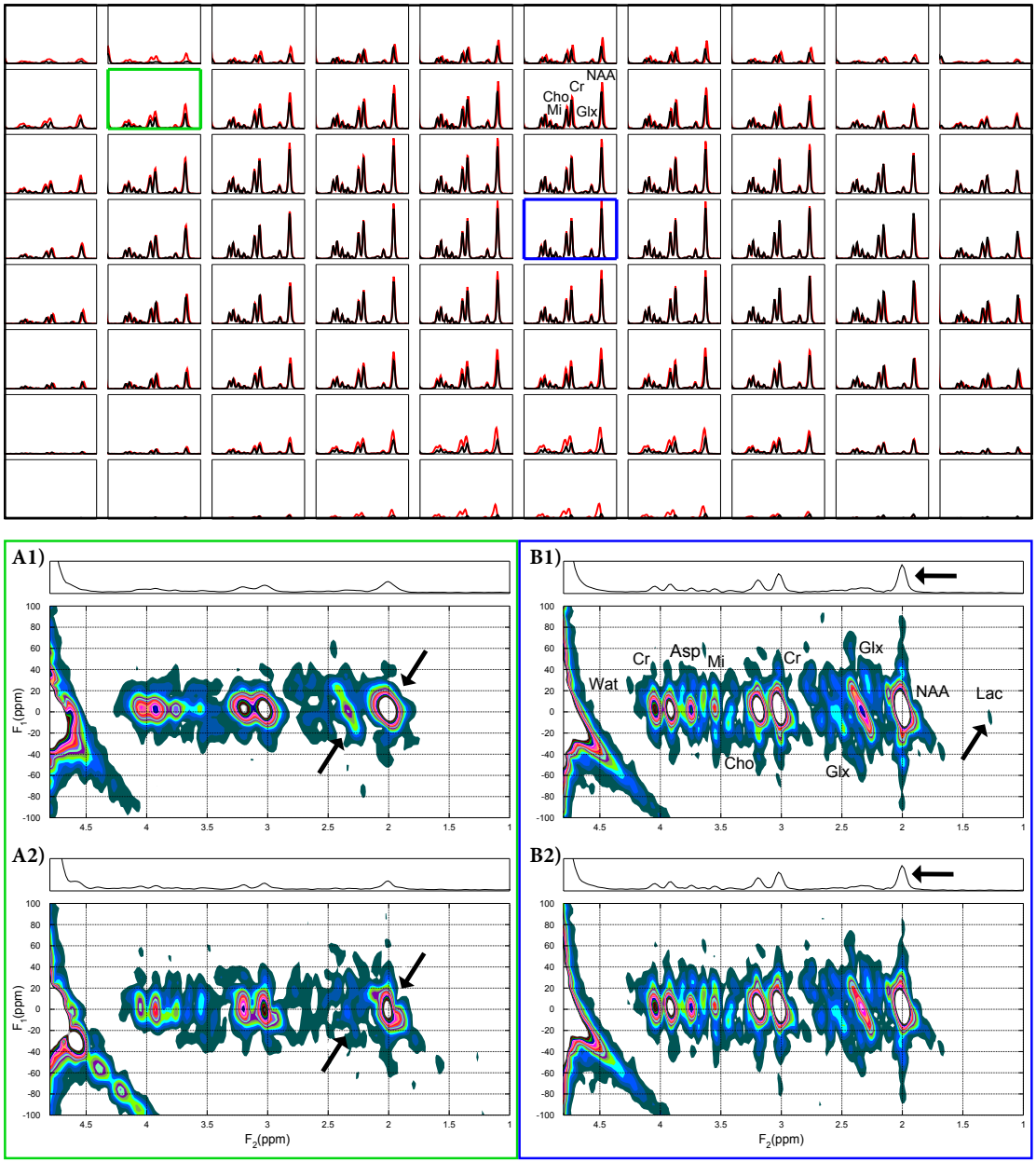

Figure 7.8: Gray matter phantom result comparison between INSEP-JRESI phase corrections and Klose's method-based phase corrections. (top) Spatial distribution of the 1D F_2 spectra taken from the F_1=0 diagonal for INSEP-JRESI corrections in red and Klose's method in black. (A1/B1) INSEP-JRESI corrected JPRESS spectra from the edge and center of phantom. (A2/B2) Klose's method corrected JPRESS spectra from the edge and center of phantom.

higher amplitude Glx and NAA peaks, as well as the Lactate peak at 1.3ppm which is not present in the Klose's method post-processed spectrum. Larger differences between the methods are seen in figures 7.8A1 and A2 taken from the edge of the phantom. It is clear the INSEP-JRESI spectrum in A1 has higher peak amplitudes for each of the metabolites as well as greatly improved peak line-shapes than the Klose's method post-processed spectra. There are peak distortions in A2 along both F_1 and F_2 that are not present in A1, and the Glx and NAA peaks are considerably higher in the INSEP-JRESI spectrum as well.

	Klose's Method Post-Processing					
	Amplitude		**F_1 FWHM**		**F_2 FWHM**	
	mean	CV (%)	mean (Hz)	CV (%)	mean (Hz)	CV (%)
NAA (2.0ppm)	2.669	40.5	6.989	3.97	8.932	36.6
Glx (2.2ppm)	0.434	31.7	**7.205**	15.1	8.749	33.1
Cr (3.0ppm)	2.017	40.4	7.006	5.6	8.716	34.0
Cho (3.2ppm)	1.355	37.1	7.189	13.6	9.596	45.4
mI (3.5ppm)	0.547	33.2	7.238	14.9	9.778	40.7
Cr (3.9ppm)	0.978	39.5	7.172	15.3	9.695	49.2
	INSEP-JRESI Post-Processing					
NAA (2.0ppm)	**2.952**	36.4	**6.973**	0.0	**8.417**	28.4
Glx (2.2ppm)	**0.463**	30.0	7.255	16.3	**8.417**	28.4
Cr (3.0ppm)	**2.098**	37.5	**6.973**	0.0	**8.45**	30.7
Cho (3.2ppm)	**1.413**	31.7	**6.973**	0.0	**9.015**	33.4
mI (3.5ppm)	**0.561**	31.3	**7.006**	5.6	**9.712**	40.5
Cr (3.9ppm)	**0.989**	36.8	**6.989**	4.0	**8.948**	40.4

Table 7.1: Mean and standard deviations of all gray matter phantom scan metabolite peak amplitudes and FWHMs over the ROI shown in figure 7.8. The lowest FWHM and highest amplitude for each metabolite peak are highlighted.

Quantitative differences between the post-processing methods are shown in table 7.1. It contains the mean and coefficient of variance (CV) of the amplitude, F_1 Full Width Half Maximum (FWHM), and F_2 FWHM of the metabolite peaks: NAA (2ppm), Glx (2.2ppm), Cr (3.0ppm), Cho (3.2ppm), mI (3.5ppm), and Cr (3.9ppm), calculated over the 40 internal voxels that were not affected by partial volume effects in the 7 gray matter phantom scans. The largest mean peak amplitude and lowest FWHM along each spectral dimension are highlighted. As can be seen, all but one of the values is from the INSEP-JRESI post-processed phantom scans, which is in agreement with the

qualitative results shown in figure 7.8. The INSEP-JRESI metabolite peak amplitudes are on average 2-10% larger than peaks from the Klose's method post-processed data and the FWHMs are 1-8% smaller. The CVs for the peak amplitudes and FWHMs across both dimensions are all lower for the INSEP-JRESI post-processed data, indicating peak amplitudes and line-shapes that are more consistent throughout the homogeneous phantom than Klose's method. The F_1 FWHMs for the INSEP-JRESI post-processing pipeline are dramatically lower than the values for Klose's method, with many equal to 0, indicating there was no variation in the value over any of the voxels or scans as a result of removing the $\Delta B_0(t)$ field drift.

7.5 Discussion

A new approach to phase error correction has been developed for multi-dimensional MRSI data acquisition that decouples the time, space, and spatio-temporal dependent phase errors and corrects them individually in a multi-step process in the appropriate domain. The INSEP-JRESI pulse sequence presented in section 7.3.1, contains an interleaved water navigator scan to sample the $\Delta B_0(t)$ field drift at every TR. The navigator phase evolution along the t_2 dimension was determined without the influence of eddy current induced phase errors or phased array coil phase offsets by using a modified DORK technique in section 7.3.2 [94]. Eddy current phase errors were removed by exploiting the phase relationship between adjacent even-odd echoes, which required the development of a new k_x-dependent first-order phase correction for the F_2 dimension in the even echoes. The multi-step post-processing pipeline for the new approach was presented in section 7.3.4, which illustrated the order of phase corrections and all other post-processing applied to the INSEP-JRESI data. Results for phantom INSEP-JRESI scan phase correction were compared against a standard Klose's method-based technique described in section 7.3.4, which showed the new technique resulted in higher metabolite peak amplitudes without an increase in the noise floor, a more even distribution of metabolite peaks throughout the homogeneous phantom, and drastically improved line-shapes in voxels near the edges of the phantom.

The results shown at various steps of the post-processing pipeline in figure 7.7 show that the $\Delta B_0(t)$ field drift estimates can be accurately decoupled and removed from the interleaved navigator scans, and that the k_x-dependent F_2 phase correction applied to the even echoes shows greatly improved phasing of metabolite peaks away from the center frequency without disturbing peaks close to the center. By removing the linear phase evolution along F_2 caused by the k_x-reversal of the even echoes, NAA, Glx, and other metabolites far from the center frequency can be combined as narrow absorptive peaks, rather than wide dispersive or mixed-phase peaks. Therefore, when the complex mean of the even and odd echoes is taken to remove the eddy-current phase evolution across t_2, an additional benefit is the increased amplitude of spectral peaks further from the center frequency than in Klose's method of eddy current deconvolution, which does not correct the phase of even echoes across F_2.

The phantom results shown in figure 7.7 and table 7.1 demonstrate the effectiveness of the new post-processing approach compared to Klose's method post-processing techniques. Removing the $\Delta B_0(t)$ field drift helped to improve line-shapes and narrow line-widths across F_1, as can be seen in the spectra shown in figure 7.7 and demonstrated by the lower means and CVs of the F_1 FWHM compared to Klose's method in table 7.1. Correcting the field drift also improved the spatial localization along Y by correcting the k_y phase increment at each TR so that it was uniform in the INSEP-JRESI results. The uneven peak distribution along Y in figure 7.7 for the Klose's method processed data even though the phantom is homogeneous in composition demonstrates the effect uncorrected $\Delta B_0(t)$ field drift can have on Y. Correcting the F_2 phase and then taking the complex mean of the even and odd echoes removed $\Delta B_0(x, y, t)$ eddy currents as demonstrated in figure 7.7 by the improved line-shapes across F_2 for voxels that were further from the center of the phantom along X. Additionally, increased peak amplitudes caused by the F_2 rephasing in INSEP-JRESI post-processing are evident in the top of figure 7.7 and in the increased mean peak amplitudes in table 7.1. The low CVs for the FWHM and peak amplitude values in table 7.1 show that the distribution of peak energy within the 4D volume is more even across the phantom for the INSEP-JRESI post-processing method versus Klose's method. Figure 7.7 shows much more variation

along both X and Y in peak amplitudes for Klose's method versus INSEP-COSI, as well as inconsistent peak line-shapes across the ROI. A contributing factor to Klose's method having higher CVs for many of the values in table 7.1 was the increased peak distortions further from the center of the phantom than INSEP-COSI as shown in figure 7.7.

The INSEP-JRESI pulse sequence uses an excite-acquire FID excitation for the interleaved water navigator scan that is not spatially localized. Previous work has used an EPI-based readout to integrate the NWS and navigator scans within each TR [39]; however, imposing spatial constrains on the navigator scan may require a much higher readout bandwidth than is necessary to sample the $\Delta B_0(t)$ phase at each TR. The FID readout bandwidth can be easily decreased in order to increase the navigator SNR without having to consider reductions in the spatial bandwidth and aliasing. This increased SNR allows for more accurate measurements of the $\Delta B_0(t)$ field drift to be made without increasing the water excitation flip angle and affecting the metabolite SNR of the next TR. EPI-based readouts are compatible with the field drift estimation technique described in section 7.3.2 because any EPI-based eddy currents or k_x spatial phase modulation will be removed from the $\Delta B_0(t)$ field estimates by the TR reference phase. Therefore, incorporating spatial localization into the navigator scan to accommodate motion correction and local field changes from susceptibility are possible, but the decision was made to use an FID acquisition for this manuscript in order to maximize SNR. Alternative implementations of the interleaved navigator scan that incorporate spatial information and can address local changes to the field strength are topics of future work.

The EPI eddy current model in this work has been successfully used to remove eddy currents from previous fast multi-echo MRI pulse sequences through even-odd echo cancellation [63, 96, 124]. However, any residual eddy currents as a result of the crusher gradients in the EP-JRESI excitation are not removed by the echo cancellation and may affect the X-F_2 plane of the 4D volume. Efforts were made in the development of the INSEP-JRESI pulse sequence to reduce these eddy currents as much as possible, but further work is required to model their effects and ensure they are removed from the data. They do not appear to be adversely affecting the INSEP-JRESI results, so

it is safe to assume their effects are minimal. As the t_1 increment is increased over the duration of the scan and the EPI readout is pushed further and further away from the initial EP-JRESI excitation, any effects from these eddy current will be reduced as they have more time to dissipate over the increment. One of the strengths of Klose's method is its ability to model the EPI eddy currents along t_2 at each sample point, however, because the NWS is taken at the first t_1 increment, it does not properly model the crusher gradient eddy currents at later t_1s. In fact, at higher t_1 increments, the eddy current deconvolution in Klose's method will actually inject more phase dispersion into the data set because the model incorporates the crusher gradient eddy currents from the first t_1 which are much larger than in later t_1s. An accurate eddy current model using Klose's deconvolution must sample the k_x-t_2 phase at every t_1 increment, not just the first; however, this would double the scan time if implemented.

The use of INSEP-JRESI post processing in the brain *in vivo* is an on-going topic of research and will be the subject of future articles. Preliminary results are promising, however, fat contamination from the skull marrow continues to be problematic in the water and metabolite scans. The fat saturation and dephasing modules used in the slice-based INSEP-JRESI pulse sequence combined with OVS bands are unable to consistently suppress the fat to levels acceptable for clinical use. The field drift estimates from a fat contaminated navigator scan are still accurate for low levels of fat contamination because it is removed by the difference phase between TRs; however, the levels of fat contamination from the sliced-based localization are too great for phase estimates to be accurate. Using volumetric localization could reduce the fat contamination to acceptable levels by allowing a VOI to be chosen that does not excite the fat, however, this will reduce the spatial extent of the imaged region.

7.6 Conclusion

This works demonstrates how to decouple the numerous phase errors from a multi-dimensional MRSI acquisition and to correct them in the appropriate domain. The INSEP-JRESI pulse sequence was presented that acquires an interleaved navigator wa-

ter scan at each TR in order to estimate field drift. Methods were presented for isolating and estimating the field drift, as well as correcting the even-odd echo phase differences inherent in an EPI-based readout. Eddy currents were removed by even-odd echo cancellation in k-space, which differs from Klose's method in the spatial domain. Phantom results comparing the INSEP-COSI post-processing pipeline to Klose's method-based post-processing showed increased peak amplitudes for each metabolite in all voxels across both the X and Y dimensions, as well as improved spatial peak distributions and line-shapes across the ROI. These results show that INSEP-COSI is a viable alternative to Klose's method of phase correction of MRSI data and that it is possible to correct the phase errors within the domain in which they occur. Further work is required to optimize the INSEP-JRESI navigator scan parameters and to improve the fat suppression techniques for slice-based localization. Future articles may address alternative spatially localized navigator scans that can for correct patient motion as well as field drift.

CHAPTER 8

Conclusions

This dissertation has demonstrated the successful implementation of the two main goals presented at the end of section 1.4 as well as their constituent components.

The 2D Poisson-gap mask algorithm and *best mask* empirical heuristic were described in sections 3.5 and 3.5.2, and demonstrated stochastic NUS mask creation for MRSI data that could be modulated by the MR time-domain signal envelope. The viability of the approach was shown by the mask PSFs with a single dominant central peak and small side-lobes surrounded by low amplitude, broadband noise as well as by the successful reconstruction of 2D Poisson-gap under-sampled data sets throughout the rest of the dissertation.

As described in chapter 4, the Cambridge algorithm was successfully implemented from partially documented sources and optimized to reconstruct multi-dimensional spectroscopic data. It was modified to solve both the MaxEnt and CS problems so they could be compared without solver bias in chapter 5. Prospectively and retrospectively 4X under-sampled *in vivo* breast data was reconstructed by MaxEnt and CS in chapter 5, and showed that MaxEnt reconstruction resulted in superior reconstructions. Additionally, quantitative metrics taken over under-sampled and reconstructed simulated data sets showed that MaxEnt reconstruction resulted in less metabolite peak non-linearity than CS. The results in chapter 5 showed that a clinically acceptable 5 minute EP-COSI breast scan was possible using NUS and non-linear reconstruction.

The GS reconstruction problem of 4D MRSI data was defined in chapter 6 and a derivation for the solution was shown within the Split-Bregman iterative framework. This work showed that Split-Bregman based GS reconstruction with 50% overlapping

groups demonstrated the best metabolite peak reproduction, lowest mean metabolite peak RMSEs, and best denoising characteristics of the iterative reconstruction methods tested at 2X-10X NUS on both gray matter brain phantom and *in vivo* brain data.

Lastly, chapter 7 showed the INSEP-JRESI pulse sequence which was developed to sample the $\Delta B_0(t)$ field drift at each TR. The spatio-temporal phase error theory was developed that allowed for the various sources of acquisition error to be characterized, modeled, and removed in the pipeline shown in section 7.3.4. Gray matter brain phantom results for the new post-processing pipeline were compared against Klose's method-based post-processing and showed improved SNR throughout the ROI, spectral line-shapes, and a more even distribution of metabolite peak energy throughout the homogeneous phantom. Further work is required to apply the new techniques to slice-based *in vivo* acquisitions because of fat contamination, however, volumetric localization does not suffer from the same degree of fat contamination and preliminary results are promising.

8.1 Future Work and Recommendations

8.1.1 2D Poisson Gap Under-Sampling

1. The 2D Poisson-gap sample mask creation is a stochastic process that will not produce the same mask given the same set of parameters. This makes it difficult to optimize the mask to specific post-processing spectral filters and time-domain signal envelopes. The current EP-COSI and EP-JRESI t_1 modulations functions are merely approximations to these constraints. Therefore, deterministic sample mask creation should be investigated that creates masks that satisfy the Restricted Isometry Property and mutual incoherence required of a sampling mask. Having a deterministic function calculate the sample positions within the mask will make it much simpler to optimize the sampling patterns in order to maximize reconstruction SNR or reduce non-linearity.

2. Because the reconstructions are non-linear, the ratio's between metabolite peaks

may change as a result of the reconstruction. The relationships of the NUS rate, sampling distribution, and SNR to the reconstruction non-linearity should be performed with the ultimate goal of fitting the reconstructed spectra in Profit and LCModel for quantitation.

3. Preliminary work extending 2D Poisson-gap sample mask creation to under-sampled 5D data sets (3 spatial + 2 spectral) has been completed, however, the nature of the PSF and sampling artifacts have not been fully explored. This work should continue.

8.1.2 MaxEnt Reconstruction

1. Because the objective function of the MaxEnt problem is a separable problem (i.e., the entropy is calculated over each point individually), most of the operations can be parallelized because the calculations are mostly separate from each other. By parallelizing the Cambridge algorithm, significant increases in the convergence rate can be realized.

2. The Cambridge algorithm is phase sensitive so the phase information of sampled data during the reconstruction should be conserved. However, a study on the effect the algorithm has on the phase of the reconstruction should be made to determine if phase is conserved or destroyed.

3. The non-linearity of the reconstructed peaks has not been fully explored and should be studied in order to determine if accurate quantitation is possible. The effect of the *def* and C_0 parameters that are calculated from the sampled data's noise distribution may play a role in the non-linearity of the reconstruction. These parameters should be modified in any study of metabolite peak non-linearity.

4. While not covered in this dissertation, the current implementation of the Cambridge algorithm can reconstruction 5D data sets (3 spatial + 2 spectral) and research into the effect of under-sampling a second spatial dimension on the reconstruction should be explored. The mixed-domain k_y-t_1 plane of multi-dimensional

MRSI are is sparse, but because the spatial domains are non-sparse in MRSI, the sparsity of the mixed-domain k_y-k_z-t_1 volume may be insufficient to produce acceptable reconstructions. Therefore, 5D MaxEnt reconstruction using some transform domain in the spatial dimension should be explored.

8.1.3 Group Sparse Reconstruction

1. The Split-Bregman based GS reconstruction implementation has many operations that can be parallelized because they occur over individual groups of points. Even though they overlap, they are stored separately in memory and calculations for these groups can be distributed over a cluster.

2. The current implementation of the **G** and textbfG' functions in the GS pseudocode loop over the groups stored in a cell array, which is a time intensive process and is by far where most of the computation time is spent. Because the groups are equal sized in the current implementation, it may be possible to use a more clever indexing scheme that defines a vector of indices into the cell array and pulls out the grouping indices into the 4D volume. Matlab is very slow at for loops, so if a clever indexing strategy can not be implemented, then a parallelizing parfor loop would definitely speed up this process.

3. The current implementation is limited to equal sized groups because the left hand side of the u^{k+1} subproblem is circular and can be inverted using the Fourier transform. This occurs when G is a multiple of the identity matrix. If groups were different sizes and each point was not in the same number of groups, G is still diagonal however each diagonal is the number of groups that contain the point corresponding to the diagonal. Equation 6.17 describes the point in the code where this requirement can be changed. Each point being in a different number of groups would allow various grouping distributions to be tried other than a uniform distribution, which is essentially what is used in the current implementation. For example, a higher density of groupings or more overlap could be enforced over spectral regions, while less overlap and less group density could be enforced over

noise and artifact regions.

4. Even if different sized groupings or non-uniform distributions are used, the optimal size and overlapping percentage need to be determined for different experimental conditions. Empirically, it was found that the optimal group sizes are on the order of the features being reconstructed or slightly smaller. Therefore, the linewidth of the spectra should be a factor used in any heuristic to determine the optimal grouping strategy.

5. A phase sensitive variant of GS reconstruction should be implemented that takes into account the phase of each point during the reconstruction. There are open questions regarding the conservation of phase during the reconstruction because the group-wise shrink is performed in magnitude mode and the phase information is lost. Phase information is retained by the fidelity constraint, but this may be insufficient. A phase sensitive reconstruction would reconstruct the real and imaginary channels separately so the memory requirements would be quite high.

6. GS reconstruction is well suited for the joint sparsity problem in multi-channel reconstruction. The jointly sparse points across each channel could theoretically be grouped and reconstructed together rather than reconstructing each channel individually , as is currently done.

8.1.4 INSEP-JRESI and Spatio-temporal Phase Corrections

1. Fat suppression for slice-based *in vivo* brain scans in both the metabolite, NWS, and navigator was scans needs to be addressed. Current methods do not suppress the fat sufficiently, so the phase error estimates are compromised.

2. One possible remedy is to remove the residual fat from the NWS and navigator scans in post-processing.

3. The nature of crusher eddy currents that are not removed during post-processing need to be explored and means to remove or reduce them should be implemented.

4. The initial off-resonance is currently estimated using the center of k-space in the NWS scan and alternative methods should be investigated.

5. Spatial localization should be added to the navigators so that patient motion, susceptibility changes, and other forms of local field changes can be modeled and removed in post-processing.

8.1.5 Miscellaneous

1. The new INSEP-JRESI-based post-processing method should be combined with NUS reconstruction. Because most of the rephasing occurs in the sample domain, each channel can be reconstructed with only the phase error of phased-array coils present. The multi-channel GS reconstruction could be implemented in such a way that each channel is rephased in the spatial domain at each iteration. However, there are stability concerns given that there will be spatial artifacts present in the earlier iterations.

2. The 90° refocusing pulse in EP-COSI is not giving any where near its theoretical coherence transfer efficiency so the cross peaks are being degraded. This is preventing high spatial resolutions to be achieved in the brain and other not-fatty tissues. The pulse's phase evolution needs to be investigated to determine how this affects the coherence transfer efficiency. Other pulse types should be investigated as well.

References

[1] A. Abragam, *Principles of Nuclear Magnetism.* Oxford University Press, 1983.

[2] W. Aue, E. Bartholdi, and R. Ernst, "Two-dimensional spectroscopy. application to nuclear magnetic resonance," *J. Chem. Phys.*, vol. 64, pp. 2229–2246, 1976.

[3] J. Barna, E. Laue, M. Mayger, J. Skilling, and S. Worrall, "Exponential sampling, an alternative method for sampling in two-dimensional nmr experiments," *JMR*, vol. 73, pp. 69–77, 1987.

[4] R. Bartha, D. Drost, R. Menon, and P. Williamson, "Spectroscopic lineshape correction by quecc: Combined deconvolution and eddy current correction," *MRM*, vol. 44, pp. 641–645, 2000.

[5] P. Basser, S. Pajevic, C. Pierpaoli, J. Duda, and A. Aldroubi, "in vivo fiber tractography using dt-mri data," *Magn. Reson. Med.*, vol. 44, pp. 625–632, 2000.

[6] P. Basser and C. Pierpaoli, "Microstructural and physiological features of tissues elucidated by quantitative-diffusion-tensor mri," *J. Magn. Reson.*, vol. 213, pp. 560–570, 2011.

[7] J. Begley, T. Redpath, P. Bolan, and F. Gilbert, "In vivo proton magnetic resonance spectroscopy of breast cancer: a review of the literature," *Breast Cancer. Res.*, vol. 14, p. 207, 2012.

[8] A. L. Berger, V. J. D. Pietra, and S. A. D. Pietra, "A maximum entropy approach to natural language processing," *Comput. Linguist.*, vol. 22, pp. 39–71, 1996.

[9] M. Bernstein, K. King, and X. Zhou, *Handbook of MRI Pulse Sequences.* Elsevier, 2004.

[10] D. Bertsekas, "Multiplier methods: A survey," *Automatica*, vol. 12, pp. 133–145, 1976.

[11] F. Beutler, "Error-free recovery of signals from irregularly spaced samples," *SIAM*, vol. 8, pp. 328–335, 1966.

[12] ——, "Alias-free randomly timed sampling of stochastic processes," *IEEE Trans. Inf. Th.*, vol. IT-16, pp. 147–152, 1970.

[13] B. Biswal, F. Yetlin, V. Haughton, and J. Hyde, "Functional connectivity in the motor cortex of resting human brain using echo-planar mri," *Magn. Reson. Med.*, vol. 34, pp. 537–541, 2005.

[14] K. Block, M. Uecker, and J. Frahm, "Undersampled radial mri with multiple coils. iterative image reconstruction using a total varation constraint," *Magn. Reson. Med.*, vol. 57, pp. 1086–1098, 2007.

[15] S. Boyd. (2013) Cvx: a matlab-based convex modeling framework. [Online]. Available: http://cvxr.com/

[16] S. Boyd and L. Vandenberghe, *Convex Optimization.* Cambridge Univ. Press, 2004.

[17] S. Burch, S. Gull, and J. Skilling, "Image restoration by a powerful maximum entropy method," *Com. Vision, Grap. and Im. Proc.*, vol. 23, pp. 113–128, 1983.

[18] J. Burg, "Maximum entropy spectral analysis," in *Presented at 37th Annual Society of Exploration Geophysics Meeting*, 1967.

[19] B. Burns, N. Wilson, J. Furuyama, and M. Thomas, "Non-uniformly undersampled multidimensional spectroscopic imaging in vivo: Maximum entropy versus compressed sensing reconstruction," *NMR in BioMed*, vol. 27, 2013.

[20] E. Candés, "Compressive sampling," in *Proceedings of the International Congress of Mathematicians*, 2006, pp. 1433–1452.

[21] ——, "Stable signal recovery from incomplete and inaccurate measurements," *Comm. Pure App. Math.*, vol. 59, pp. 1207–1223, 2006.

[22] E. Candés and J. Romberg. (2013) l_1-magic: A collection of matlab routines for solving the convexoptimization programs central to compressive sampling. [Online]. Available: www.acm.caltech.edu/l1magic/

[23] E. Candés, J. Romberg, and T. Tao, "Robust uncertainty principles: Exact signal reconstruction from highly incomplete frequency information," *IEEE Trans. Info. Theory.*, vol. 52, pp. 489–509, 2006.

[24] E. Candés, M. Wakin, and S. Boyd, "Enhancing sparsity by reweighted l_1 minimization," *J. Fourier Anal. Appl*, vol. 14, pp. 877–905, 2008.

[25] P. Caravan, J. Ellison, T. McMurray, and R. Lauffer, "Gadolinium (iii) chelates as mri contrst agents: structure, dynamics, and applications," *Chem. Rev.*, vol. 99, pp. 2293–2352, 1999.

[26] P. Chen and I. Selesnick, "Overlapping group shrinkage/thresholding and denoising," Polytechnic Institue of New York University, Tech. Rep., 2012.

[27] S. Chen, D. Donoho, and M. Saunders, "Atomic decomposition by basis pursuit," *SIAM*, vol. 20, pp. 33–61, 1999.

[28] ——, "Atomic decomposition by basis pursuit," *SIAM L. Sci. Comp.*, vol. 20, pp. 33–61, 1998.

[29] R. Constable and R. Henkelman, "Why mem does not work in mr image reconstruction," *Magn. Reson. Med.*, vol. 14, pp. 12–25, 1990.

[30] R. Cook, "Stochastic sampling in computer graphics," *ACM Trans. Graph.*, vol. 5, pp. 51–72, 1986.

[31] G. Daniell and P. Hore, "Maximum entropy and nmr: A new approach," *J. Magn. Reson.*, vol. 4, pp. 515–536, 1989.

[32] R. de Graaf, *in vivo NMR Spectroscopy*. Wiley, 2007.

[33] L. Devroye, *Non-Uniform Random Variate Generation*. Springer-Verlag, 1986.

[34] M. Dippe and E. Wold, "Antialiasing through stochastic sampling," *ACM SIGGRAPH Computer Graphics*, vol. 19, pp. 69–78, 1985.

[35] ——, "Antialiasing through stochastic sampling," *ACM*, vol. 19, pp. 69–78, 1985.

[36] D. Donoho, "Compressed sensing," *IEEE Trans. Info. Theory.*, vol. 52, pp. 1289–1306, 2006.

[37] ——, "For most large underdetermined systems of linear equations the minimal ℓ_1-norm solution is also the sparsest solution," *Comm. Pure App. Math.*, vol. 59, pp. 797–829, 2006.

[38] E. Durand, P. van de Moortele, M. Pachot-Clouard, and D. L. Bihan, "Artifact due to b_0 fluctuations in fmri: Correction using k-space central line," *MRM*, vol. 46, pp. 198–201, 2011.

[39] A. Ebel and A. Maudsley, "Detection and correction of frequency instabilities for volumetric ^{1}h echo-planar spectroscopic imaging," *MRM*, vol. 53, pp. 465–469, 2005.

[40] M. Eddy, D. Ruben, R. Griffin, and J. Herzfeld, "Deterministic schedules for robust and reproducible non-uniform sampling in multidimensional nmr," *J. Magn. Reson.*, vol. 214, pp. 296–301, 2012.

[41] Y. Eldar, P. Kuppinger, and H. Bölcskei, "Block-sparse signals: Uncertainty relations and efficient recovery," *IEEE Trans. Sig. Proc.*, vol. 58, pp. 3042–3054, 2010.

[42] Y. Eldar and M. Mishali, "Robust recovery of signals from a structured union of subspaces," *IEEE Trans. Info. Theory.*, vol. 12, pp. 5302–5316, 1980.

[43] M. Figueiredo, R. Nowak, and S. Wright, "Gradient projection for sparse reconstruction: Application to compressed sensing and other inverse problems," *IEEE J. Sel. Topics. Sig. Proc.*, vol. 1, pp. 586–597, 2007.

[44] D. Firmin, G. Nayler, R. Klipstein, S. Underwood, R. Rees, and D. Longmore, "in vivo validation of mr velocity imaging," *J. Comp. Assis. Tomo.*, vol. 11, pp. 751–756, 1987.

[45] B. Foerster, D. Tomasi, and E. Caparelli, "Magnetic field shift due to mechanical vibration in functional magnetic resonance imaging," *MRM*, vol. 54, pp. 1261–1267, 2005.

[46] B. R. Frieden, "Restoring with maximum likelihood and maximum entropy," *J. Opt. Soc. Am.*, vol. 62, no. 4, pp. 511–518, 1972.

[47] B. R. Friedman, "Restoring with maximum liklihood and maximum entropy," *J. Optical Soc. Am.*, vol. 62, pp. 511–518, 1972.

[48] ——, "Statistical models for the image restoration problem," *Comp. Graph. and Imag. Proc.*, vol. 12, pp. 40–59, 1980.

[49] ——, "Unified theory for estimating frequency-of-occurrence laws and optical objects," *J. Opt. Soc. Am.*, vol. 73, pp. 927–938, 1983.

[50] J. Furuyama, N. Wilson, B. Burns, R. Nagarajan, D. Margolis, and M. Thomas, "Application of cs to multidimensional spectroscopic imaging in human prostate," *Magn. Reson. Med.*, vol. 67, pp. 1499–1505, 2012.

[51] U. Gamper, P. Boesiger, and S. Kozerke, "Compressed sensing in dynamic mri," *Magn. Reson. Med.*, vol. 59, pp. 365–373, 2008.

[52] A. Gilbert, S. Guha, P. Indyk, S. Muthukrishnan, and M. Strauss, "Near-optimal sparse fourier representations via sampling," in *Annual ACM Symposium on Theory of Computing*, vol. 34, 2002, pp. 152–161.

[53] G. Glover and N. Pelc, "A rapid-gated cine mri technique," *Magn. Reson. Annual*, pp. 299–333, 1988.

[54] E. Glunde, Z. Bhujwalla, and S. Ronen, "Choline metabolism in malignant transformation," *Nat Rev Cancer*, vol. 11, pp. 835–848, 2011.

[55] T. Goldstein and S. Osher, "The split bregman method for l1-regularized problems," *SIAM J. Imaging Sci.*, vol. 2, pp. 323–343, 2009.

[56] V. Govindaraju, K. Young, and A. Maudsley, "Proton nmr chemical shifts and coupling constants for brain metabolites," *NMR in Biomed*, vol. 13, pp. 129–153, 2000.

[57] S. Gull and G. Daniell, "Image reconstruction from incomplete and noisy data," *Nature*, vol. 272, pp. 686–690, 1978.

[58] R. Hamming, *Digital Filters*. Prentice-Hall, 1989.

[59] J. Hoch, "Maximum entropy signal processing of two-dimensional nmr data," *J Magn. Reson*, vol. 64, pp. 436–440, 1985.

[60] J. Hoch, A. Stern, D. Donoho, and I. Johnstone, "Maximum entropy reconstruction of complex (phase sensitive) spectra," *JMR*, vol. 86, pp. 236–246, 1990.

[61] J. Hoch and A. Stern, *NMR Data Processing*. Wiley, 1996.

[62] S. Hu, M. Lustig, A. Chen, J. Crane, A. Kerr, D. Kelley, R. Hurd, J. Kurhanewicz, S. Nelson, J. Pauly, and D. Vigneron, "Compressed sensing for resolution enhancement of hyperpolarized 13c flyback 3d-mrsi," *J Magn. Reson*, vol. 192, pp. 258–264, 2008.

[63] X. Hu and T. Le, "Artifact reduction in epi with phase-encoded reference scan," *MRM*, vol. 36, pp. 16–171, 1996.

[64] J. Huang and T. Zhang, "The benefit of group sparsity," *Annals of Statist.*, vol. 38, pp. 1978–2000, 2010.

[65] S. Hyberts, K. Takeuchi, and G. Wagner, "Poisson-gap sampling and forward maximum entropy reconstruction for enhancing the resolution and senstivity of protein nmr," *J. Am. Chem. Soc.*, vol. 132, pp. 2145–2147, 2010.

[66] A. Jain, *Fundamentals of Digital Image Processing*. Prentice Hall, 1989.

[67] E. T. Jaynes, "Information theory and statistical mechanics i," *Phy. Review*, vol. 106, pp. 620–630, 1957.

[68] ——, "Information theory and statistical mechanics ii," *Phy Review*, vol. 108, pp. 171–190, 1957.

[69] ——, "Prior probabilities," *IEEE Trans. on Sys. Sci. and Cyber.*, vol. 4, pp. 227–241, 1968.

[70] P. Jezzard and R. Balaban, "Correction for geometric distortions in echo planar images from b_0 field variations," *MRM*, vol. 34, pp. 65–73, 1995.

[71] P. Jezzard, A. Barnett, and C. Pierpaoli, "Characterization of and correction for eddy current artifacts in echo planar diffusion imaging," *MRM*, vol. 39, pp. 801–812, 1998.

[72] S. Kim, K. Koh, M. Lustig, S. Boyd, and D. Gorinevsky, "An interior-point method for large-scale l_1-regularized least squares," *IEEE J. Sel. Topics. Sig. Proc.*, vol. 1, pp. 606–617, 2007.

[73] U. Klose, "In vivo proton spectroscopy in presence of eddy currents," *Magn. Reson. Med.*, vol. 14, pp. 26–30, 1990.

[74] T. Lange, M. Zaisev, and M. Buechert, "Correction of frequency drifts induced by gradient heating in ^{1}h spectra using interleaved reference spectroscopy," *JMRI*, vol. 33, pp. 748–754, 2011.

[75] E. Laue, M. Mayger, J. Skilling, and J. Staunton, "Reconstruction of phase-sensitive 2d nmr spectra by maximum entropy," *JMR*, vol. 68, pp. 14–29, 1986.

[76] G. Lenz, E. Haacke, and R. White, "Retrospective cardiac gating: a review of technical aspects and future directions," *Magn. Reson. Imag.*, vol. 7, pp. 445–455, 1989.

[77] S. Lipnick, X. Liu, J. Sayre, L. Bassett, N. DeBruhl, and M. Thomas, "Combined dce-mri and single-voxel 2d mrs for differentiation between benign and malignant breast lesions," *NMR in Biomed.*, vol. 8, pp. 922–930, 2010.

[78] S. Lipnick, G. Verma, S. Ramadan, J. Furuyama, and M. Thomas, "Ep-cosi: implementation and pilot evaluation in human calf in vivo," *Magn. Reson. Med.*, vol. 64, pp. 947–956, 2010.

[79] M. Lustig, D. Donoho, and J. Pauly, "Sparse mri: The application of compressed sensing for rapid mr imaging," *Magn. Reson. Med.*, vol. 58, pp. 1182–1195, 2007.

[80] M. Lustig, D. Donoho, J. Santos, and J. Pauly, "Compressing sensing mri," *IEEE Signal Process. Mag.*, vol. 25, pp. 72–82, 2008.

[81] M. Maciejewski, M. Medhi, A. schuyler, A. Stern, and J. Hoch, "Data sampling in multidimensional nmr: Fundamentals and strategies," *Top Curr. Chem.*, vol. 316, pp. 49–77, 2012.

[82] P. Mansfield, "Spatial mapping of the chemical shift in nmr," *J. Phys. D. Appl. Phys*, vol. 16, pp. L235–L238, 1983.

[83] ——, "Spatial mapping of the chemical shift in nmr," *Magn. Reson. Med.*, vol. 1, pp. 370–386, 1984.

[84] G. Marseille, R. D. Beer, M. Fuderer, A. Mehlkopf, and D. van Ormondt, "Nonuniform phase-encode distributions for mri scan time reduction," *J. Magn. Reson. Series B*, vol. 111, pp. 70–75, 1996.

[85] M. Mobli and J. Hoch, "Maximum entropy spectral reconstruction of nonuniformly sampled data," *Concepts Mag. Res.*, vol. 32A, pp. 436–448, 2006.

[86] R. Mulkern and L. Panych, "Echo planar spectroscopic imaging," *Concepts. Magn. Reson.*, vol. 13, pp. 213–237, 2001.

[87] R. Mulkern, S. Wong, C. Winalski, and F. Jolesz, "Contrast manipulation and artifact assessment of 2d and 3d rare sequences," *Magn. Reson. Imag.*, vol. 8, pp. 557–566, 1990.

[88] R. Nagarajan, J. Furuyama, D. Margolis, S. Raman, M. Sarma, and M. Thomas, "Echo planar based j resolved and correlated spectroscopic imaging of human prostate using external coil," in *Proceedings of the 2011 ISMRM*, 2011, p. 2801.

[89] W. Negendank, "Studies of human tumors by mrs: a review," *NMR in Biomed.*, vol. 5, pp. 303–324, 1992.

[90] S. Ogawa, D. Tank, R. Menon, J. Ellermann, S. Kim, H. Merkle, and K. Ugurbil, "Intrinsic signal changes accompanying sensory stimulation: functional brain mapping with magnetic resonance imaging," *PNAS*, vol. 89, pp. 5951–5955, 1992.

[91] R. Ogg, P. Kingsley, and J. Taylor, "Wet, a t1 and b1 insensitive water-suppression method for in vivo localized 1h nmr spectroscopy," *J Magn. Reson. B*, vol. 104, pp. 1–10, 1994.

[92] S. Osher, M. Burger, D. Goldfarb, J. Xu, and W. Yin, "An iterative regularization method for total variation-based image restoration," *Multiscale Model Simul.*, vol. 4, pp. 460–489, 2005.

[93] N. Pelc, R. Herfkens, A. Shimakawa, and D. Enzmann, "Phase contrast cine magnetic resonance imaging," *Magn. Reson. Quarterly*, vol. 7, pp. 229–254, 1991.

[94] J. Pfeuffer, P. van de Mortele, K. Ugurbil, X. Hu, and G. Glover, "Correction of physiologically induced global of-resonance effects in dynamic echo-planar and spiral functional imaging," *MRM*, vol. 47, pp. 344–353, 2002.

[95] C. Pierpaoli and P. Basser, "Toward a quantitative assesment of diffusion anisotropy," *Mag. Res. Med.*, vol. 36, pp. 893–906, 1996.

[96] B. Poser, M. Barth, P. Goa, W. Deng, and V. Stenger, "Single-shot echo planar imaging with nyquist ghost compensation: Interleaved dual echo with acceleration (idea) echo-planar imaging (epi)," *MRM*, vol. 69, pp. 37–47, 2013.

[97] S. Posse, C. DeCarli, and D. Le-Bihan, "3d echo planar spectroscopic imaging at short echo times in human brain," *Radiology*, vol. 192, pp. 733–738, 1994.

[98] S. Posse, G. Tedeschi, R. Risinger, R. Ogg, and D. Le-Bihan, "High speed 1h spectroscopic imaging in human brain by echo planar spatial-spectral encoding," *Magn. Reson. Med.*, vol. 33, pp. 34–40, 1995.

[99] C. Prieto, M. Usman, J. Wild, S. Kozerke, and P. Batchelor, "Group sparse reconstruction using intensity-based clustering," *Mag. Res. Med.*, vol. in press, 2012.

[100] T. Reese, O. Heid, R. Weisskoff, and V. Wedeen, "Reduction of eddy-current-induced distortion in diffusion mri using a twice-refocused spin echo," *MRM*, vol. 49, pp. 177–182, 2003.

[101] P. Roemer, W. Edelstein, C. Hayes, and S. Souza, "The nmr phased array," *MRM*, vol. 16, pp. 192–225, 1990.

[102] D. Rovnyak, D. Frueh, M. Sastry, Z. Sun, A. Stern, J. Hoch, and G. Wagner, "Accelerated acquisition of high resolution triple-resonance spectra using non-uniform sampling and maximum entropy reconstruction," *J Magn. Reson*, vol. 170, pp. 15–21, 2004.

[103] L. Rudin, S. Osher, and E. Fatemi, "Nonlienar total variation based noise removal algorithms," *Physica D*, vol. 60, pp. 259–268, 1992.

[104] L. Ryner, J. Sorenson, and M. Thomas, "Localized 2d j-resolved 1h mr spectroscopy: strong coupling effects in vitro and in vivo," *Magn. Reson. Imag.*, vol. 13, pp. 853–869, 1995.

[105] M. Saunders. (2013) Pdco: Primal-dual interior method for convex objectives. [Online]. Available: http://www.stanford.edu/group/SOL/software/pdco.html

[106] P. Schmieder, A. Stern, G. Wagner, and J. Hoch, "Application of nonlinear sampling schemes to cosy-type spectra," *J. Biomolecular. NMR*, vol. 3, pp. 569–576, 1993.

[107] ——, "Quantification of maximum-entropy spectrum reconstructions," *J Magn. Reson.*, vol. 125, pp. 332–339, 1997.

[108] R. Schulte, T. Lange, J. Beck, D. Meier, and P. Boesiger, "Improved two-dimensional j-resolved spectroscopy," *NMR Biomed.*, vol. 19, pp. 264–270, 2006.

[109] C. Shannon, "A mathematical theory of communication," *Bell Sys. Tech. J.*, vol. 27, pp. 379–423,623–656, 1948.

[110] H. Shapiro and R. Silverman, "Alias-free sampling of random noise," *SIAM*, vol. 8, pp. 225–248, 1960.

[111] S. Sibisi, J. Skilling, R. Brereton, E. Laue, and J. Staunton, "Maximum entropy signal processing in practical nmr spectroscopy," *Nature*, vol. 311, pp. 446–447, 1984.

[112] A. Simoneti, W. Melssen, M. van der Graaf, A. Heerschap, and L. Buydens, "Automated correction of unwanted phase jumps in reference signals which corrupt mrsi spectra after eddy current correction," *JMR*, vol. 159, pp. 151–157, 2002.

[113] J. Skilling, *Maximum-Entropy and Bayesian Methods in Science and Engineering.* Kluwer, 1988.

[114] J. Skilling and R. Bryan, "Maximum entropy image reconstruction: General algorithm," *Mon. Not. R. Astr. Soc.*, vol. 211, pp. 111–124, 1984.

[115] S. Smith, T. Levante, B. Meier, and R. Ernst, "Computer simulations in magnetic resonance. an object-oriented programming approach," *J. Magn. Reson.*, vol. 106a, pp. 75–105, 1994.

[116] A. Stern, D. Donoho, and J. Hoch, "Nmr data processing using iterative thresholding and minimum l_1-*norm* reconstruction," *J. Magn. Reson.*, vol. 188, pp. 295–300, 2007.

[117] T. Sugahara, Y. Korogi, M. Kochi, I. Ikushima, Y. Shigematu, T. Hirai, T. Okuda, L. Liang, Y. Ge, Y. Komohara, Y. Ushio, and M. Takahashi, "Usefulness of diffusion-weighted mri with echo-planar technique in the evaluation of cellularity in gliomas," *J. Magn. Reson. Imag.*, vol. 9, pp. 53–60, 1999.

[118] T. Thiel, M. Czisch, G. Elbel, and J. Hennig, "Phase coherent averaging in magnetic resonance spectroscopy using interleaved navigator scans: Compensation of motion artifacts and magnetic field instabilities," *MRM*, vol. 47, pp. 1077–1082, 2002.

[119] M. Thomas, S. Lipnick, S. Velan, X. Liu, S. Banakar, N. Binesh, S. Ramadan, A. Ambrosio, R. Raylman, J. Sayre, N. DeBruhl, and L. Bassett, "Investigation of breast cancer using two-dimensional mrs," *NMR in BioMed*, vol. 22, pp. 77–91, 2008.

[120] M. Thomas, K. Yue, N. Binesh, P. Davanzo, A. Kumar, B. Siegel, M. Frye, J. Curran, R. Lufkin, P. Martin, and B. Guze, "Localized two-dimensional shift correlated mr spectroscopy of human brain," *Magn. Reson. Med.*, vol. 46, pp. 58–67, 2001.

[121] R. Tibshirani, "Regression shrinkage and selection via the lasso," *J Roy. Stat. Soc. Series B*, vol. 58, pp. 267–188, 1996.

[122] J. Tropp and A. Gilbert, "Signal recovery from partial information via orthogonal matching pursuit," *IEEE Trans. Info. Theory*, vol. 53, pp. 4655–4666, 2007.

[123] M. Usman, C. Prieto, T. Schaeffter, and P. Batchelor, "k-t group sparse: A method for accelerating dynamic mri," *Mag. Res. Med.*, vol. 66, pp. 1163–1176, 2011.

[124] W. van der Zwaag, J. Marques, H. Lei, N. Just, T. Kober, and R. Gruetter, "Minimization of nyquist ghosting for echo-planar imaging at ultra-high fields based on a negative readout gradient strategy," *JMRI*, vol. 30, pp. 1171–1178, 2009.

[125] D. Wei, W. O. T. A. O. Yin, and Y. Zhang, "Group sparse optimization by alternating direction method," Dept. Comp. and App. Math., Rice U., Tech. Rep., 2011.

[126] J. Wild, "Artifacts introduced by zero order phase correction in proton nmr spectroscopy and a method of elimination by phase filtering," *JMR*, vol. 137, pp. 430–436, 1999.

[127] D. Williams, J. Detre, J. Leigh, and A. Korestsky, "Magnetic resonance imaging of perfusion using spin inversion of arterial water," *PNAS*, vol. 89, pp. 212–216, 1992.

[128] S. Wright and L. Wald, "Theory and application of array coils in mr spectroscopy," *NMR in Biomed*, vol. 10, pp. 394–410, 1997.

[129] M. Yuan and Y. Lin, "Model selection and estimation in regression with grouped variables," *Statist. Soc. B.*, vol. 68, pp. 49–67, 2006.

[130] A. Ziegler, M. Izquierdo, and M. Decorps, "Optimization of homonuclear two-dimensional correlation methods for in vivo and ex vivo nmr," *J. Magn. Reson. Series B*, vol. 107, pp. 10–18, 1995.

[131] J. Zou, Y. Fu, Q. Zhang, and H. Li, "Split bregman algorithm for multiple measurement vector problem," *Multidim Syst Sign Process*, pp. 1–18, 2013.